공학박사 학위논문

Study on Hierarchically Porous Carbon/Polymer Composites for High-performance Flexible Supercapacitors

고성능 유연성 슈퍼커패시터를 위한 계층적 다공성 탄소/고분자 복합체 연구

2023 년 2 월

서울대학교 융합과학기술대학원

융합과학부 나노융합전공

장명석

Study on Hierarchically Porous Carbon/Polymer Composites for High-performance Flexible Supercapacitors

지도 교수 박 원 철

이 논문을 공학박사 학위논문으로 제출함
2022 년 11 월

서울대학교 융합과학기술대학원
융합과학부 나노융합전공
장 명 석

장명석의 공학박사 학위논문을 인준함
2023 년 1 월

위 원 장	김 연 상	(인)
부위원장	박 원 철	(인)
위 원	임 형 준	(인)
위 원	김 정 민	(인)
위 원	유 태 경	(인)

Abstract

Study on Hierarchically Porous Carbon/Polymer Composites for High-performance Flexible Supercapacitors

Myeongseok Jang
Program in Nano Science and Technology
Graduate School of Convergence Science and Technology
Seoul National University

A supercapacitor, which is a type of electrochemical energy storage device, refers to a capacitor having a very large storage capacity. Supercapacitors, which have been commercialized since the 1980s and have a relatively short history, have continuously improved their performance due to the advent of new electrode materials such as metal oxides and conductive polymers as well as activated carbon and the development of hybrid material technology. Supercapacitors are becoming more important as they provide stable and high-quality electrical energy with fast charge/discharge rate, high power density, and cycle stability. However, to meet the continuously increasing market demand, lots of researchers are struggling to develop high-performance flexible supercapacitors with the improved energy density. The energy density of a supercapacitor is determined by the capacitance (C) and operating voltage range (V). Therefore, in this thesis, we discussed a method for improving the capacitance and voltage range by using carbon/polymer hybrid materials exhibiting a hierarchically porous structure to fabricate a high-performance flexible supercapacitor.

First, a textile-type free-standing electrode made of carbon fiber coated with a hierarchically porous carbon was prepared and used as an electrode for supercapacitor application. The activated carbon electrode, highly interconnected in a three-dimensional porous structure, showed stable macro- (>50 nm), meso- (2~50 nm), and micro- (<2 nm) sized pores, resulting in excellent charge conductivity and a large surface area with stable ion diffusion path. As a result, when it was used as an electrode, superior capacitance value was achieved. In addition, since the free-standing binder-free electrode can be directly used in supercapacitor device, effective large-area and mass production of electrode is possible. The hierarchically porous carbon structure of the carbon fibers can be accomplished by increasing the carbonization yield after heat treatment through controlling the mixing ratio of an organic-inorganic mixture composed of citric acid as a carbon source and potassium ion as an activating agent. Also, the potassium ions undergo self-templating and catalytic reactions during heat treatment, the stable porous carbon structure could be obtained even at relatively low temperature of 700 ℃. Furthermore, in the porous carbon electrode formed by pyrolysis and salt template removal process, oxygen-related functional groups remaining on the surface increased electrolyte affinity and exhibited a doping effect. As a result, the self-organized hierarchically porous carbon electrode represented excellent charge storage capacity through the synergistic effect of high conductivity, porosity, and oxygen-related functional groups. To confirm the feasibility, an all-solid-state symmetric supercapacitor was fabricated using the prepared carbon electrode, and excellent performance with an energy density of 0.69 mWh cm^{-3} and a power density of 4.91 mW cm^{-3} was obtained through electrochemical evaluation. In addition, this device exhibited excellent cycle stability enough to maintain about 88% of its initial capacity even after 10,000 charge/discharge cycles and was also confirmed as a flexible energy storage device.

In the second part, a supercapacitor with excellent energy storage performance was prepared by grafting a redox-active conductive polymer to activated graphene to further enhance the pseudocapacitive reaction. First, the formation of defects such as voids and tears on the graphene oxide sheet plane was induced through chemical etching, and the Buchwald-Hartwig coupling reaction between the as-prepared activated graphene oxide and precursors for hybrid polymer was conducted. Through this, an anthraquinonylamine-based conjugated microporous polymer (CMP) network incorporating activated graphene was synthesized. The activated graphene provides a very rigid

conductive matrix to prevent re-agglomeration of the polymer and facilitates the ion diffusion into the active materials. In addition, the CMP network, in which anthraquinonylamine and triphenylamine are cross liked to each other, exhibiting good conductivity and mechanical/chemical/thermal stability, prevents graphene re-stacking and maintains the hierarchical porosity of the composite. This further enhances the electrochemical charge storage capacity by providing abundant redox reaction sites with excellent ion transport. The properties of the polymer/activated graphene hybrid were optimized by controlling the amount of graphene added and the degree of activation, and as a result, an electrode with high capacity, fast charge/discharge rate, cycle stability, and flexibility could be prepared. Furthermore, using the synthesized polymer/activated graphene composite as a positive electrode and activated graphene as a negative electrode, a quasi-solid-state asymmetric supercapacitor could be fabricated, which represented a superior volumetric energy density of 76.6 Wh kg^{-1} and a power density of 27,634 W kg^{-1}. Also, the manufactured device exhibited excellent cycle stability, maintaining an initial capacity of 88% even after 20,000 charge/discharge cycles along with flexibility.

In this thesis, three-dimensional hierarchically porous electrode materials exhibiting a high capacitance value were synthesized, and flexible supercapacitors representing excellent performance were developed. In the first study, the energy storage capacity was improved by fabricating a textile-type free-standing activated carbon electrode with stable porosity through the

optimization of the internal structure and surface affinity of the electrode material. In the second study, the energy storage capacity was maximized by synthesizing a redox-active polymer/activated graphene composite, and the flexible energy storage device showing further improved performance was developed by fabricating an asymmetric supercapacitor with a wide operating voltage range. Therefore, this study is expected to be applied to the development field of flexible energy storage device with environmentally friendly materials and a cost-competitive manufacturing method.

Keywords : Supercapacitors, Hierarchically porous carbon, Activated graphene, Conjugated microporous polymer network, Carbon/polymer hybrid

Student Number : 2018-36419

Contents

Chapter 1. Introduction ······································ 1

List of Figures

List of Tables

Chapter 1. Introduction

1.1 Supercapacitors

In a situation where global energy consumption is steadily increasing, power generation using sustainable renewable energy has been steadily expanding globally due to climate change and depletion of fossil fuel resources. To realize carbon neutrality, the proportion of end-use electric energy must be increased, and the most electricity must be produced cleanly from renewable energy sources such as solar and wind power (Figure 1.1). However, the solar and wind power have a disadvantage in that the output fluctuates rapidly depending on the weather conditions, and thus the range of power generation fluctuation is significant. Therefore, an energy storage system (ESS) is necessary to utilize a renewable energy source with a large variation in load response characteristics as described above [1-3].

A supercapacitor, also called an ultracapacitor or an electrochemical capacitor, stores electrochemical energy by the adsorption/desorption of electrolytic ions or a fast and reversible redox reaction at the electrode surface, which is distinct from the chemical reaction of a battery [4]. A supercapacitor features high specific power, high capacitance, almost infinite cyclability, short charging time, good stability, low maintenance cost, and fast frequency response. Supercapacitors have been used in electronic devices to meet the requirements of rapid charging/discharging, such as for memory back-up and uninterruptible power supply (UPS). Also, their use is being extended to transportation and large industry applications that require high power/energy density, such as for electric vehicles and power quality systems of smart grids. In power generation using intermittent power sources such as solar and wind, a supercapacitor is configured in the ESS together with a battery to compensate for the relatively slow charging/discharging time of the battery, to contribute to extending the lifespan of the battery, and to improve the system power quality.

Through the Ragone plot of Figure 1.2 and Table 1.1, the relative energy density and power density of supercapacitors can be compared with other energy storage devices. Supercapacitors exhibit relatively lower power densities than conventional capacitors. The biggest difference between a supercapacitor and a conventional capacitor is that there is no dielectric material. Conventional capacitors consist of a dielectric plate for storing static charges, whereas supercapacitors consist of two electrodes separated by a separator in an electrolyte. Batteries are operated mainly by intercalation and de-intercalation of positive ions controlled by diffusion, and this diffusion limits the charge/discharge rate and power density. Supercapacitors tend to have lower energy densities and provide much greater power densities compared to batteries because the charge storage reaction takes place in the outer layer of the electrode [5,6].

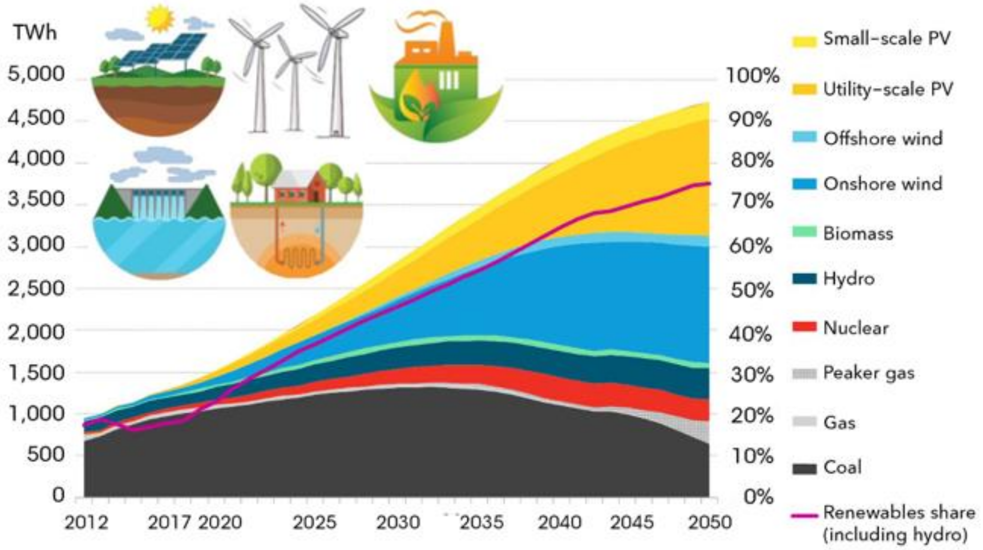

Figure 1.1. Global generation capacity of sustainable energy (source from Bloomberg new energy finance 2020).

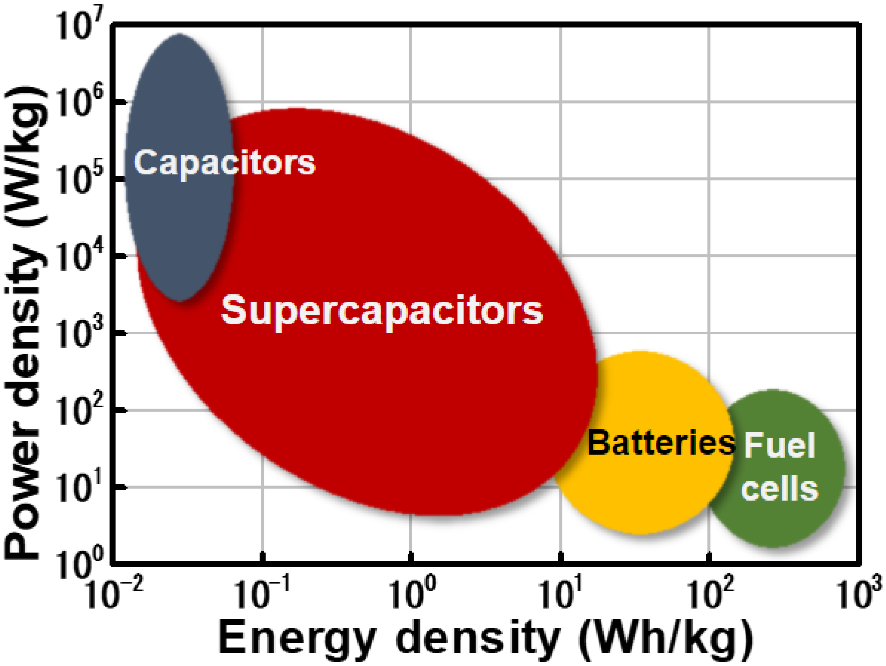

Figure 1.2. Ragone plot for different energy storage devices.

Table 1.1. Comparison of the performance for different electrochemical energy storage system.

Parameter	Capacitor	Supercapacitor	Battery
Energy density / Wh kg^{-1}	< 0.1	1 ~ 10	70 ~ 100
Power density / W kg^{-1}	> 10,000	> 1,000 ~ 2,000	50 ~ 200
Charge/discharge time	10^{-6}~10^{-3} s	s to min	1 ~ 5 h
Coulombic efficiency	~ 100	85 ~ 95	70 ~ 85
Cycle life	> 500k	> 100k	0.5 ~ 2k
Determinants	area,dielectric	porosity	thermodynamics

1.2 Energy storage mechanisms of supercapacitors

A supercapacitor, which is composed of two electrodes, electrolyte, and separator, operates through an electrochemical mechanism generated by applying voltage to both ends of a unit cell electrode, moving ions in the electrolyte along an electric field and adsorbing them to the electrode surface, and for this reason, they are also called electrochemical capacitors (Figure 1.3). Since the energy storage of supercapacitors is based on charge accumulation or reversible redox reaction, it is largely divided into electric double layer capacitors (EDLCs) and pseudocapacitors according to electrodes and mechanisms (Figure 1.4) [5]. EDLCs use carbon-based materials as an electrode and follows an electric double-layer (EDL) charge adsorption mechanism that electrostatically stores charge at the interface between the electrolyte and the electrode (a non-Faraday process without charge transfer between the electrode and the electrolyte). Pseudocapacitors use metal oxides and conductive polymers as electrode materials and stores electric charges through electric deposition, fast and reversible redox reaction (a Faradaic process in which electric charges move between an electrolyte and an electrode). The pseudocapacitance depends on the structure of the electrode, the size of the electrode pores, and the chemical affinity of the material for the ions adsorbed on the electrode surface.

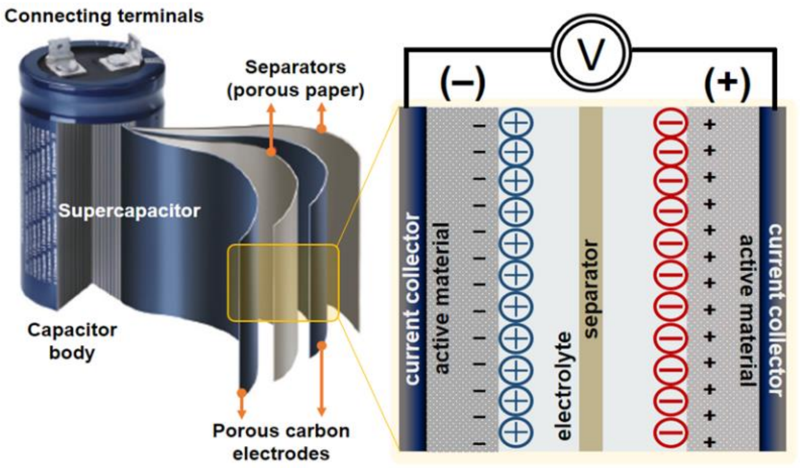

Figure 1.3. Schematic illustration of conventional supercapacitors.

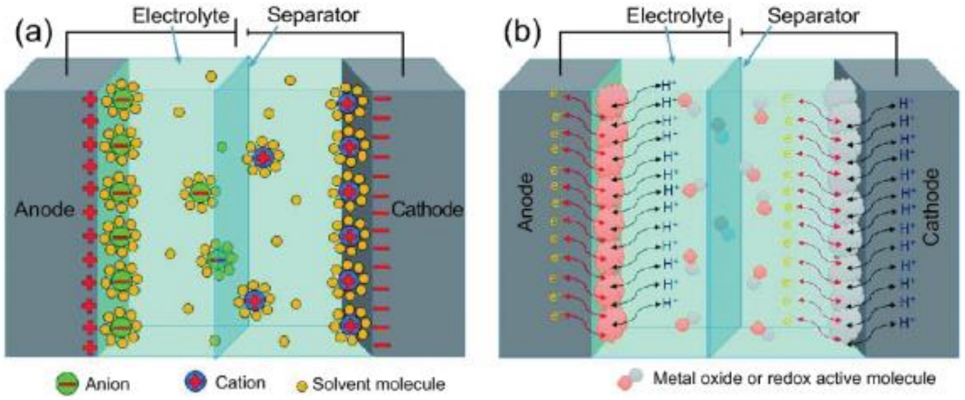

Figure 1.4. Schematic representation of (a) electrical double-layer capacitors (EDLCs) and (b) pseudocapacitors (PCs) [5].

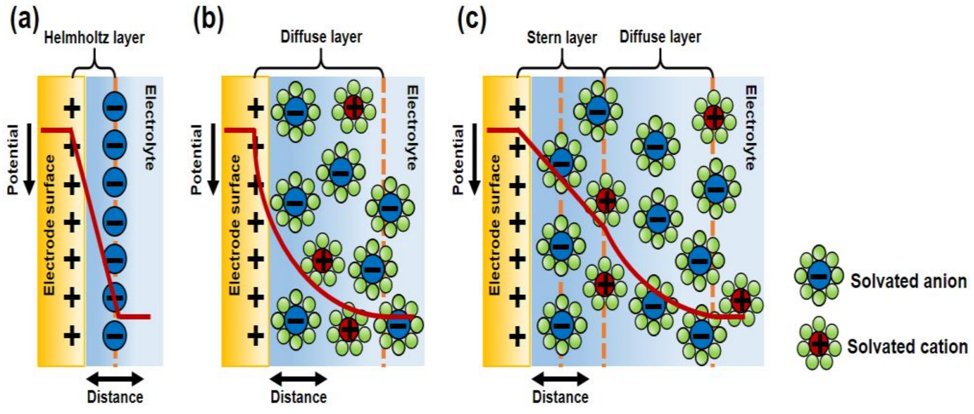

Figure 1.5. Schematic illustration of (a) Helmholtz, (b) Gouy-Chapman, and (c) Stern model of the electrical double-layer at a positively charged surface in an electrolyte [7-10].

Conventional capacitors store very little energy because of the limited charge storage areas and geometric constraints of the separation distance between the two charged plates. Charge separation occurs on polarization at the electrode-electrolyte interface. As illustrated in Figure 1.5, in the 19th century, the concept of the EDL was first explained and modeled by von Helmholtz when he investigated the distribution of the opposite charges at the interface of colloidal particles. The Helmholtz double-layer model states that two layers of opposite charge form at the electrode/electrolyte interface and are separated by an atomic distance [7]. The model is similar to that of two-plate conventional capacitors.

The capacitance (C) can be evaluated according to the following equation:

$$\mathrm{C} = \frac{\varepsilon_r \varepsilon_0 A}{d}$$

where C (F), ε_r, ε_0, A, and d represent the capacitance, electrolyte dielectric constant, dielectric constant of the vacuum, surface area of electrode, and double layer thickness, respectively. But Gouy and Chapman suggested a diffusion-model of the electrical double-layers in which the potential decreases exponentially from the electrode surface to the fluid bulk. This is because of the Helmholtz model does not regard several factors such as the interaction between the dipole moment of the solvent and the electrode, and the diffusion of ions in the solution [8,9]. However, the Gouy-Chapman model is also not enough for highly charged double-layers, and later, Stern combined the Helmholtz model with the Gouy-Chapman model, dividing the ion distribution into two regions: an inner region and a diffusion layer [10].

In conclusion, EDLCs store static electricity through a non-faradaic reaction, and a difference from batteries is that there is no limit to the electrochemical dynamics through polarization resistance. These surface storage mechanisms provide fast energy adsorption and transfer and good power performance. Also, because there is no faradaic reaction, the expansion of the active materials during charge/discharge cycles seen in the batteries is also not exhibited. Thus, EDLCs features very stable cycling ability, high charge and discharge rate, and excellent cycling stability [11-13]. In general, carbon-based materials are electrode materials that have the EDL mechanism. Carbon-based materials are the most promising candidates for electrode materials due to their abundance, low cost, and eco-friendly properties, as well as their high specific surface area, good mechanical stability, and good electrical conductivity [11].

1.3 Materials for supercapacitor devices

1.3.1 Carbon materials

In general, carbon materials, i.e., activated carbon [14-17], carbon nanotube (CNT) [18-20], graphene [21-23], and carbon aerogel (frozen smoke) [24-26] are used as electrode materials for EDLCs owing to their significant advantages, i.e., good electronic conductivity, high durability, low cost, and benign environmental availability. Activated carbons, which are conventionally used in most supercapacitors due to its abundance and a relatively low cost, have a large effective surface area and very large capacitance, but shows a very weakly graphitized framework of irregular shapes and wide pores. On the other hand, CNTs can form relatively uniform surface pores, and have excellent stability (mechanical and thermal) and electrical properties. Graphene has emerged as a high-capacitive EDLC electrode materials in recent decades and has a unique hierarchical structure with a wide effective surface area and superior electrochemical and mechanical properties.

1.3.2 Redox active materials

Electrode materials for pseudocapacitors include transition metal oxides (MO_x) [27-31], i.e., IrO_2, RuO_2, MnO_2, Fe_3O_4, Co_3O_4, NiO, and V_2O_5, and conductive polymers [32-36], i.e., polyaniline (PANI), polythiophene (PT), polypyrrole (PPy), polyvinyl alcohol, poly (3,4-ethylene dioxythiophene (PEDOT), polyacetylene, poly (4-styrene sulfonate) (PSS), and polyphenylene-vinylene

(PPV). Although these redox-active materials, which are storing energy through surface oxidation/reduction reactions, can be expected to improve energy density with a relatively high theoretical capacity value compared to carbon, they are not suitable for high-speed energy storage environments due to its relatively low conductivity, and have disadvantages in that they have an unstable structure during charging/discharging cycles. Therefore, recently, new electrode materials, such as a composite with graphene, CNT, and structured carbon materials, or a structure doped with heteroatoms through cation substitution, are being actively studied such as covalent-organic frameworks (COFs), metal-organic frameworks (MOFs), MXenes, and metal sulfides (or nitrides) [37-42]. Figure 1.6 compares the energy storage performance of electrode materials corresponding to carbons, polymers, and metal oxides [43].

1.3.3 Electrolyte and separator

In addition, electrolyte plays an essential role in setting important properties such as power density, operation temperature, and conductivity, and is divided into water-soluble, organic, ionic liquid, etc., and improves electrochemical performance (ion concentration, voltage range, resistance, volatility), and it has been widely adopted with a focus on safety (toxicity) and compatibility (cost). So far, in supercapacitors, separators are generally used in the form of electrically insulating and ion-permeable paper, polymer and ceramic materials wetted with electrolyte to allow the transfer of charged ions between electrodes [44].

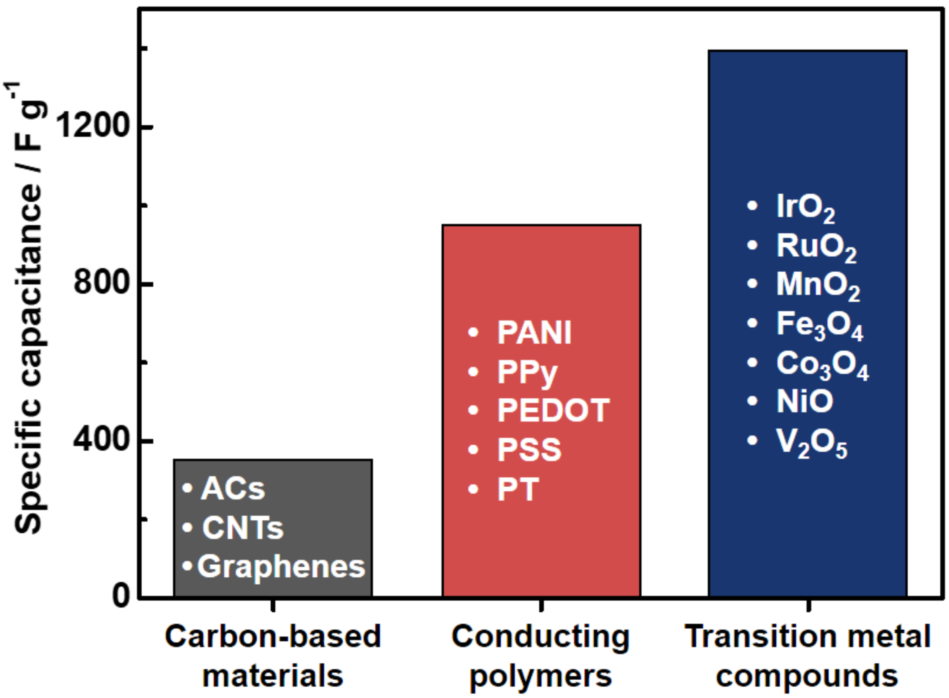

Figure 1.6. Various types of electrode materials for supercapacitors and its specific capacitances.

1.4 Challenges and strategies

Electrode materials play an essential role in supercapacitor applications. The electrode of the supercapacitor is required to have high conductivity, temperature stability, good chemical stability, high specific surface area, corrosion resistance, environmental friendliness, and low cost for fabrication. Also, the material properties that undergo Faradaic reactions further increase the total capacitance [10]. Based on an in-depth understanding of the energy storage mechanism of the interfacial reaction between electrode materials and electrolytes, many researchers have designed hierarchically interconnected porous electrodes to avoid dead volume and obtain efficient reactive surface, which improves the electrochemical performance by controlling the interactions within the cell.

There are two parameters for evaluating the electrochemical performance of supercapacitors. The maximum energy density (E) and power density (P) can be obtained by following equations:

$$\mathrm{E\ (Wh\ kg^{-1})} = \frac{CV^2}{2}$$

$$\mathrm{P\ (W\ kg^{-1})} = \frac{V^2}{4R}$$

where C, V, and R represent capacitance, operating voltage, and equivalent series resistance. However, EDLCs suffer from a limited energy density due to a consequence of electrostatic surface charging mechanism [10]. Therefore, EDLC research are currently focused on improving the energy density by increasing specific capacitance of electrodes and the operating voltage of cells.

To improve specific capacitance, the strategies are focused on increasing the specific surface area, optimizing the pore size, and pore size distribution by developing hierarchically porous structure without sacrificing the good electrical conductivity. Moreover, the high specific capacitance can be achieved by introducing redox species, i.e., conductive polymers and transition metals to contribute additional Faradaic pseudocapacitance.

1.4.1 Hierarchically porous carbon

One of the strategies to improve the energy density and cycle life of EDLCs is the structural modification of the carbon materials. Recent research has shown that hierarchically porous carbon combining micropores with meso- and macropores is promising electrode material for supercapacitor applications [17, 45-47]. The hierarchical porous structure can provide high accessible surface area and consequently large exposed active sites and facilitate ion transport for high-rate capability. As the name suggests, the basic requirement for the hierarchical porous structure is that a porous system should contain multi-scale pores. According to the International Union of Pre and Applied Chemistry (IUPAC) definition, porous materials are classified into three categories according to their pore size: micro pores (< 2 nm), mesopores (2-50 nm), or macroporous (>50 nm) (Figure 1.7). Porous systems that solely contain different sizes of pores is not necessarily qualified as hierarchical porous structure. The notion of 'hierarchy' in a material requires a clear presentation of the interplay between all different pores and formation of a hierarchical network. To be qualified as the hierarchically porous structure, different types of pores should be at least interconnected with each other. As a result, ions enter first into largest pores and then flow into smaller ones that are subdivided from the larger pores. This pattern continues until ions reach the smallest pores. In this manner, hierarchically porous structured carbon materials can accomplish a large surface area with pore volumes, good ion accessibility, mass transport property, and superior energy storage capacity, which can be utilized in various applications where it shows its advantages compared to conventional porous carbon materials. In terms of energy storage system, i.e., active materials surface vs. electrolyte, micropores in 0.7–1 nm range provide a large specific surface area for charge storage, while meso- and macropores act as ion diffusion pathways and ion-buffering reservoirs to reduce ion diffusion range and facilitate ion transfer. Therefore, rational design of pore structure with a suitable content of micro-, meso-, and macropores can effectively increase the ion accessible surface area and thus improve the electrochemical performance [48,49].

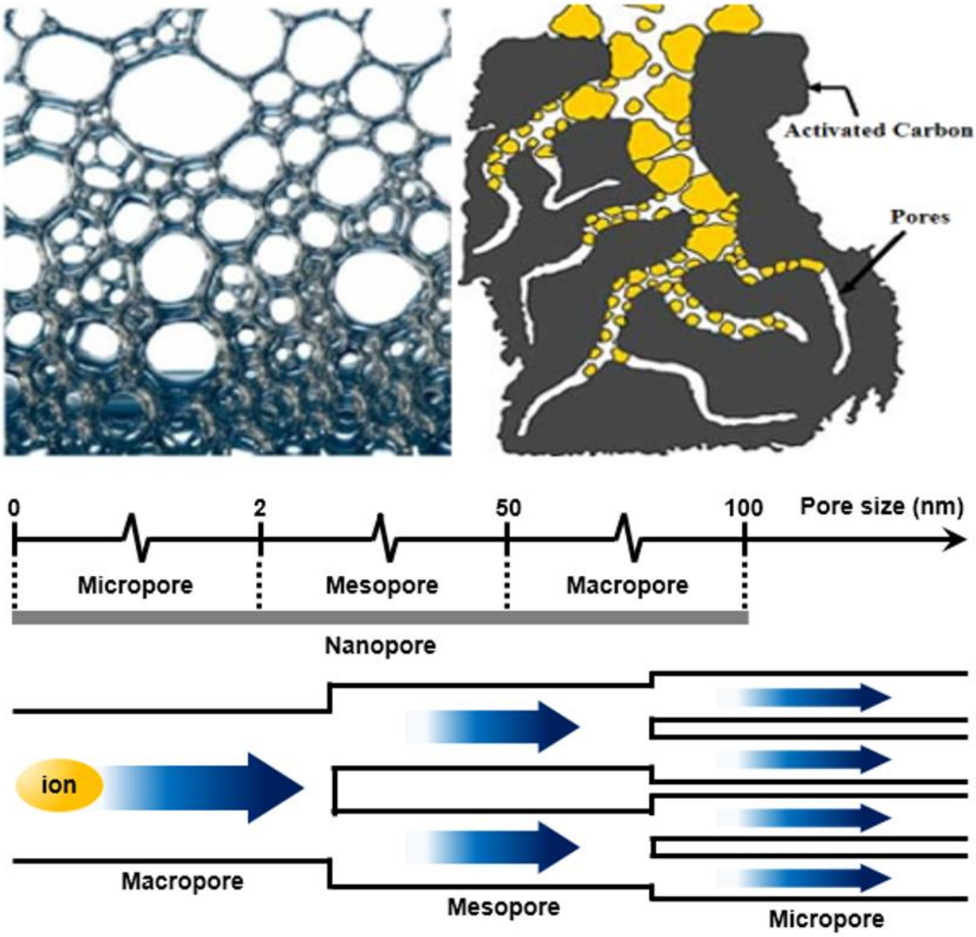

Figure 1.7. Schematic illustrations of a typical hierarchically porous structure and an ion diffusion path with IUPAC classification of pores based on the pore size [45].

1.4.2 Synthesis methods of hierarchically porous carbon

Recently, there are various methods to synthesize hierarchically porous carbon, which all have its advantages and disadvantages. Depending on the synthetic procedures, the methods can be roughly categorized into three types such as activation, template-assisting, and in-situ templating [50]. First, activation methods have been intensively utilized to generate porosity with a large surface area or introduce functional groups on the carbon surface by using various physical or chemical treatments. Physical activation can be achieved through various milling techniques using shear forces or heat treatment at 600~1200 ℃ in the presence of an activating agent such as air, oxygen, carbon dioxide, or steam. Chemical activation is a method in which an activating agent such as potassium hydroxide, sodium hydroxide, zinc chloride, iron chloride, or phosphoric acid is introduced into the precursor and thermally treated in an inert atmosphere and at a temperature of over 400 ℃ [51-55]. The obtained porous carbon, which is also called activated carbon (AC), exhibited excellent properties such as a large specific surface area and pore volume, good electrical conductivity, physicochemical durability, and relatively low costs, and thus the majority of commercial electrochemical devices utilize the AC to fabricate electrodes for supercapacitor applications [56]. The large surface area of AC provided many interaction sites for surface- or interface-related processes such as energy storage, and the large pore volume showed excellent durability during repeated electrochemical reactions (Figure 1.8). However, because AC has a broad pore distribution and contains random pore connections, these irregular pore connections with closed or narrow passageways between them limit accessibility of ions during electrochemical reactions. Therefore, controlling the porosity of AC is very important because it is directly related to the surface area and accessibility of ions and the subsequent electrochemical performance.

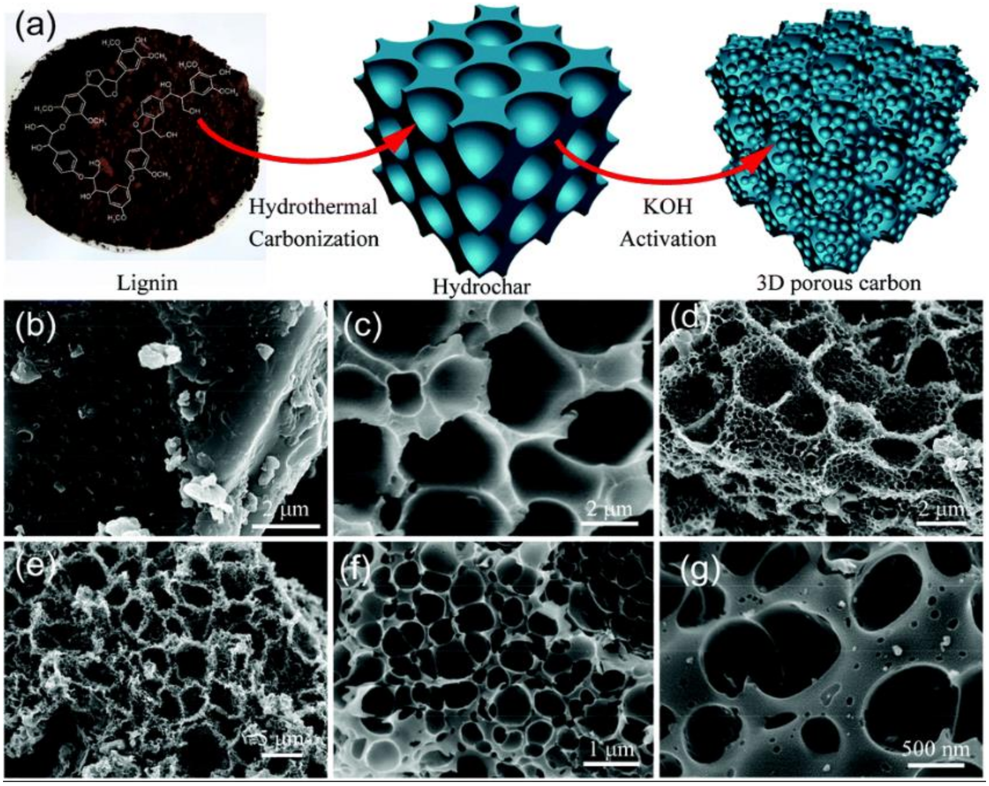

Figure 1.8. (a) Schematic illustration of the transformation of lignin into 3D hierarchically porous carbons by using activation method; (b-g) FE-SEM images with different magnifications [53].

Templating methods have been identified as useful routes to fabricate porous carbon materials with the ordered or designed structure. This method includes the soft-, hard-, and multiple-templating methods (Figure 1.9). The soft-templating route used a self-assembly of surfactant and carbon precursor, and the hard-templating is another practical approach in which porous structures are made from preformed templates, such as silica spheres or metal oxide nanoparticles. Besides, molten salts, i.e., potassium or sodium chlorides (KCl or NaCl), and sodium sulfate (Na_2SO_4) can act as the eco-friendly hard template to prepare porous structure. Porous carbon materials with diverse pore distribution and adjustable pore size have been prepared by many synthetic routes based on these templating methods mentioned above. To fabricate a hierarchically porous carbon, it is needed to use the multiple-templating methods which combine more than one different size of soft or hard template. However, there has been trouble with preparing fine templates and removing them eventually under harsh conditions leading to the complex procedures and high production costs as well. Hence, it is necessary to find a facile and cost-effective methods for preparation.

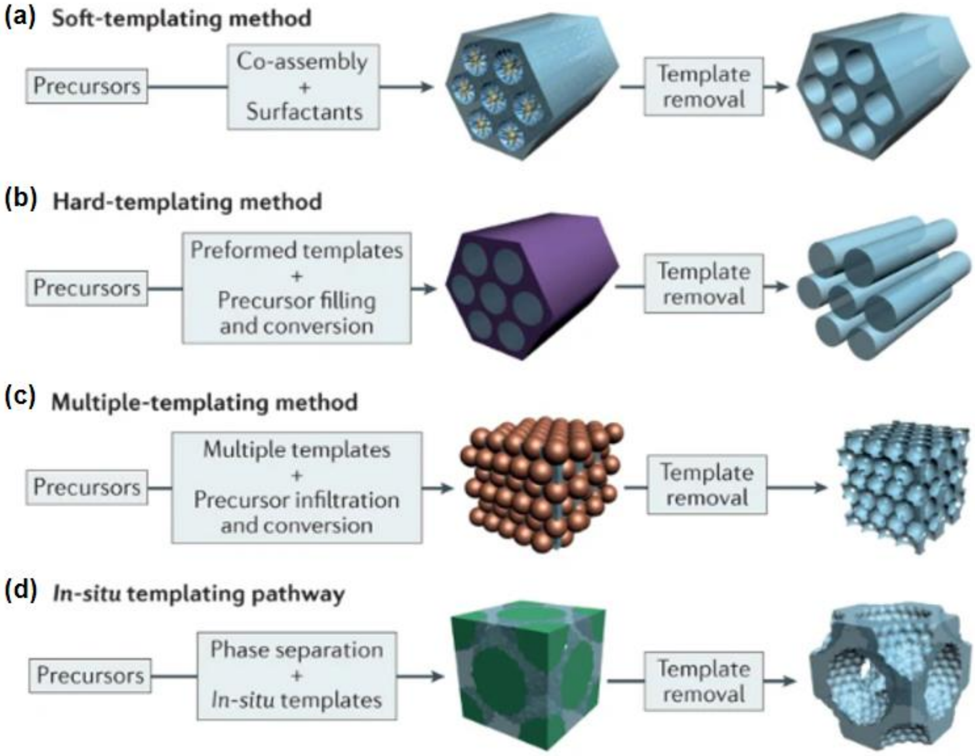

Figure 1.9. Schematic illustrations of various templating methods [50].

In-situ templating method is a possible technique that chemical species such as salts in carbon precursor itself can be directly transformed into the template by phase separation during heat treatments [50]. Alkali metal-organic salts are consisting of organic moieties and alkali metal ions. The organic parts, i.e., acetic acid, tartaric acid, gluconic acid, alginic acid, and citric acid, provide carbon sources while the inorganic species, i.e., sodium (Na), potassium (K), and calcium (Ca), transform into salts which provide template for pore generation and surface activation. Moreover, the uniform dispersion of such elements within the organic matrix at a molecular level assists the activation process effectively despite the relatively low contents of inorganic species.

Consequently, the interconnected hierarchically porous carbon can be easily prepared.

In this thesis, potassium citrate was selected from among numerous salt precursors, and the in-situ templating technique was implemented through reforming the precursor and heat treatment, and the synthesized product was named self-templated hierarchically porous carbon. During pyrolysis of potassium citrate, self-generated potassium carbonate (salt) acts as a template to form macro- and mesopores, and the potassium ion assists to form micropores at an elevated temperature [57,58]. In this precursor, the potassium moiety played an important role in the generation of hierarchically porous carbon structure because its vapor is intercalated between the bulk carbon layers causing swelling and disruption of the carbon microstructure [17]. Also, the citric acid which is known as biomolecule easily obtained from citrus fruits has been intensely studied because of its unique and intriguing molecular structure. It is well known that 3D structured porous carbon can be easily generated by a gradual thermal decomposition of citric acid [59,60]. By tuning a carbonization degree of citric acid, the molecules react each other and transform into carbon quantum dots and multi-dimensional carbon networks showing photoluminescent and electrochemical properties.

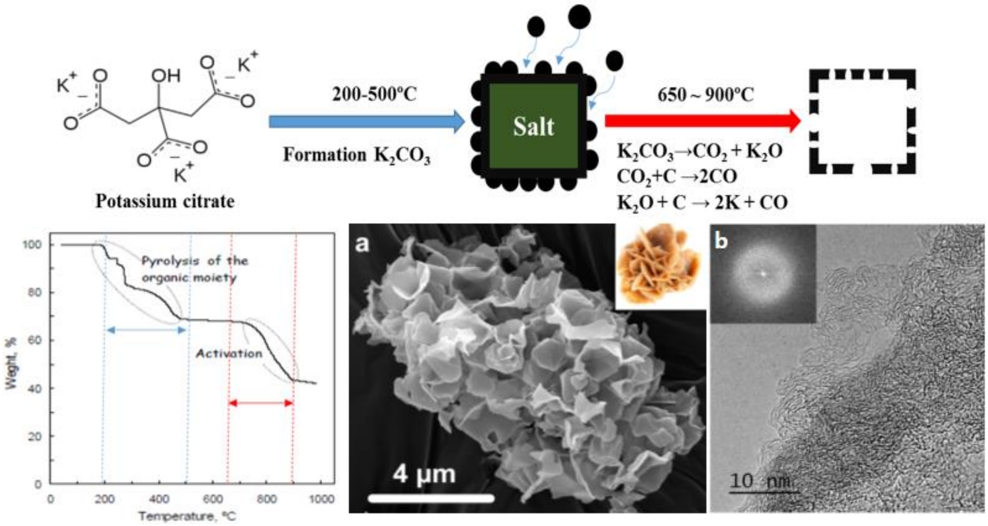

Figure 1.10. Schematic illustrations of interconnected hierarchically porous carbon nanosheets by using potassium citrate via in-situ templating method [17].

Despite these advantages of synthetic method of the self-organized hierarchically porous carbon, the end products are obtained in powder form. Accordingly, traditional slurry process is needed to prepare electrode for further electrochemical application. During the slurry process, carbon powders are often aggregated, and the interconnected macroporous structure is collapsed. Moreover, the insulating binder blocks the pores and enlarges the dead surface of the material, increasing the contact resistance and lowering the electrochemical performance. Therefore, the key challenges to date remain in the development of free-standing and binder-free hierarchically porous carbon electrode materials that are strongly interconnected to the current collector substrate.

1.4.3 Activated graphene

Among various carbon materials, graphene has been extensively studied for energy storage system due to two-dimensional flexible feature, excellent physiochemical stability, large surface area and high conductivity [21,22]. The pristine graphene nanosheets, however, cannot provide an efficient ion diffusion path due to its non-porous structure [61,62]. Ion diffusion along the plane direction is hindered by carbon atomic arrays in the graphene sheets [63]. As a result, it leads to inherent detour of ions which can trigger a slow charge/discharge process in cells. Therefore, to further improve the ion diffusivity, many researchers have attempted to introduce pores on the graphene sheets. Numerous studies have demonstrated that in-plane holey graphene structures could serve as abundant ion-penetrable channels and active surface areas for high-rate performance in energy storage devices [23,64-67]. Interestingly, it should be noted that the introduction of defects in the graphene sheet is often accompanied by the breakage of the graphene sheet due to pore growth (Figure 1.11). Therefore, controlling the activation condition of graphene can affect the structural properties of the active material used in the energy storage device as well as the improvement of the EC performance.

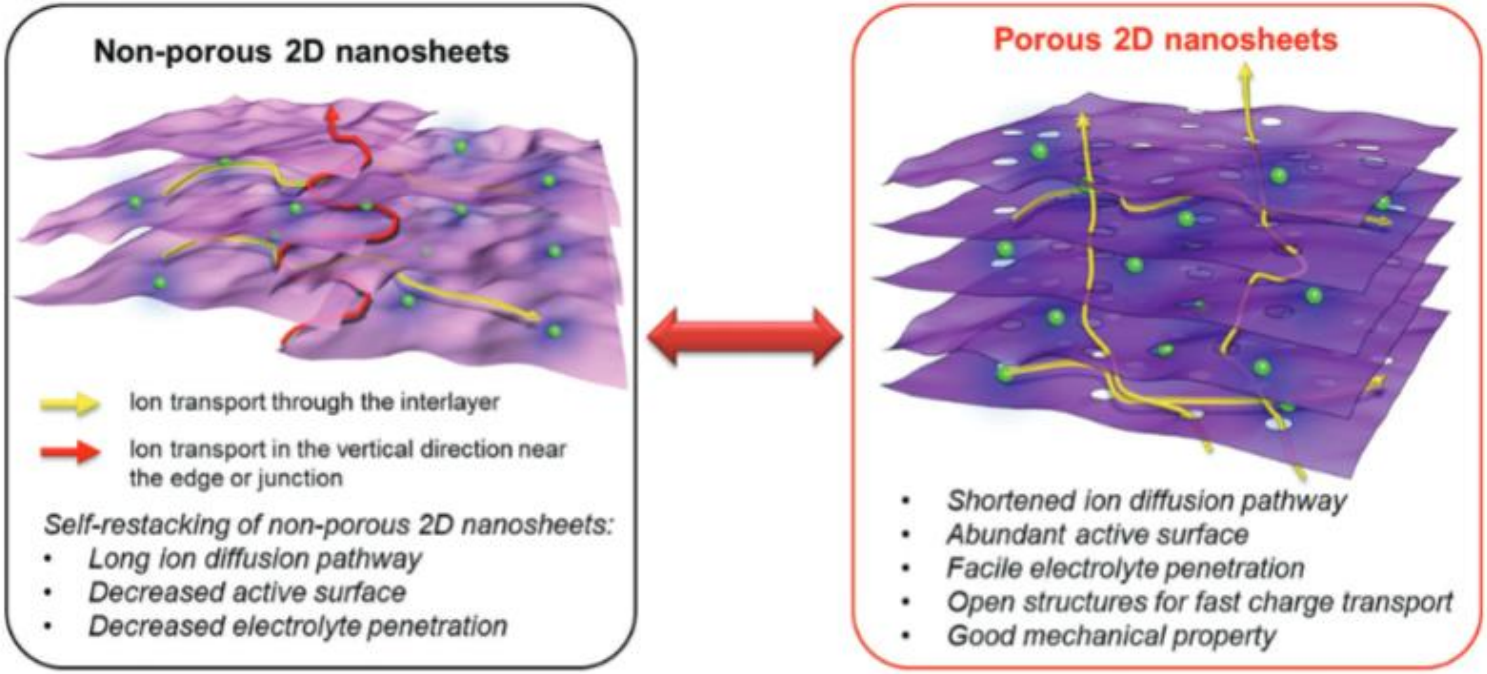

Figure 1.11. Schematic illustration of advantageous features of porous/holey 2D nanomaterials for energy storage [64].

1.4.4 Redox-active conductive polymers

Considerable efforts have been devoted in recent years to developing electrode materials with faradaic reactions. Redox supercapacitors appeared in 1940s by David C. Grahame to describe the reversible electrochemical capacity that was not related to the formation of electric double-layer. Then, in the work of Conway and Gileadi in the early 1960s, redox capacitance was used to understand the electrochemical charge transfer reactions involved in surface adsorption [68]. At first, redox capacitance was defined in terms of the fractional surface coverage of adsorbed species according to the Langmuir adsorption model. Since the capacitance arose from Faradaic reactions involving monolayers of electrochemically active species, it was distinguished from strictly electrostatic double-layer capacitance and the typical behavior of battery materials, which entailed significant phase and structural modifications of the reactants. It has been proved that these Faradaic electrochemical processes extend the working voltage as well as increase the specific capacitance of the supercapacitors [69]. As shown in the equation below, by an exchange of charge across the double layer, rather than a static separation of charge across a finite distance, resulting in oxidation-reduction reactions.

$$O_x + ne^- \leftrightarrow R_{ed}$$

The negative charge, ne^-, exchanged in this reaction, and the energy storage is indirect and analogous to that of a battery.

Redox-active conductive polymers offer a unique combination of physical charge separation across an interface and a Faradaic reaction between an electrolyte and electrode material and are possible low-cost alternatives to expensive and rare transition metals (Figure 1.12). Redox-active conductive polymers have great advantages in terms of desirable molecular structure, superior chemical and physical properties, and excellent electrochemical storage performance compared with metal-based inorganic materials [36,70,71]. Redox active small organic molecules in conductive polymers provide additional charge storage capacity. Previously, anthraquinone and its derivatives have been widely utilized for supercapacitor applications due to their low cost, high stability, and excellent redox capability [40,41]. Anthraquinone-based redox systems involve interfacial proton-coupled electron transfers, which are fast and therefore likely to facilitate greater power densities than other redox systems [72].

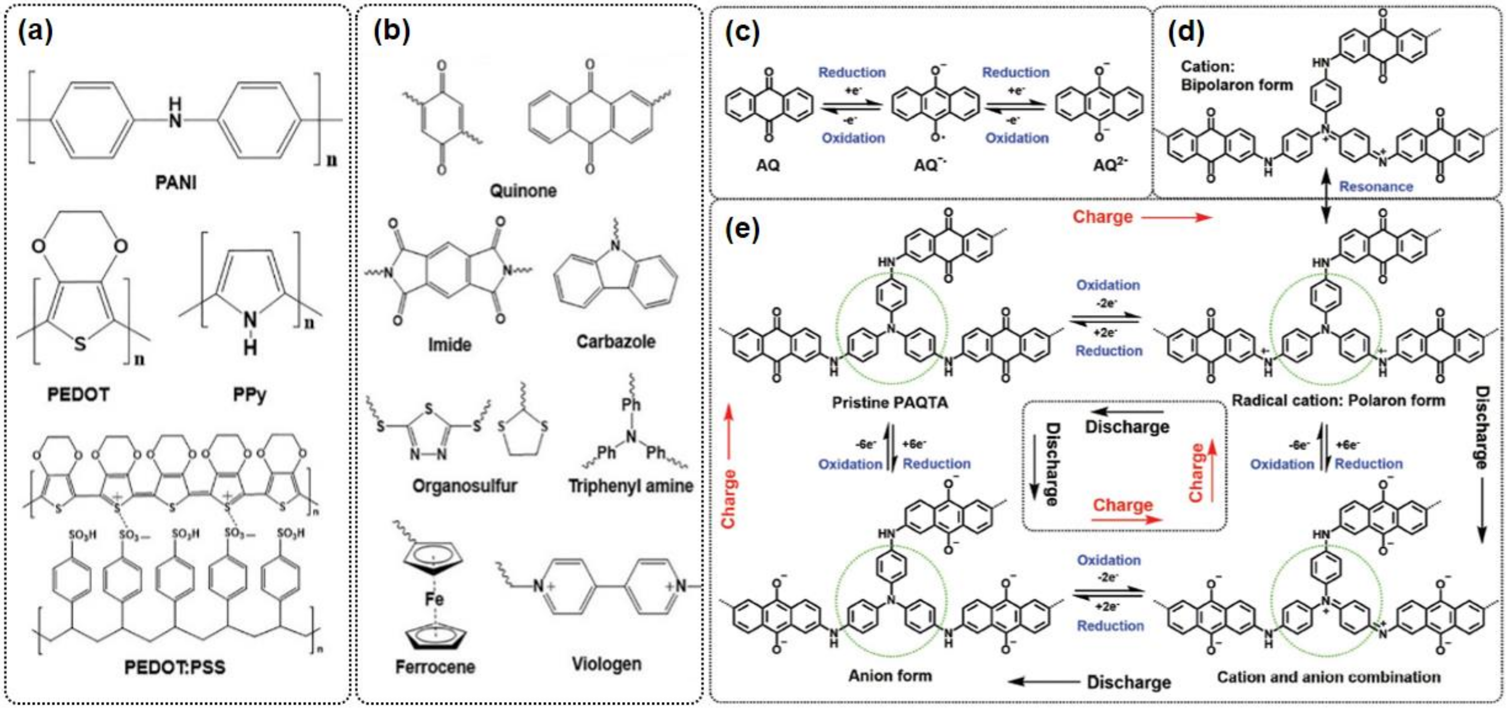

Figure 1.12. (a) Representative repeat units of conductive polymers, (b) various redox-active pendants, and (c-e) proposed redox reactions, i.e., charge/discharge mechanism for poly (anthraquinonyl triphenylamine) (PAQTA) [71].

1.4.5 Conjugated microporous polymer (CMP) hybrid networks via Buchwald-Hartwig coupling.

Traditional conductive polymers such as polyaniline, polypyrrole, and polythiophene are normally nonporous and not durable due to the decomposition after several charge/discharge cycles because of the swelling and shrinkage of linear macromolecular structures [73]. Generally, their capacitances are largely impaired after >1000 charge/discharge cycles and overall power is limited by water splitting voltage window (<1 V). As a solution to the problems mentioned above, conjugated microporous polymer (CMP) networks have attracted tremendous attention in recent years as potentially suitable candidates for energy storage application due to their good porosity with strong covalent bonding and highly unsaturated π-bond-rich nature affording high thermal and chemical stabilities and ion accessibility as well as unique electron-donating characteristics [74-76]. Furthermore, a wide range of properties including multi-scale porosity, a large surface area, and electrochemical reactivity can be fine-tuned by altering strut length, contortions, rigidity, and functional group through a variety of organic building blocks and synthetic pathways (i.e., Suzuki, Sonogashira-Hagihara and Yamamoto coupling, Schiff-base chemistry, cyclotrimerization, and oxidative polymerization reactions) [75,77]. These promising properties are expected to position CMP as an enabler for various research areas such as gas separation/storage, catalysis, and energy storage applications [78-81]. Especially, the unique porosity and microstructure with a large surface area of

CMP-based electrodes endow EDLC contribution and fast scan-rate performance, while the numerous redox-active sites of the CMP backbones, consisting of heteroatom functional groups offer outstanding pseudo energy storage performance [34,82,83]. Based on their versatile contributions, CMPs could play an important role in supercapacitive electrodes for developing efficient energy storage devices (Figure 1.13a and b).

Recently, lots of studies have recognized that CMPs synthesized via Buchwald-Hartwig (BH) coupling reaction can become one of the attractive candidates for improving the performance of supercapacitors (Figure 1.13c-g). In organic chemistry, the BH amination is a chemical reaction for the synthesis of polar C–N bonds via the palladium-catalyzed coupling reactions of amines and aryl halides [84,85]. The unique BH coupling approach allows for expansion of the repertoire of possible C–N bond formation through the facile synthesis of aromatic amines, affording a simple route to nitrogen-containing redox-active systems, which are believed to be very important for superior electrochemical energy storage [86-89]. For example, Liao et al. successfully synthesized a series of pyridine functionalized CMPs with high nitrogen contents (18 %) via BH coupling. The resulting conjugated microporous poly-triphenylamine (PTPA) networks exhibit tunable redox activity and porosity offering ideal electrode materials for supercapacitors. Combining these advantages, PTPAs delivered a high capacity of 335 F g^{-1} at 0.5 A g^{-1} with high-rate performance (achieved a capacitance of 250 F g^{-1} at 10 A g^{-1}), and high cyclability (retained 65 % of initial capacitance after 5,000 cycles at 2.0

A g^{-1}) [86]. Thomas et al. have also reported a series of poly-aminoanthraquinone (PAQ) networks synthesized by BH coupling for supercapacitive energy storage. The PAQs were found to have a combination of large surface areas (600 m^2 g^{-1}), redox activity of quinone groups, and good dispersibility in polar solvents. When applied as electrodes in a supercapacitor device, the PAQs delivered specific capacitance values of 570 F g^{-1}, retaining 80–85 % capacitance after 600 cycles with almost 100 % Coulombic efficiencies. They also investigated applications in both symmetric and asymmetric supercapacitors, demonstrating the potential of high-performance flexible energy storage devices [87,88].

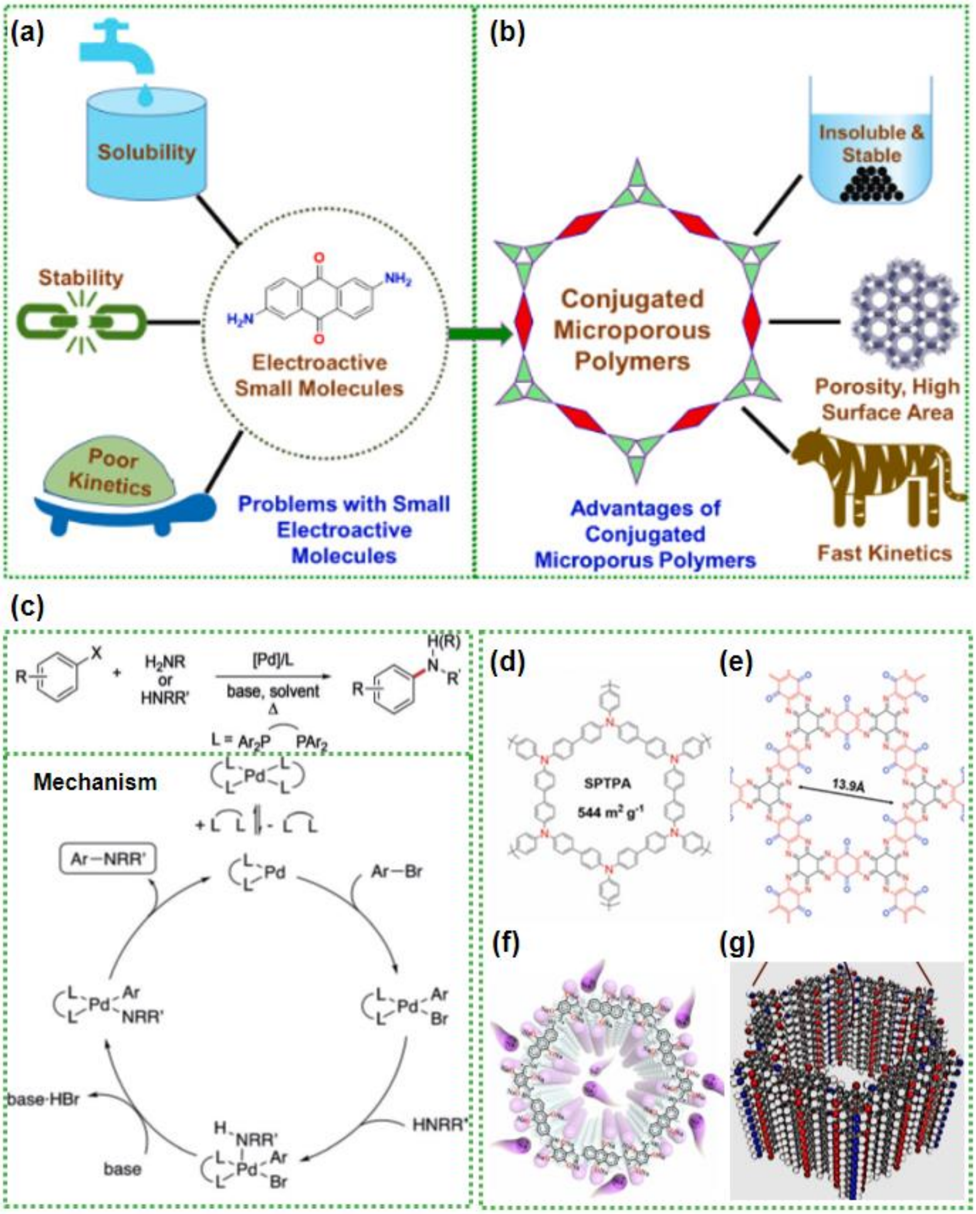

Figure 1.13. (a) Challenges associated with electroactive small organic molecules, (b) some of the advantages of conjugated microporous polymers (CMP), chemical mechanisms of the Buchwald-Hartwig coupling reaction, and (d-g) molecular images of CMP networks with good structural properties [79].

1.4.6 CMP/activated graphene nanocomposites

Despite some advances, the intrinsically low electric conductivity of conductive polymers, i.e., the quinone-based redox-active organic molecules, hamper their wide usage in energy storage because it could limit their capacitive performance, i.e., narrow voltage range, low-rate capability, and cycling stability [90-92]. Therefore, recent studies have introduced conductive support to the organic molecules to improve electrical conductivity by using carbonaceous materials such as porous carbon, carbon nanotube, and graphene, yielding a composite with performance data significantly superior to the respective data of the single components [93-100]. Among various carbon materials, graphene-based CMP composite has been found to show superior EC performance, because the graphene shows superior physicochemical properties, i.e., mechanical stability, large surface area, and high electron conductivity [21,22]. Moreover, graphene nanosheets incorporated in the CMP network offer multiple advantages, such as providing a stable framework and increasing electrical conductivity (Table 1.2). Although various anthraquinone/graphene composite designs have made remarkable progress in improving EC performance, increasing electrical conductivity has been only the focus. Importantly, it should be noted that supercapacitive reactions usually occur on the surface of the electrode [101-103]. Thus, using a high surface area material is important to ensure easy ion accessibility to the active material surface and better capacitance, yet it has been largely ignored so far.

Table 1.2. Synergistic effects of conjugated microporous polymer (CMP) grafted with activated graphene (AG) hybrids (CMP@AG) via Buchwald-Hartwig (BH) coupling.

	CMP network	**vs.**	**AG**	**→**	**Synergistic effects of CMP@AG**
Conductivity	conductivity & microporosity	<<	Good electrical conductivity & enhanced ion transfer		Rate capability & a large voltage range
Reactivity (Wettability)	Redox-active functional groups	>	Surface functionalization by in-plane defects		Energy density, power density, cycle stability, applicability
Surface area	100 ~ 400 m^2 g^{-1}	<<	400 ~ 1200 m^2 g^{-1}		
Durability	Cross-linked covalent bonding structure	~	Physicochemical durability		
Aggregation	Polymer chains agglomeration	~	Graphene flakes re-stacking		Stable porosity
Synthesis process	BH coupling (catalytic amination)	~	Catalytic oxidation & reduction process		Facile synthesis

1.4.7 Symmetric and asymmetric supercapacitors

Supercapacitor devices consist of two electrodes immersed in an electrolyte and separated by an ion-permeable insulating film. Depending on how these two electrodes are designed, they can be classified into symmetric supercapacitors (SSCs) and asymmetric supercapacitors (ASCs) [4-6]. SSCs consist of two electrodes with the same material, while asymmetric supercapacitors consist of two electrodes with different materials.

In general, SSCs operate only within the voltage range of one material, and when using an aqueous electrolyte, the operating voltage is limited to 1.0 V or less due to the thermodynamic decomposition of water molecules. Although organic electrolytes can be used to increase the operating voltage range beyond 2.5 V, these organic electrolytes are sometimes toxic and hazardous to the environment [53]. On the other hand, since ASCs operate by combining the working voltages of different active electrode materials, they can achieve a wider working voltage even for aqueous electrolytes unlike SSCs [5]. ASCs mainly use redox-active materials (positive electrode) as an energy source and capacitive materials (negative electrode) as a power source [103]. Redox-active materials such as conductive polymers and transition metal compounds can achieve a more positive limit in the potential window, whereas capacitive materials such as carbon exhibit a higher overpotentials for hydrogen evolution, allowing the negative potential limit to be extended. Therefore, the fabrication of ASCs can be used as a strategy to increase the operating voltage window of full-cell devices by utilizing different voltage ranges of each electrode during the charge-discharge process [38,39,42,56]. Schematic illustrations and typical cyclic voltammetry curves of the SSCs and ASCs are displayed in Figure 1.14.

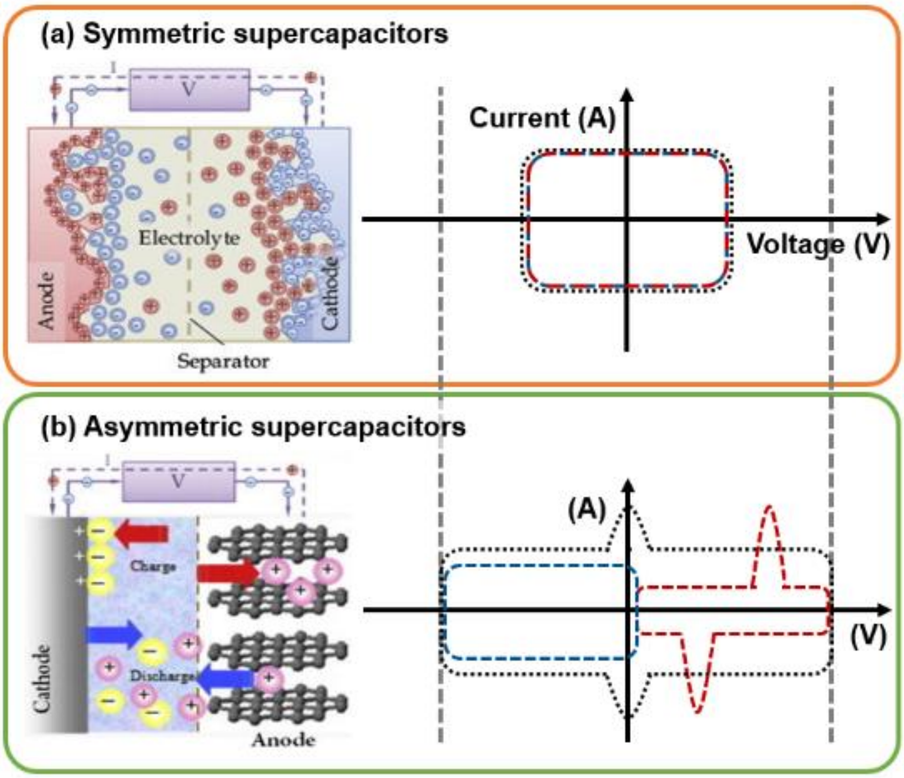

Figure 1.14. Schematic illustrations and typical cyclic voltammetry curves of (a) symmetric and (b) asymmetric supercapacitors [103].

1.5 Dissertation overview

As described above, carbon materials are most widely used as supercapacitor electrodes, but it need to overcome its relatively low energy density properties. To figure out the problems, various design strategies for electrode materials including a large surface area, stable porous structure, high conductivity, and additional redox properties have been investigated. This dissertation is mainly focused on the preparation, characterization, and evaluation of three-dimensional hierarchically porous nanocomposite electrodes composed of carbon materials and redox-active conductive polymers to develop high-performance flexible all-solid-state supercapacitors.

In the first part of chapter 2, a low-cost binder-free activated all-carbon electrode derived from modified potassium citrate has been prepared on the carbon cloth via a facile thermal decomposition and carbonization method. The hierarchically porous carbon tuned by potassium ion and a heating temperature shows unique stable morphology, a large surface area, and a good charge/ion conductivity. The optimized sample can be directly used as an electrode for flexible supercapacitor, and exhibits a remarkable capacitance, rate capability, energy density with a good cycle stability.

In the second part of chapter 2, a composite of redox-active conjugated microporous anthraquinonylamine-based polymer network and activated graphene has been prepared by facile one-step Buchwald-Hartwig coupling. The hierarchically porous hybrid of conductive polymer and activated graphene shows a large surface area and significant charge/ion conductivity.

An asymmetric supercapacitor is prepared by using the as-prepared hybrid and activated graphene as a positive and negative electrode, respectively. The flexible supercapacitor showed a high energy density with a good cycle stability.

1.6 References

[1] A.Q. Al-Shetwi, Sustainable development of renewable energy integrated power sector: trends, environmental impacts, and recent challenges, Sci. Total Environ. 822 (2022) 652–657.

[2] R.E.H. Sims, H.-H Rogner, K. Gregory, Carbon emission and mitigation cost comparisons between fossil fuel, nuclear and renewable energy resources for electricity generation, Energy Policy 31 (2003) 1315–1326.

[3] R. Hemmati, H. Saboori, Emergence of hybrid energy storage systems in renewable energy and transport applications – a review, Renew. Sust. Energ. Rev. 65 (2016) 11–23.

[4] M.-S. Son, J.-H. Ryu, Recent research trends of supercapacitors for energy storage systems, Clean Technol. 27 (2021) 277–290.

[5] A. Muzaffar, B. Ahamed, K. Deshmukh, J. Thirumalai, A review on recent advances in hybrid supercapacitors: design, fabrication, and applications, Renew. Sustain. Energy Rev. 101 (2019) 123–145.

[6] W. Raza, F. Ali, N. Raza, Y. Luo, K.-H. Kim, J. Yang, S. Kumar, A. Mehmood, E.E. Kwon, Recent advancements in supercapacitor technology, 52 (2018) 441–473.

[7] H. Helmholtz, Studies of electric boundary layers, Wied. Ann. 7 (1879) 337–382.

[8] G. Gouy, Constitution of the electric charge at the surface of an electrolyte, J. Phys. Theor. Appl. 9 (1910) 457–468.

[9] D.L. Chapman, A contribution to the theory of electrocapillarity, Philos. Mag. 25 (1913) 475–481.

[10] S. Balasubramaniam, A. Mohanty, S.K. Balasingam, S.J. Kim, A. Pamadoss, Comprehensive insight into the mechanism material selection and performance evaluation of supercapatteries, Nano-Micro Lett. 12 (2020) 85.

[11] A.G. Pandolfo, A.F. Hollenkamp, Carbon properties and their role in supercapacitors, J. Power Sources 19 (2006) 11–27.

[12] J.R. Miller, P. Simon, Electrochemical capacitors for energy management, Science 321 (2008) 651–652.

[13] X. Zhao, H. Tian, M. Zhu, K. Tian, J.J. Wang, F. Kang, R.A. Outlaw, Carbon nanosheets as the electrode material in supercapacitors, 194 (2009) 1208–1212.

[14] P. Dubey, V. Chrivastav, P.H. Maheshwari, S. Sundriyal, Recent advances in biomass derived activated carbon electrodes for hybrid electrochemical capacitor applications: challenges and opportunities, Carbon 170 (2020) 1–29.

[15] Y.-J. Gu, W. Wen, J. Wu, Simple air calcination affords commercial carbon cloth with high areal specific capacitance for symmetrical supercapacitors, J. Mater. Chem. A 6 (2018) 21078.

[16] L.-F. Chen, X.-D. Zhang, H.-W. Liang, M. Kong, Q.-F. Guan, P. Chen, Z.-Y. Wu, S.-H. Yu, Synthesis of nitrogen-doped porous carbon nanofibers as an efficient electrode material for supercapacitors, ACS Nano 6 (2012) 7092–7102.

[17] M. Sevilla, A.B. Fuertes, Direct synthesis of highly porous interconnected carbon nanosheets and their application as high-performance supercapacitors, ACS Nano 8 (2014) 5069–5078.

[18] D.K. Kim, N.D. Kim, S.-K. Park, K.-D. Seong, M. Hwang, N.-H. You, Y. Piao, Nitrogen doped carbon derived from polyimide/multiwall carbon nanotube composites for high performance flexible all-solid-state supercapacitors, J. Power Sources 380 (2018) 55–63.

[19] L. Sun, X. Wang, Y. Wang, Q. Zhang, Roles of carbon nanotubes in novel energy storage devices, Carbon 122 (2017) 462–474.

[20] Z. Cao, B.Q. Wei, A perspective: carbon nanotube macro-films for energy storage, Energy Environ. Sci. 6 (2013) 3183–3201.

[21] R. Raccichini, A. Varzi, S. Passerini, B. Scrosati, The role of graphene for electrochemical energy storage, Nat. Mater. 14 (2015) 271–279.

[22] X. Li, L. Zhi, Graphene hybridization for energy storage applications, Chem. Soc. Rev. 47 (2018) 3189–3216.

[23] W.H. Antink, Y. Choi, K.-D. Seong, J.M. Kim, Y. Piao, Recent progress in porous graphene and reduced graphene oxide-based nanomaterials for electrochemical energy storage devices, Adv. Mater. Interfaces 5 (2018) 1701212.

[24] Z. Chen, W. Ren, L. Gao, B. Liu, S. Pei, H.M. Cheng, Three-dimensional flexible and conductive interconnected graphene networks grown by chemical vapor deposition, Nat. Mater. 10 (2011) 424–428.

[25] B.G. Choi, M. Yang, W.H. Hong, J.W. Choi, Y.S. Huh, 3D macroporous graphene frameworks for supercapacitors with high energy and power densities, ACS Nano 6 (2012) 4020–4028.

[26] Y. Xu, K. Sheng, C. Li, G. Shi, Self-assembled graphene hydrogel via a one-step hydrothermal process, ACS Nano 4 (2010) 4324–4330.

[27] I.-H. Kim, J.-B. Kim, Electrochemical characterization of hydrous ruthenium oxide thin-film electrodes for electrochemical capacitor applications, J. Electrochem. Soc. 153 (2006) A383–A389.

[28] X.-H. Yang, Y.-G. Wang, H.-M. Xiong, Y.-Y. Xia, Interfacial synthesis of porous MnO_2 and its application in electrochemical capacitor, Electrochim. Acta 53 (2007) 752–757.

[29] D.-D. Zhao, S.-J. Bao, W.-J. Zhou, H.-L. Li, Preparation of hexagonal nanoporous nickel hydroxide film and its application for electrochemical capacitor, Electrochem. Commun. 9 (2007) 869–874.

[30] Z.J. Lao, K. Konstantinov, Y. Tournaire, S.H. Ng, G.X. Wang, H.K. Liu, Synthesis of vanadium pentoxide powders with enhanced surface-area for electrochemical capacitors, J. Power Sources 162 (2006) 1451–1454.

[31] Z. Fan, J. Chen, K. Cui, F. Sun, Y. Xu, Y. Kuang, Preparation and capacitive properties of cobalt-nickel oxides/carbon nanotube composites, Electrochim. Acta 52 (2007) 2959–2965.

[32] M.E. Abdelhamid, A.P. O'Mullane, G.A. Snook, Storing energy in plastics: a review on conducting polymers & their role in electrochemical energy storage, RSC Adv. 5 (2015) 11611–11626.

[33] I. Shown, A. Ganguly, L.-C. Chen, K.-H. Chen, Conducting polymer-based flexible supercapacitor, Energy Sci. Eng. 3 (2015) 2–26.

[34] M.E. Roberts, D.R. Wheeler, B.B. McKenzie, B.C. Bunker, High specific capacitance conducting polymer supercapacitor electrodes based on poly(tris(thiophenylphenyl)amine), J. Mater. Chem. 19 (2009) 6977–6979.

[35] R. Holze, Composites and copolymers containing redox-active molecules and intrinsically conducting polymers as active masses for supercapacitor electrodes–an introduction, Polymers 12 (2020) 1835.

[36] J. Kim, J.H. Kim, K. Ariga, Redox-active polymers for energy storage nanoarchitectonics, Joule 1 (2017) 739–768.

[37] Y. He, W. Chen, X. Li, Z. Zhang, J. Fu, C. Zhao, E. Xie, Freestanding three-dimensional graphene/MnO_2 composite networks as ultralight and flexible supercapacitor electrodes, ACS Nano 7 (2013) 174–182.

[38] P. Wen, P. Gong, J. Sun, J. Wang, S. Yang, Design and synthesis of Ni-MOF/CNT composites and rGO/carbon nitride composites for an asymmetric supercapacitor with high energy and power density, J. Mater. Chem. A 3 (2015) 13874–13883.

[39] S.-H. Ji, N.R. Chodankar, W.-S. Jang, D.-H. Kim, High mass loading of h-WO_3 and a-MnO_2 on flexible carbon cloth for high-energy aqueous asymmetric supercapacitor, Electrochim. Acta 299 (2019) 245–252.

[40] M. Yao, C. Guo, Q. Geng, Y. Zhang, X. Zhao, X. Zhao, Y. Wang, Construction of anthraquinone-containing covalent organic frameworks/graphene hybrid films for a flexible high-performance microsupercapacitor, Ind. Eng. Chem. Res. 61 (2022) 7480–7488.

[41] L. Yang, K. Zhuo, X. Xu, Z. Zhang, Q. Du, G. Bai, J. Wang, Anthraquinone-modified nitrogen-doped graphene aerogel for boosting energy density of supercapacitors by self-matching of capacity, Electrochim. Acta 393 (2021) 139057.

[42] Y. Zeng, Y. Han, Y. Zhao, Y. Zeng, M. Yu, Y. Liu, H. Tang, Y. Tong, X. Lu, Advanced Ti-doped Fe_2O_3@PEDOT core/shell anode for high-energy asymmetric supercapacitors, Adv. Energy Mater. 5 (2015) 1402176.

[43] D.R. Rolison, J.W. Long, J.C. Lytle, A.E. Fischer, C.P. Rhodes, T.M. McEvoy, M.E. Bourg, A.M. Lubers, Multifunctional 3D nanoarchitectures for energy storage and conversion, Chem. Soc. Rev. 38 (2009) 226–252.

[44] X. Chen, R. Paul, L. Dai, Carbon-based supercapacitors for efficient energy storage, Natl. Sci. Rev. 4 (2017) 453–489.

[45] D.-W. Wang, F. Li, M. Liu, G.Q. Lu, H.-M. Cheng, 3D aperiodic hierarchical porous graphitic carbon material for high-rate electrochemical capacitive energy storage. Angew. Chem.-Int. Edit. 47 (2008) 373–376.

[46] L. Qie, W. Chen, H. Xu, X. Xiong, Y. Jiang, F. Zou, X. Hu, Y. Xin, Z. Zhang, Y. Huang, Synthesis of functionalized 3D hierarchical porous carbon

for high-performance supercapacitors, Energy Environ. Sci. 6 (2013) 2497–2504.

[47] L. Yao, Q. Wu, P. Zhang, J. Zhang, D. Wang, Y. Li, X. Ren, H. Mi, L. Deng, Z. Zheng, Scalable 2D hierarchical porous carbon nanosheets for flexible supercapacitors with ultrahigh energy density, Adv. Mater. 30 (2018) 1706054.

[48] J. Chmiola, G. Yushin, Y. Gogotsi, C. Portet, P. Simon, P.L. Taberna, Anomalous increase in carbon capacitance at pore sizes less than 1 nanometer, Science 313 (2006) 1760–1763.

[49] C. Portet, G. Yushin, Y. Gogotsi, Effect of carbon particle size on electrochemical performance of EDLC. J. Electrochem. Soc. 155 (2008) A531–A536.

[50] W. Li, J. Liu, D. Zhao, Mesoporous materials for energy conversion and storage devices, Nat. Rev. Mater. 1 (2016) 16023.

[51] F. Rodríguez-Reinoso, M. Molina-Sabio, Activated carbons from lignocellulosic materials by chemical and/or physical activation: an overview, Carbon 30 (1992) 1111–1118.

[52] J. Wang, P. Nie, B. Ding, S. Dong, X. Hao, H. Dou, X. Zhang, Biomass derived carbon for energy storage devices, J. Mater Chem. A 5 (2017) 2411–2428.

[53] N. Guo, M. Li, X. Sun, R. Wang, R. Yang, Enzymatic hydrolysis lignin derived hierarchical porous carbon for supercapacitors in ionic liquids with high power and energy densities, Green Chem. 19 (2017) 2595–2602.

[54] L. Borchardt, M. Oschatz, S. Kaskel, Tailoring porosity in carbon materials for supercapacitor applications, Mater. Horiz. 1 (2014) 157–168.

[55] Y. Li, S. Roy, T. Ben, S. Xu, S. Qiu, Micropore engineering of carbonized porous aromatic framework for supercapacitors applications, Phys. Chem. Chem. Phys. 16 (2014) 12909–12917.

[56] P. Yu, Z. Zhang, L. Zheng, F. Teng, L. Hu, X. Fang, A novel sustainable flour derived hierarchical nitrogen-doped porous carbon/polyaniline electrode for advanced asymmetric supercapacitors, Adv. Energy Mater. 6 (2016) 1601111.

[57] Y. He, X. Zhuang, C. Lei, L. Lei, Y. Hou, Y. Mai, X. Feng, Porous carbon nanosheets: synthetic strategies and electrochemical energy related applications, Nano Today 24 (2019) 103–119.

[58] F.A. Ofori, F.A. Sheikh, R. Appiah-Ntiamoah, X. Yang, H. Kim, A simple method of electrospun tungsten trioxide nanofibers with enhanced visible-light photocatalytic activity, Nano-Micro Lett. 7 (2015) 291–297.

[59] Y. Dong, J. Shao, C. Chen, H. Li, R. Wang, Y. Chi, X. Lin, G. Chen, Blue luminescent graphene quantum dots and graphene oxide prepared by tuning the carbonization degree of citric acid, Carbon 50 (2012) 4738–4743.

[60] V. Strauss, K. Marsh, M.D. Kowal, M. El-Kady, R.B. Kaner, A simple route to porous graphene from carbon nanodots for supercapacitor applications, Adv. Funct. Mater. 30 (2018) 1704449.

[61] D.Y. Pan, S. Wang, B. Zhao, M.H. Wu, H.J. Zhang, Y. Wang, Z. Jiao, Li storage properties of disordered graphene nanosheets, Chem. Mater. 21 (2009) 3136–3142.

[62] F. Yao, F. Gunes, H.Q. Ta, S.M. Lee, S.J. Chae, K.Y. Sheem, C.S. Cojocaru, S.S. Xie, Y.H. Lee, Diffusion mechanism of lithium ion through basal plane of layered graphene, J. Am. Chem. Soc. 134 (2012) 8646–8654.

[63] J.H. Lee, N. Park, B.G. Kim, D.S. Jung, K. Im, J. Hur, J.W. Choi, Restacking-inhibited 3D reduced graphene oxide for high performance supercapacitor electrodes, ACS Nano 7 (2013) 9366–9374.

[64] L.L. Peng, Z.W. Fang, Y. Zhu, C.S. Yan, G.H. Yu, Holey 2D nanomaterials for electrochemical energy storage, Adv. Energy Mater. 8 (2018) 1702179.

[65] Y. Xu, Z. Lin, X. Zhong, X. Huang, N.O. Weiss, Y. Huang, X. Duan, Holey graphene frameworks for highly efficient capacitive energy storage, Nat. Commun. 5 (2014) 4554

[66] X. Zhao, C.M. Hayner, M.C. Kung, H.H. Kung, Flexible holey graphene paper electrodes with enhanced rate capability for energy storage applications, ACS Nano 5 (2011) 8739–8749.

[67] Z.Q. Jiang, B. Pei, A. Manthiram, Randomly stacked holey graphene anodes for lithium-ion batteries with enhanced electrochemical performance, J. Mater. Chem. A 1 (2013) 7775–7781.

[68] B.E. Conway, Electrochemical supercapacitors: scientific fundamentals and technological applications, Kluwer Academic/Plenum Publishers, New York, 1999, https://doi.org/10.1007/978-1-4757-3058-6.

[69] Y. Zhang, H. Feng, X. Wu, L. Wang, A. Zhang, T. Xia, H. Dong, X. Li, L. Zhang, Progress of electrochemical capacitor electrode materials: a review, Int. J. Hydrog. Energy 34 (2009) 4889–4899.

[70] T.B. Schon, B.T. McAllister, P.-F. Li, D.S. Seferos, The rise of organic electrode materials for energy storage, Chem. Soc. Rev. 45 (2016) 6345–6404.

[71] E.-T. Liu, S.-L. Mei, X.-H. Chen, C.-J. Yao, Conducting polymers with redox active pendant groups: their application progress as organic electrode materials for rechargeable batteries, J. Mater. Chem. C 10 (2022) 13570–13589.

[72] J.M. Gallmetzer, S. Kröll, D. Werner, D. Wielend, M. Irimia-Vladu, E. Portenkirchner, N.S. Sariciftci, T.S. Hofer, Anthraquinone and its derivatives as sustainable materials for electrochemical applications - a joint experimental and theoretical investigation of the redox potential in solution, Phys. Chem. Chem. Phys. 24 (2022) 16208–16219.

[73] H. Wang, R. Emanuelsson, H. Liu, K. Edström, F. Mamedov, M. Strømme, M. Sjödin, Redox-state-dependent interplay between Pendant group and conducting polymer backbone in quinone-based conducting redox polymers for lithium ion batteries, 2 (2019) 7162–7170.

[74] A.I. Cooper, Conjugated microporous polymers, Adv. Mater. 21 (2009) 1291–1295.

[75] Y. Xu, S. Jin, H. Xu, A. Nagai, D.L. Jiang, Conjugated microporous polymers: design, synthesis and application, Chem. Soc. Rev. 42 (2013) 8012–8031.

[76] J.M. Lee, A.I. Cooper, Advances in conjugated microporous polymers, Chem. Rev. 120 (2020) 2171–2214.

[77] J.-X. Jiang, F.B. Su, A. Trewin, C.D. Wood, H.J. Niu, J.T.A. Jones, Y.Z. Khimyak, A.I. Cooper, Synthetic control of the pore dimension and surface area in conjugated microporous polymer and copolymer networks, J. Am. Chem. Soc. 130 (2008) 7710–7720.

[78] F. Vilela, K. Zhang, M. Antonietti, Conjugated porous polymers for energy applications, Energy Environ. Sci. 5 (2012) 7819–7832.

[79] K. Amin, N. Ashraf, L. Mao, C.F.J. Faul, Z. Wei, Conjugated microporous polymers for energy storage: recent progress and challenges, Nano energy. 85 (2021) 105958.

[80] T. Sun, J. Xie, W. Guo, D.-S. Li, Q. Zhang, Covalent-organic frameworks: advanced organic electrode materials for rechargeable batteries, Adv. Energy Mater. 10 (2020) 1904199.

[81] H.G. Wang, Z.H. Cheng, Y.Z. Liao, J.H. Li, J. Weber, A. Thomas, C.F.J. Faul, Conjugated microporous polycarbazole networks as precursors for nitrogen-enriched microporous carbons for CO_2 storage and electrochemical capacitors, Chem. Mater. 29 (2017) 4885–4893.

[82] X. Liu, C.-F. Liu, S. Xu, T. Cheng, S. Wang, W.-Y. Lai, W. Huang, Porous organic polymers for high-performance supercapacitors, Chem. Soc. Rev. 51 (2022) 3181–3225.

[83] Y. Zhang, B. Zhang, L. Chen, T. Wang, M. Di, F. Jiang, X. Xu, S. Qiao, Rational design of covalent triazine frameworks based on pore size and heteroatomic toward high performance supercapacitors, J. Colloid Interface Sci. 606 (2022) 1534–1542.

[84] A.S. Guram, R.A. Rennels, S.L. Buchwald, A simple catalytic method for the conversion of aryl bromides to arylamines, Angew. Chem.-Int. Edit. 34 (1995) 1348–1350.

[85] J. Louie, J.F. Hartwig, Palladium-catalyzed synthesis of arylamines from aryl halides. Mechanistic studies lead to coupling in the absence of tin reagents, Tetrahedron Lett. 36 (1995) 3609–3612.

[86] Y.Z. Liao, J. Weber, B.M. Mills, Z.H. Ren, C.F.J. Faul, Highly efficient and reversible iodine capture in hexaphenylbenzene-based conjugated microporous polymers, Macromolecules 49 (2016) 6322–6333.

[87] H. Li, W. Lyu, Y. Liao, Engineering redox activity in conjugated microporous polytriphenylamine networks using pyridyl building blocks toward efficient supercapacitors, Macromol. Rapid Commun. 40 (2019) 1900455.

[88] Y.Z. Liao, J. Weber, C.F.J. Faul, Conjugated microporous polytriphenylamine networks, Chem. Commun. 50 (2014) 8002–8005.

[89] Y. Liao, H. Wang, M. Zhu, A. Thomas, Efficient supercapacitor energy storage using conjugated microporous polymer networks synthesized from Buchwald-Hartwig coupling, Adv. Mater. 30 (2018) 1705710.

[90] R. Shi, C. Han, H. Duan, L. Xu, D. Zhou, H. Li, J. Li, F. Kang, B. Li, G. Wang, Redox-active organic sodium anthraquinone-2-sulfonate (AQS) anchored on reduced graphene oxide for high-performance supercapacitors, Adv. Energy Mater. 8 (2018) 1802088.

[91] X. Chen, H. Wang, H. Yi, X. Wang, X. Yan, Z. Guo, Anthraquinone on porous carbon nanotubes with improved supercapacitor performance, J. Phys. Chem. C 118 (2014) 8262–8270.

[92] L. Gao, S. Gan, H. Li, D. Han, F. Li, Y. Bao, L. Niu, Self-assembling graphene-anthraquinone-2-sulphonate supramolecular nanostructures with enhanced energy density for supercapacitors, Nanotechnology 28 (2017) 275602.

[93] Y.-G. Wang, H.-Q. Li, Y.-Y. Xia, Ordered whisker-like polyaniline grown on the surface of mesoporous carbon and its electrochemical capacitance performance, Adv. Mater. 18 (2006) 2619–2623.

[94] Y. Zhou, Z.-Y. Qin, L. Li, Y. Zhang, Y.-L. Wei, L.-F. Wang, M.-F. Zhu, Polyaniline/multi-walled carbon nanotube composites with core-shell structures as supercapacitor electrode materials, Electrochim. Acta 55, (2010) 3904–3908.

[95] W. Lyu, W. Zhang, H. Liu, Y. Liu, H. Zuo, C. Yan, C.F.J. Faul, A. Thomas, M. Zhu, Y. Liao, Conjugated microporous polymer network grafted carbon nanotube fibers with tunable redox activity for efficient flexible wearable energy storage, Chem. Mater. 32 (2020) 8276–8285.

[96] L. Zhang, D. Han, Y. Tao, C. Cui, Y. Deng, X. Dong, W. Lv, Z. Lin, S. Wu, Z. Weng, Q.-H. Yang, Dense organic molecules/graphene network anodes with superior volumetric and areal performance for asymmetric supercapacitors, J. Mater. Chem. A 8 (2020) 461–469.

[97] Z. Xu, Y. Liu, Z. Wu, R. Wang, Q. Wang, T. Li, J. Zhang, J. Cheng, Z. Yang, S. Chen, M. Miao, D. Zhang, Construction of extensible and flexible supercapacitors from covalent organic framework composite membrane electrode, Chem. Eng. J. 387 (2020) 124071.

[98] A.M. Khattak, H. Sin, Z.A. Ghazi, X. He, B. Liang, N.A. Khan, H.R. Alanagh, A. Iqbal, L. Li, Z. Tang, Controllable fabrication of redox-active

conjugated microporous polymers on reduced graphene oxide for high performance faradaic energy storage, J. Mater. Chem. A 6 (2018) 18827–18832.

[99] Y. Qin, J. Li, X. Jin, S. Jiao, Y. Chen, W. Cai, R. Cao, Anthraquinone-functionalized graphene framework for supercapacitors and lithium batteries, Ceram. Int. 46 (2020) 15379–15384.

[100] M. Jia, Y. Li, L. Cui, Y. An, C. Pan, X. Jin, An anthraquinone-decorated graphene hydrogel based on carbonized cotton fibers for flexible and high-performance supercapacitors, Sustain. Energ. Fuels 5 (2021) 862–873.

[101] R. Kötza, M. Carlen, Principle and applications of electrochemical capacitors, Electrochim. Acta 45 (2000) 2483–2498.

[102] L.L. Zhang, X.S. Zhao, Carbon-based materials as supercapacitor electrodes, Chem. Soc. Rev. 38 (2009) 2520–2531.

[103] N. Choudhary, C. Li, J.L. Moore, N. Nagaiah, L. Zhai, Y.W. Jung, J. Thomas, Asymmetric supercapacitor electrodes and devices, Adv. Mater. 29 (2017) 1605336.

Chapter 2. Hierarchically porous carbon/polymer composites for supercapacitor electrode materials

Chapter 2.1 Self-organized hierarchically porous carbon coated on carbon cloth for high-performance freestanding supercapacitor electrodes

[Jang et al., J. Electroanal. Chem. 895 (2021) 115456]

2.1.1 Motivation

Great efforts have been made to prepare freestanding and binder-free electrodes with favorable mechanical strength and large capacitance to provide a vital component for flexible supercapacitor. Commercial carbon cloth composed of carbon fibers is routinely employed as a conductive substrate for flexible supercapacitor. However, the conventional carbon fiber cannot be used as an electrode because its energy capacity is significantly low. To develop high-performance flexible supercapacitor electrodes, activation method for carbon fiber such as etching, functionalization, and active material coating have been proposed [1-3]. In the case of simple etching methods of carbon fiber, there is an advantage of improving the surface area, but it is easy to lose the flexibility of substrate (current collector) due to the damage of fiber. The introduction of chemical functional groups can activate the electrode surface evenly, but there is a limit to maximizing the specific capacitance of existing fibers. Therefore, in recent years, methods of coating active materials, i.e., active carbon, conductive polymer, and transition metal, are preferred. Among them, the most cost-effective and environmentally friendly method for improving performance is growing activated carbon on carbon fiber (coating method).

Activated carbons, which are also called porous carbons, with tunable pore size and structure are significantly important when adapting to supercapacitor application [4,5]. As mentioned in chapter 1, it shows advantages, i.e., good electronic conductivity, high durability, low cost, and benign environmental availability. Self-template method is regarded as a simple way to prepare hierarchically porous carbons. One of the most widely known methods is in situ pyrolysis through heat treatment in inert atmosphere of bio-mass existing as metal-organic compounds. Taking potassium citrate as an example, the organic moiety becomes a raw material for carbonization, and the potassium ions cause a thermal catalytic reaction during the heat treatment [6]. Due to this, the carbide generation and the decomposition are promoted inside the salt to generate defects, which maximizes the porosity. As a result, the as-prepared activated carbon with hierarchically porous structure can be used as supercapacitor electrode materials. However, this preparation method exhibits a very low carbonization yield, and produce activated carbon powders. This causes a disadvantage that mass production of the active material is difficult, and an additional electrode manufacturing process is required. In addition, the binder used in the electrode manufacturing process causes a dramatic decrease in the performance of the active material. Therefore, it was needed to develop a manufacturing method for an all-carbon-type freestanding, and flexible active electrode that can be prepared in an easy and efficient way and can be used directly as an electrode.

Herein, we report a facile procedure for the fabrication of self-organized hierarchically porous carbon coated on carbon cloth (PCC) by using a pyrolysis of modified potassium citrate, which can be directly employed as a supercapacitor electrode. A mixture of citric acid and potassium hydroxide was preheated to obtain a sticky homogeneous gel with high carbon content to facilitate loading and carbonization process. The concentration of potassium hydroxide and the temperature for carbonization were tuned to obtain optimal porous carbon structure. Benefiting from its good electrolyte accessibility and fast charge transfer ascribed to its unique and stable multiscale porosity the resulting PCCs exhibits high capacitance, outstanding rate capability, and cycle stability. More importantly, an all-solid-state supercapacitor device made by using the optimized PCCs shows high volumetric energy and powder densities, excellent cycle stability, and mechanical flexibility.

2.1.2 Experiment

2.1.2.1 Materials

Citric acid anhydrous (CA, $C_6H_8O_7$, 99.5%), potassium hydroxide (KOH, 95%), potassium citrate ($K_3C_6H_5O_7$), hydrochloric acid (HCl, 35.0-37.0%), and ethanol (95.0%) were purchased from Samchun Chemicals. Deionized water used in this work was obtained by using a Milli-Q ultrapure water system (Millipore, USA). Carbon cloth (CC, W0S1002) was obtained from Nara Cell-Tech Corporation. Polyvinyl alcohol (PVA) was obtained from Sigma-Aldrich. All chemicals were of analytical grade and used as received without further purification.

2.1.2.2 Preparation of PCCs

As a precursor, CA-KOH gel was prepared by a thermochemical decomposition (pyrolysis) method. Initially, 50 mmol (9.6 g) of CA was put into a 100 mL of vial and heated at 160 °C in an ambient atmosphere for 1 hour and cooled down to room temperature. While heating, the CA was liquefied and partially decomposed that the color of solution changed from colorless to bright orange. When the temperature of solution was below 90 °C, 2 mL of deionized water was added drop wise under vigorous stirring to prevent solidification till the solution was cooled down to the room temperature, then a viscous gel-like solution was formed. As an activation agent, a different amount of KOH (i.e., 10, 20, and 40 mmol) was added into the solution and dissolved completely for 2 hours under vigorous stirring at room temperature.

To prepare substrates, a commercial carbon cloth (CC) was treated with a mixture solution of deionized water/ethanol (7/3 v/v) at 80 °C for 12 hours. After washing with the same solution several times, the treated CC was dried in a vacuum oven at 60 °C overnight. Finally, the CC was cut into a small piece with size of 1×5 cm^2 for further use.

A desired amount of the as-prepared CA-KOH gel was soaked uniformly upon a 1×1 cm^2 area of the CC and dried. Then, the precursor loaded CC was heated using a tubular furnace for 1 hour under argon (Ar) gas flow for carbonization and activation. After thermal treatment, all samples were washed with a 3 M HCl aqueous solution, deionized water, and ethanol for three times, respectively, to remove salts and impurities, and dried in a vacuum oven at 60 °C for overnight.

In terms of CA/KOH ratio, the amounts of KOH in precursor were 10, 20, and 40 mmol while the amount of CA was fixed at 50 mmol. For comparison of electrode samples, the as-prepared PCCs were denoted as PCC-0 (no KOH), PCC-10, PCC-20, and PCC-40, respectively, corresponding to a molar ratio of CA:KOH (50:0, 50:10, 50:20, and 50:40). In this study, PCC-20 showed the best features for further analysis.

After confirming the best precursor condition, the thermal treatment was performed at 500, 600, 700, and 800 °C. Then, the resultant PCCs were denoted as PCC-500, PCC-600, PCC-700, and PCC-800, respectively, corresponding to a target temperature. In this work, the best performance was obtained from PCC-700, which was carbonized at 700 °C.

2.1.2.3 Material characterization

The morphology of samples was monitored by field-emission scanning electron microscopy (FE-SEM, S-4800, Hitachi) at 15kV and high-resolution transmission electron microscopy (HRTEM, JEM-2100, JEOL) at 200kV. Thermo gravimetric analysis (TGA) was performed by using a thermogravimeter (TGA/DSC 1, Mettler Toledo) to define reaction behaviors of materials in the temperature range of 25-900 °C with a heating rate of 5 min^{-1}. Surface elemental analysis was inspected by X-ray photoelectron spectroscopy (XPS) using ESCA spectrometer (SIGMA PROBE, Thermo Fisher Scientific) via a monochromatic Al Kα radiation source. X-ray diffraction (XRD) patterns of the samples were obtained in a scan range of 10°-80° using an X-ray diffractometer (New D8 Advance, Bruker) equipped with a Cu Kα radiation source operating at 40 kV and 40 mA. Nitrogen adsorption/desorption isotherms were acquired by using BELSORP-mini II (MicrotracBEL) at 77K with increasing gas pressure up to 1.0 bar. The specific surface area and pore distribution of the samples were calculated by a Brunauer-Emmett-Teller (BET) and Barrett-Joyner-Halenda (BJH) method, respectively. Raman spectroscopy was measured using Raman spectrometer (Horiba, LabRAM HR Evolution) with an excitation wavelength of 514 nm.

2.1.2.4 Electrochemical characterization

Both three-electrode and two-electrode (i.e., full-cell) configurations were applied to evaluate electrochemical performances of the fabricated PCCs. Cyclic voltammetry (CV) and galvanostatic charge/discharge (GCD) measurements were performed by using an electrochemical workstation (CHI 660E, CH Instruments Inc.). Electrochemical impedance spectroscopy (EIS) measurements were performed using ZIVE SP1 (ZIVE Lab) by applying an AC voltage with 10 mV amplitude in a frequency range from 100 kHz to 0.01 Hz at open-circuit voltage. Nyquist plot data was collected and fitted by ZMAN software (ZIVE Lab).

Prior to beginning a full-cell demonstration, electrochemical properties of the fabricated PCCs were examined in a three-electrode system to verify the optimized conditions for practical application. The as-prepared PCC was directly used as working electrodes in the three-electrode system. A mercury/mercury oxide (Hg/HgO) electrode was used as a reference electrode and a platinum (Pt) mesh was used as a counter electrode.

The loading mass of porous carbon coated on CC was fixed as 1 mg cm^{-2} and compared specific capacitance to optimize the amount of KOH and the temperature for carbonization of PCCs. Electrochemical measurements were performed at room temperature in 6 M KOH aqueous solution as an electrolyte. CV of PCCs was performed at different scan rates from 10-100 mV s^{-1} in potential range from -1.0 to 0.0 V (vs. Hg/HgO). GCD measurement of the PCCs was carried out with different current densities in potential range from -1.0 to 0.0 V (vs. Hg/HgO). After confirming the optimized condition of PCC, the loading mass of samples was increased from 1 to 5.5 mg cm^2, then compare the areal capacitance.

To measure the electrochemical performance of full-cell device, the PCCs with optimized properties were used to fabricate an all-solid-state symmetric supercapacitor. The loading mass of porous carbon coated on CC was fixed at 5.5 mg cm^{-2}. To prepare a PVA-KOH electrolyte solution, 3 g of PVA was added into 30 mL of deionized water and heated to 95 °C with a vigorous stirring for 1 hour until a clear homogeneous solution was obtained. 10 mL of KOH aqueous solution (0.15 mg mL^{-1}) was added into the PVA solution and mixed under a vigorous stirring for 2 hours. Two pieces of PCCs were soaked in PVA-KOH electrolyte for 1 hour to allow the electrolyte to uniformly wet the electrodes. The two electrodes were sandwiched together with filter paper as a separator and then dried in a fume hood for 5 hours at room temperature to evaporate the water. A working area of the samples was 1.0 cm^2 and a thickness of CC was 0.036 cm. The total volume of the as-prepared symmetric supercapacitors was 0.1 cm^3. To study the electrochemical performance of the symmetric supercapacitors, CV measurement were performed in a potential window range of 0.0-1.0 V at different scan rates from 10 to 100 mV s^{-1}. GCD measurements were conducted at a potential window ranging from 0.0 to 1.0 V at current densities ranging from 1 to 50 mA/cm^2. The specific capacitance from GCD measurements was calculated according to the following equation (1):

$C_s = (I\times\Delta t)/(\Delta V\times m)$ (1)

where C_s (F g^{-1}), I (A), Δt (s), ΔV (V), and m (g) represent the specific capacitance measured in a three-electrode configuration, the discharge current, the discharge time, the potential window, and the mass of active materials in one electrode, respectively. The areal and volumetric capacitance, C_a (F cm^{-2}), C_v (F cm^{-3}), were calculated by replacing the mass of active materials (m, g) with an area (a, cm^2) or volume (v, cm^3) of PCC electrodes, respectively.

The volumetric energy and the power densities of the full-cell device were calculated according to the following equations (2,3):

$E_v = (0.5/3600)\cdot C_v\cdot \Delta V^2$ (2)

$P_v = 3600\cdot E_v\cdot \Delta t^{-1}$ (3)

where E_v (Wh cm^{-3}), C_v (F cm^{-3}), ΔV (V), P_v (W cm-3), and Δt (s) represent the volumetric energy, the volumetric capacitance, the discharging potential range, the volumetric power, and the discharging time, respectively.

2.1.3 Results and discussion

The schematic illustration of the fabrication of self-organized hierarchically porous carbon on carbon cloth (PCC) via thermal carbonization process is shown in Figure 2.1a. Potassium citrate is well known as a proper source of two-dimensional (2D) porous carbon nanosheets [6]. According to the mechanism of pyrolysis and gasification processes, organic moiety is a carbon source and potassium ion has an essential role in the multi-step developments of microporous network as a noble catalyst. Potassium carbonate is formed at about 650 °C and then further decomposed to K_2O ($K_2CO_3 \rightarrow CO_2 + K_2O$). The as produced CO_2 reacts with carbon ($CO_2 + C \rightarrow 2CO$) to generate microporosity and the metallic potassium is produced via the reduction of K_2O by carbon ($K_2O + C \rightarrow 2K + CO$). In this study, we used CA as a carbon source and KOH as a catalyst for hierarchically porous carbon networks. The gel formation method with controlled amounts of KOH was performed to obtain PCC electrodes with desired features. The homogeneous CA-KOH gel-type solution was prepared by thermochemical decomposition method. Then the mixture was distributed on the carbon cloth (CC) and filled into gaps of each carbon fibers, which is subsequently set as it dried. This method was chosen because of the reasons bellow. First, lower melting point of CA (153 °C) compared to that of potassium citrate (over 180 °C) facilitates thermal gelation of the mixture upon heating at 160 °C and avoid rapid decomposition of citrate molecules that takes place at 175 °C. This method can solve the main obstacle for precursors loading upon CC surface coming from the low viscosity of potassium citrate aqueous solution. Second, facile control of potassium to citric acid molar ratio is desired because while potassium serves as a catalyst in carbonization processes, excessive potassium ion may disturb connection of porous carbons and the surface of CC due to the over-activation. By using KOH, the amount of potassium in precursor gel can be easily adjusted.

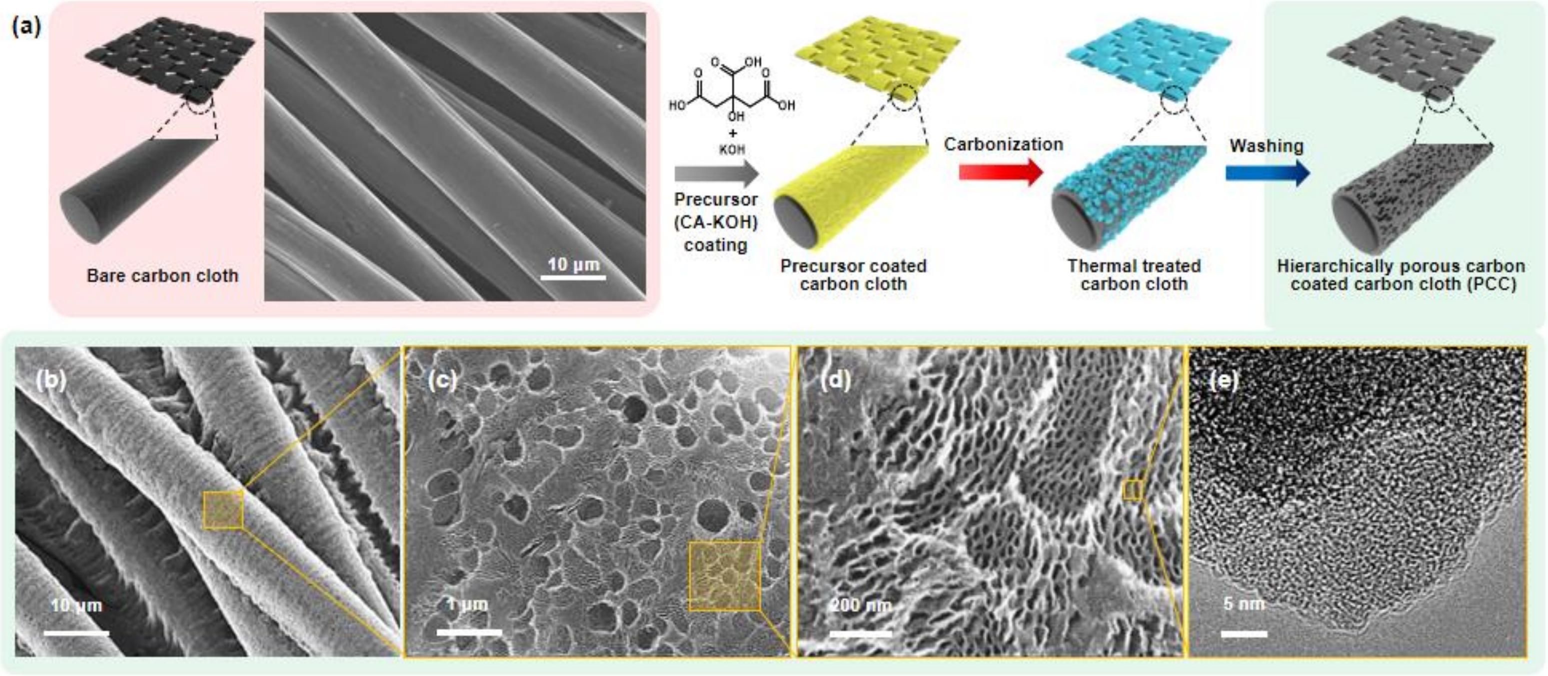

Figure 2.1. (a) Schematic illustration of the fabrication of PCCs; (b-d) FE-SEM and (e) HR-TEM images of the optimized PCC with different magnification.

To confirm the enhancement of thermal stability of porous carbon by introducing KOH, thermogravimetric analysis (TGA) was carried out for potassium citrate ($K_3C_6H_5O_7$), citric acid (CA, $C_6H_8O_7$), and a mixture of CA-KOH with a molar ratio of CA to KOHs at 50:20 (for PCC-20) (see Figure 2.2). CA was melted and decomposed around 153 °C and 0 % of weight was observed at 700 °C. Potassium citrate exhibited a lower weight loss than CA owing to the synthesized carbon catalyzed by potassium salts [6]. The CA-KOH mixture for PCC-20 had more weight residues than CA at higher temperature, indicating that KOH homogeneously mixed with CA enhanced thermal stability of CA during heat treatment and potassium ion assisted the synthesis of graphitic carbon network.

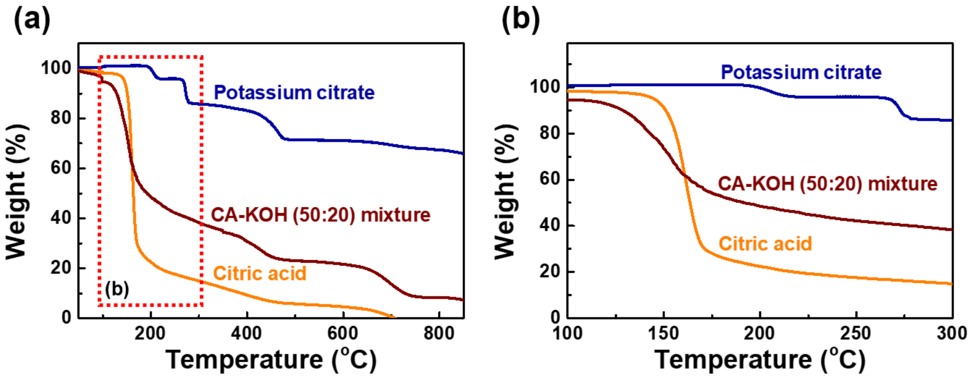

Figure 2.2. (a) TGA curves of potassium citrate ($K_3C_6H_5O_7$), citric acid (CA, $C_6H_8O_7$), and a mixture of CA-KOH; (b) Enlarged TGA curves of the region enclosed by the dashed red box in (a).

The morphology of PCCs was investigated by field-emission scanning electron microscopy (FE-SEM). Figure 2.1b-d and Figure 2.3 show FE-SEM images of PCC-0, PCC-10, PCC-20, and PCC-40 carbonized at 700 °C. Without KOH, i.e., PCC-0, it was difficult to observe carbon layers on CC surface before and after washing due to a complete decomposition of CA at 700 °C, as we predicted from the TGA data in Figure 2.2. The PCC-0 exhibits similar surface morphology compared to that of bare CC in Figure 2.1a. As the amount of KOH increased, thick porous carbon layers were formed on a surface of CC. However, the excessive amount of KOH reduced the porous carbon attached on CC after washing because of over activation process as shown in Figure 2.3c and f. These results demonstrate that KOH plays a significant role in the formation of hierarchically porous carbon structure on the surface of CC. The effect of varying carbonization temperature was also studied (see Figure 2.4). When samples were carbonized at 500, 600, and 700 °C in Ar atmosphere, porous carbon layer was well maintained on the CC surface after washing. However, when elevating the carbonization temperature to 800 °C, most of the porous carbon layers are eliminated due to an over activation. According to the morphological features, the optimal carbonization temperature for PCC was 700 °C for further characterization.

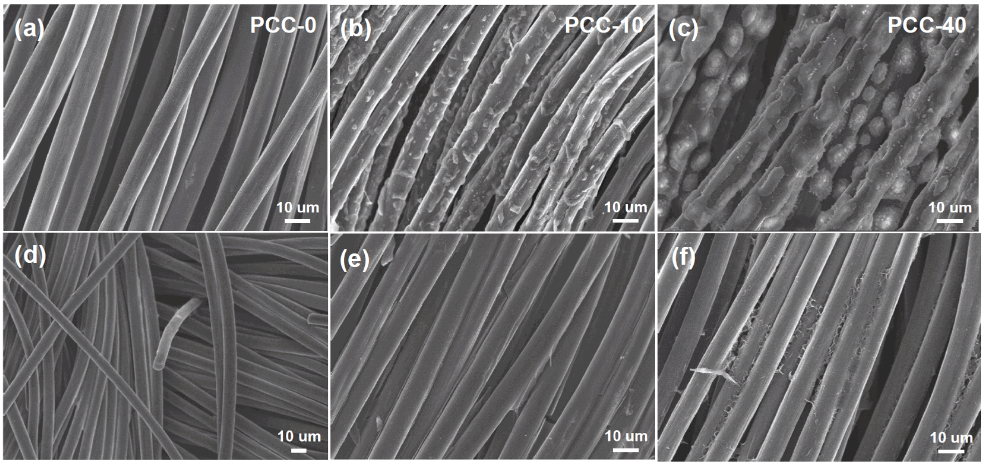

Figure 2.3. FE-SEM images of (a, d) PCC-0, (b, e) PCC-10, and (c, f) PCC-40; (a, b, c) before washing and (d, e, f) after washing. The carbonization temperature was fixed at 700 °C.

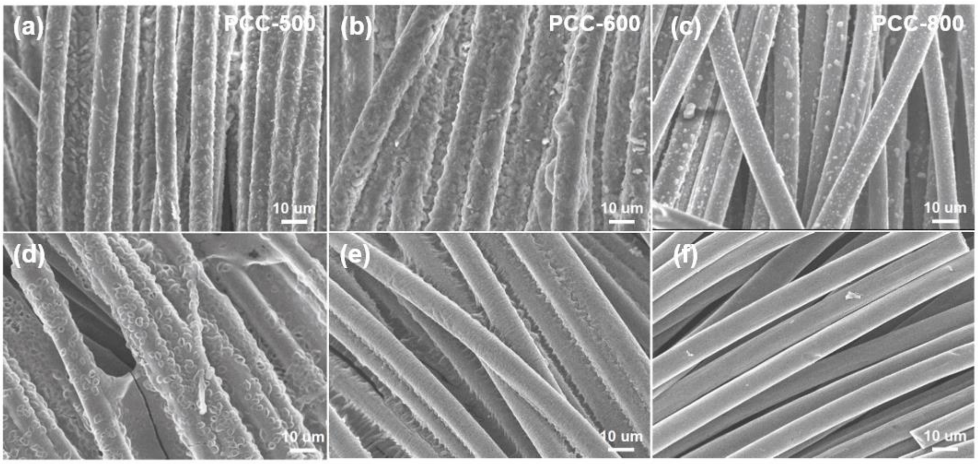

Figure 2.4. FE-SEM images (a, d) PCC-500, (b, e) PCC-600, and (c, f) PCC-800; (a, b, c) before washing and (d, e, f) after washing. As a precursor, the molar ratio of CA-KOH was fixed at 50:20.

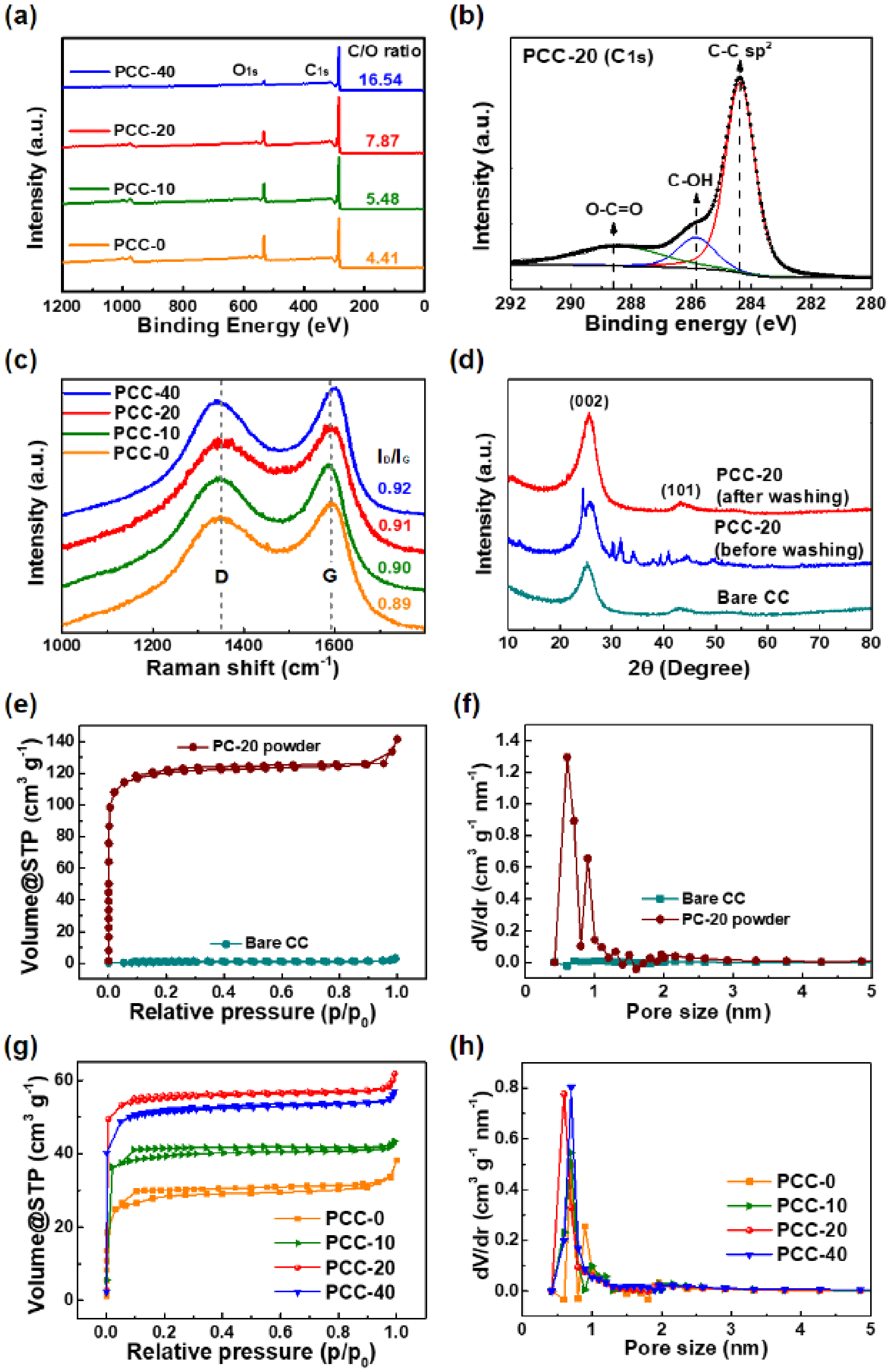

Figure 2.5. (a) XPS survey scanning spectra of PCCs, i.e., PCC-0, PCC-10, PCC-20, and PCC-40; (b) core-level high-resolution C 1s spectra of PCC-20; (c) Raman spectra of PCCs; (d) XRD patterns of PCC-20; (e, g) N_2 adsorption/ desorption isotherms and (f, h) BJH pore distribution diagrams of PCCs.

X-ray photoelectron spectroscopy (XPS) was conducted to explain the elemental configuration of the as-prepared powder of PCC-20 carbonized at 700 °C (see Figure 2.5a). The XPS spectra ranging from 0 to 1,200 eV showed that the sample was composed of carbon (C_{1s}) and oxygen (O_{1s}) without impurities resulted from potassium ion and the C/O ratio was 5.05. The deconvolution of XPS peaks assigned to C_{1s} components exhibited three distinctive peaks at 284.4, 285.8, and 288.4 eV, which are corresponding to C-C sp2 carbon, C-OH carbon, and O-C=O carbon, respectively (see Figure 2.5b) [7,8]. These functional groups can further enhance the wettability of carbon electrodes surface and increase pseudocapacitive property via Faradic reaction. These results strongly support that the as-prepared activated carbon coated on CC can satisfy electrical requirements for supercapacitors. To clarify the activation degree and defects in the sample, Raman spectroscopy measurement was carried out with an excitation wavelength of 514 nm (see Figure 2.5c). Raman spectra show two distinguished peaks at approximately 1350 and 1590 cm^{-1} corresponding to the D band for defects or disorders derived from the breathing mode of aromatic ring and G band from in-plane stretching vibration of the graphitic lattice which are corresponding to a sp^2 carbon atoms, respectively [9-11]. The intensity of D peak (I_D) is mainly attributed to the nano-sized defects of carbonaceous materials that the intensity ratios of the D band to the G band (I_D/I_G) of materials are generally considered as a degree of activation. In other words, the more activated sample has the higher I_D/I_G ratio in Raman spectra. The I_D/I_G ratios of the PCC-0, PCC-10, PCC-20, and PCC-40 were evaluated as 0.889, 0.898, 0.909, and 0.916, respectively, which means as the amount of KOH increased, the degree of the formation of porous carbon layers with nano-sized defects also increased, which agrees with results of XPS and nitrogen adsorption/desorption isotherm. The XRD pattern of bare CC and PCC-20s presents two broad peaks centered at 25.5° and 43° assigned to (002) and (101) planes of carbon, respectively (see in Figure 2.5d). In addition, potassium-related peaks are observed in the XRD pattern of PCC-20 (before washing), implying that inorganic impurities were clearly eliminated by washing step using HCl solution. These results are consistent with the XPS analysis, as shown in Figure 2.5a.

Nitrogen (N_2) adsorption/desorption isotherm and pore size distribution were measured at 77 K with an increasing gas pressure up to 1.0 bar. Prior to the PCCs demonstration, N_2 adsorption/desorption isotherm of bare CC and porous carbon powder of the as-prepared PCC-20 (denoted as PC-20 powder) was measured. As shown in Figure 2.5e and f, the surface area of bare CC was 2.53 $m^2\ g^{-1}$ but the PC-20 powder exhibited 461.6 $m^2\ g^{-1}$. A total pore volume the PC-20 was 0.432 $cm^3\ g^{-1}$ similar to that of other porous carbon powders synthesized by pyrolysis and activation of organic precursors [12,13]. When it comes to isotherm curves of the PCC-0, PCC-10, PCC-20, and PCC-40 samples as shown in Figure 2.5g and h, characteristic steep rise in the low relative pressure range (i.e., $p/p_0 < 0.01$) was clearly appeared suggesting that microporous carbon matrix was formed. By using a Brunauer-Emmett-Teller (BET) and Barrett-Joyner-Halenda (BJH) methods, the specific surface areas were calculated to be 106.5, 153.6, 220.8, and 200.5 $m^2 g^{-1}$, respectively, and their total pore volumes were 0.131, 0.142, 0.198, and 0.185 $cm^3 g^{-1}$, respectively. Moreover, the related micropore volumes were found to be 0.0458, 0.0663, 0.0927, and 0.0862 $cm^3 g^{-1}$, respectively, implying that the hierarchically porous carbon structures of the samples are composed of numerous micropores compared to the total pore volumes of each sample. The PCC-20 had the largest specific surface area which can further contributes to electrochemical performance. Detailed structural properties of the samples are also listed in Table 2.1.

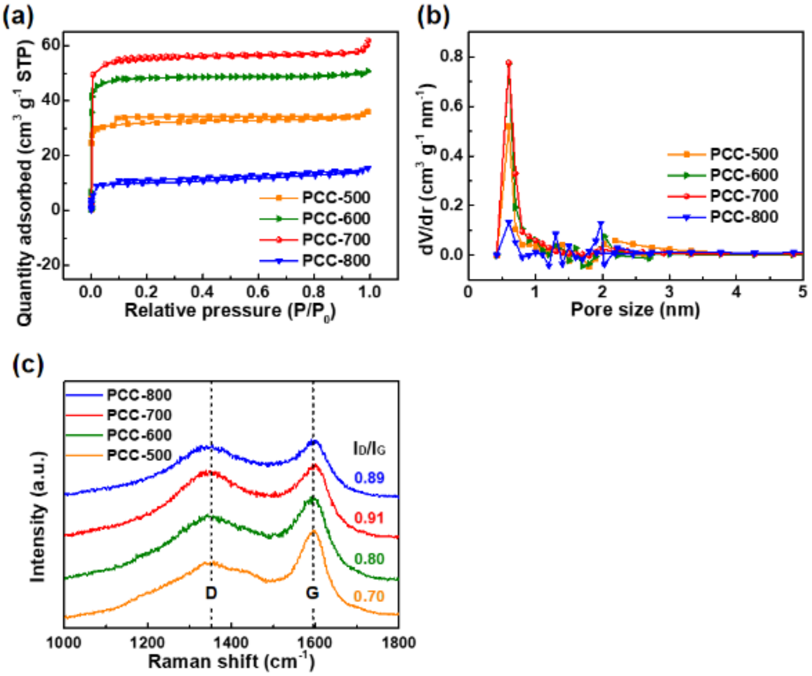

Figure 2.6. (a) N_2 adsorption/desorption isotherms, (b) pore size distributions, and (c) Raman spectra of the as-prepared PCC-500, PCC-600, PCC-700, and PCC-800.

To clarify the effect of carbonization temperature to structural properties of samples, nitrogen adsorption/desorption isotherm, pore size distribution, and Raman spectra of the PCC-20s which is prepared with different thermal temperature named as PCC-500, PCC-600, PCC-700, and PCC-800 were conducted. As shown in Figure 2.6a, the hysteresis curves in nitrogen adsorption/ desorption isotherm of PCC-500, PCC-600, PCC-700, and PCC-800 show characteristic steep rise in the low relative pressure range (i.e., $p/p_0 < 0.01$), which implies that microporous carbon matrix is formed. By using a BET and BJH methods, the specific surface areas are calculated to be 127.0, 193.7, 220.8, and

38.2 m^2 g^{-1}, respectively, and their total pore volumes are 0.108, 0.158, 0.198, and 0.043 cm^3 g^{-1}, respectively. BET surface area increases when the carbonization temperature is increased from 500 to 700 ^oC due to a formation of pores. However, the surface area of PCC-800 dramatically decreases because the porous carbon structure is collapsed due to an over-activation. These results are demonstrated by pore size distribution data as shown in Figure 2.6b and the related micropore volumes which is found to be 0.053, 0.080, 0.093, and 0.019 for PCC-500, PCC-600, PCC-700, and PCC-800, respectively. The PCC-700 shows the largest specific surface area and pore volume which can further contributes to electrochemical performance. Detailed structural properties of the samples are listed in Table 2.1. As shown in Figure 2.6c, Raman spectroscopy measurement for PCC-500, PCC-600, PCC-700, and PCC-800 was also conducted to clarify the degree of graphitization by comparing the I_D/I_G ratio of each sample. The position of D and G peak is similar to that of PCCs with different ratio of KOH (about 1350 and 1590 cm^{-1} corresponding to the D and G band, respectively). The I_D/I_G ratios of the PCC-500, PCC-600, PCC-700, and PCC-800 are evaluated as 0.70, 0.80, 0.91, and 0.89, respectively. This result indicates that activation degree of carbon layers on PCCs is increased by the carbonization temperature. However, PCC-800 shows lower I_D/I_G ratio than that of PCC-700 because the porous carbon structure is collapsed by the over-activation, which is in correspondence to the BET and BJH data. As a result, the experimental condition for PCC-700 is chosen as the optimal one for the material preparation.

Table 2.1. Structural properties of the PCCs.

Sample	Specific surface area [m^2 g^{-1}]	Mean diameter of pores [nm]	Pore volume [cm^3 g^{-1}]		
			Micro pores	**Meso- and macro-pores**	**Total**
Bare CC	2.53	6.35	0.001	0.008	0.009
PC-20-(700) (powder)	461.61	1.78	0.201	0.231	0.432
PCC-0-(700)	106.47	2.36	0.046	0.086	0.131
PCC-10-(700)	153.56	1.73	0.066	0.076	0.142
PCC-20-(700)	220.84	1.70	0.093	0.106	0.198
PCC-40-(700)	200.52	1.74	0.086	0.099	0.185
PCC-(20)-500	126.97	1.74	0.053	0.055	0.108
PCC-(20)-600	193.69	1.62	0.080	0.078	0.158
PCC-(20)-700	220.84	1.70	0.093	0.106	0.198
PCC-(20)-800	38.23	2.46	0.019	0.024	0.043

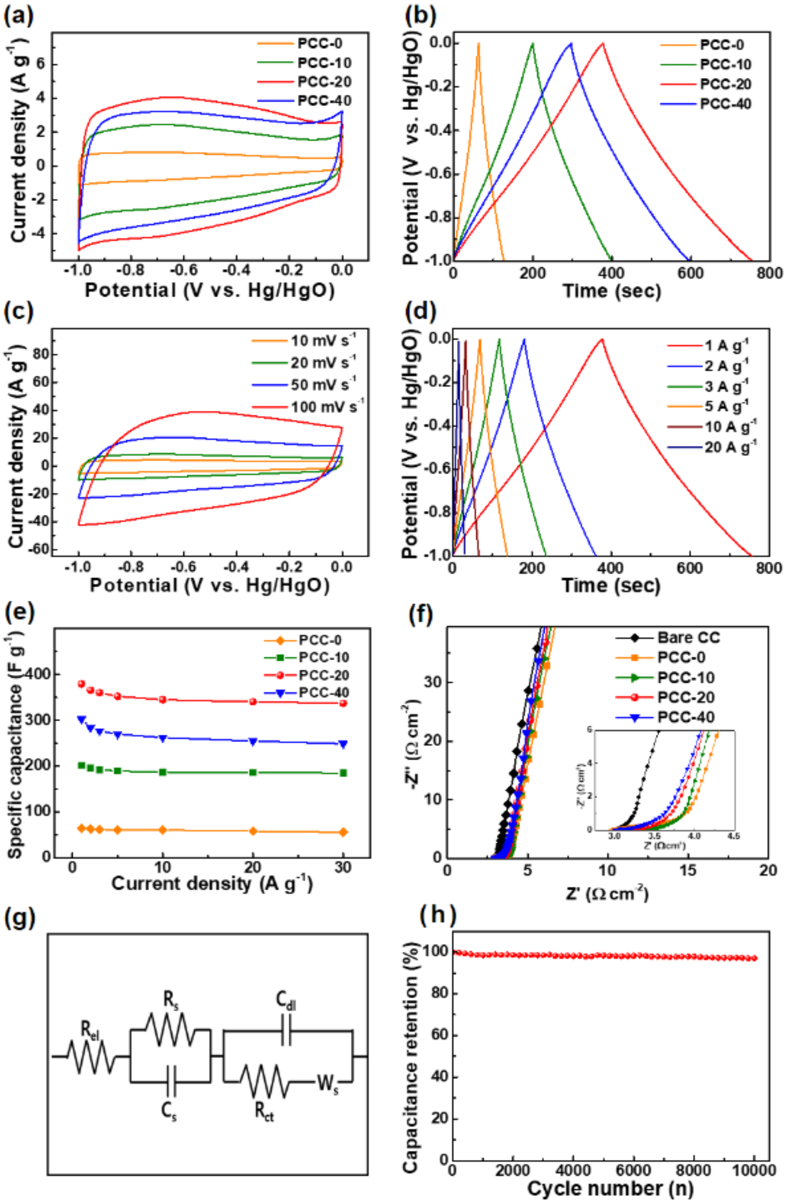

Figure 2.7. Electrochemical performances of PCCs, i.e., PCC-0, PCC-10, PCC-20, and PCC-40, in a three-electrode configuration using 6.0 M KOH electrolyte: (a) CV curves at a scan rate of 10 mV s^{-1}; (b) GCD curves at a fixed current density of 1 A g^{-1}; (c) CV curves of the optimized sample, i.e., PCC-20, at varied scan rates; (d) GCD curves of PCC-20 at various current densities; (e) specific capacitances of PCCs at different current densities from 1 to 30 A g^{-1}; (f) Nyquist plots in a frequency range of 100 kHz - 0.01 Hz (inset: enlargement of the high-frequency region); (g) electrical equivalent circuit used for fitting the impedance spectra; and (h) capacitance retention of PCC-20 upon 10,000 GCD cycles at a current density of 10 A g^{-1}.

Electrochemical performances of the as-prepared PCCs with a different amount of KOH ratio were tested in a three-electrode configuration using Hg/HgO reference electrode, platinum (Pt) mesh as a counter electrode, and a 6.0 M KOH aqueous electrolyte solution. In addition, the measurements were performed within the operation potential window from -1.0 to 0.0 V. To compare the effect of KOH quantities, all the PCCs were carbonized at a temperature of 700 °C and the loading mass was fixed at 1 mg cm^{-2}. The CV curves of PCC-0, PCC-10, PCC-20, and PCC-40 at a scan rate of 10 mV s^{-1} are presented in Figure 2.7a. All CV data exhibits nearly rectangular shape with a slight distortion due to pseudo-capacitance of oxygen atoms in the porous carbon lattice. The CV curve area increases as KOH ratio increases due to a development of hierarchically porous carbon networks by KOH activation. This effect peaked at PCC-20 but started to diminish at PCC-40. The small CV area of PCC-40 indicates that hierarchically porous structures are destroyed by over activation due to an excessive amount of KOH. Galvanostatic charge/discharge (GCD) curves of each samples display highly linear and symmetric triangular shapes implying the capacitive behaviors (see Figure 2.7b). The PCC-20 showed the longest discharging time as expected. Figure 2.7c displays CV curves of PCC-20 with increasing scan rate from 10 to 100 mV s^{-1}. All CV data maintain rectangular shape even at high scan rates, suggesting an electric double layer capacitance (EDLC) behavior and a fast ion diffusion. As shown in Figure 2.7d, GCD curves of PCC-20 at different current densities from 1 to 20 A g^{-1} shows nearly symmetric triangular characteristics indicating good reversibility. The specific capacitance at different current densities for PCC-0, PCC-10, PCC-20, and PCC-40 was compared in Figure 2.7e. At a current density of 1 A g^{-1}, PCC-20 exhibits the highest specific capacitance value of 379.5 F g^{-1}, higher than that of PCC-0 (64.1 F g^{-1}), PCC-10 (201.8 F g^{-1}), and PCC-40 (302.8 F g^{-1}). It is clear that the ratio of KOH greatly affects the formation of porous structure and improvement of specific capacitance. PCC-20 shows an excellent capacitance retention of 89 % (337.6 F g^{-1}) at a current density of 30 A g^{-1}, due to a fast ion accessibility of hierarchically porous structures.

Electrical impedance spectroscopy (EIS) was performed for PCCs to study the electrochemical kinetics, internal and charge transfer resistance. The EIS behavior of the electrodes was tested in the range of 100 kHz – 0.01 Hz in 6M KOH electrolyte. The Nyquist plots and electrical equivalent circuit are presented in Figure 2.7f and g. The values of fitting parameters according to the electrical equivalent circuit are showed in Table 2.2. The R_{el}, R_s, and R_{ct} represent the electrolyte-electrode resistance, surface resistance, and internal charge transfer resistance, respectively. The C_s and C_{dl} represent the surface layer geometrical capacitance and electric-double-layer capacitance, respectively. W_s represents the surface layer diffusion impedance [14-

17]. As shown in Figure 2.7f, the quasi-vertical profile of the PCCs, i.e., PCC-0, PCC-10, PCC-20 and PCC-40, in the low-frequency region indicates efficient diffusion of the electrolyte to the electrode surface. Additionally, when compared to profile of bare CC, the diffusion layer resistance of PCCs in high frequency region is increased because porous carbon is successfully loaded on the surface of carbon fiber. From PCC-0 to PCC-40 as the KOH ratio increases, ionic diffusion layer resistance is decreased. This result indicated that the ionic accessibility is enhanced due to the formation of stable hierarchical structure in the carbon layer [14]. This result is further demonstrated by the fitting parameters as shown in Table 2.2. As the KOH ratio increases, the values of internal and charge transfer resistance (R_{el}, R_s and R_{ct}) are decreased and the values of capacitance (C_s and C_{dl}) are increased. These results imply that the electrolyte ion accessibility improved by increasing the formation of hierarchical pore structures through KOH activation process. Finally, Figure 2.7h shows that the capacitance retention of PCC-20 electrode is 97% upon 10,000 GCD cycles at a current density of 10 A g^{-1}, and there is no evident deterioration in the graph. This result reflects that the electrode has a good electrochemical durability because the porous carbon networks are stably formed and strongly attached on CC surface.

Table 2.2. Fitting parameters for impedance spectra of PCCs, i.e., PCC-0, PCC-10, PCC-20, and PCC-40, according to the electrical equivalent circuit.

	Bare CC	**PCC-0**	**PCC-10**	**PCC-20**	**PCC-40**
R_{el} / Ω cm^2	2.95	3.02	3.03	3.00	3.01
R_s / Ω cm^2	0.64	0.40	0.38	0.27	0.24
C_s / mF cm^2	0.098	0.10	0.12	0.14	0.15
C_{dl} / F cm^2	0.017	0.39	0.61	0.76	0.85
R_{ct} / Ω cm^2	138.50	119.01	107.49	81.02	79.31
W_s / Ω cm^2	1.76×10^{-2}	1.66×10^{-2}	1.44×10^{-2}	1.29×10^{-2}	1.11×10^{-2}

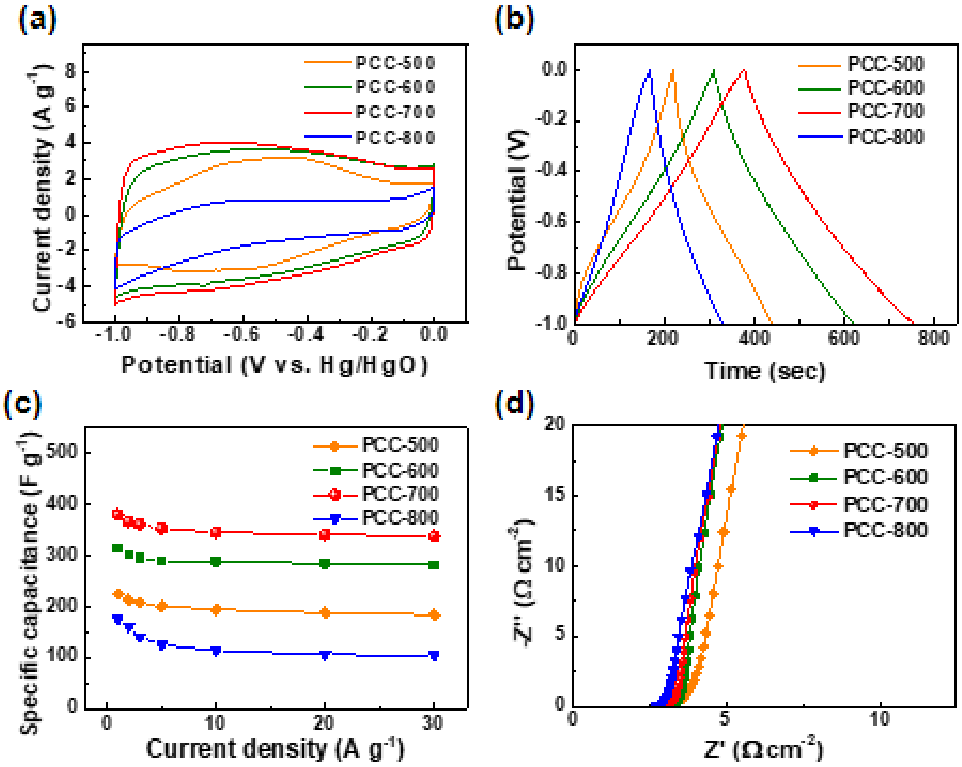

Figure 2.8. Electrochemical performances of PCCs, i.e., PCC-500, PCC-600, PCC-700, and PCC-800, in a three-electrode configuration using 6.0 M KOH electrolyte: (a) CV curves at a scan rate of 10 mV s^{-1}; (b) GCD curves at a current density of 1 A g^{-1}; (c) specific capacitances at different current densities from 1 to 30 A g^{-1}; (d) Nyquist plots in a frequency range of 0.01 Hz - 0.1 MHz.

We investigated the influence of carbonization temperature on the electrochemical performance of PCCs, i.e., PCC-500, PCC-600, PCC-700, and PCC-800, in a three-electrode configuration using 6.0 M KOH electrolyte. Figure 2.8a shows CV curves of PCCs at a scan rate of 10 mV s^{-1}. When the carbonization temperature is increased from 500 °C to 700 °C, areas of each CV curve are increased, and the PCC-700 exhibited the largest integrated CV area. On the other hand, PCC-800 shows the smallest CV area compared to that of other PCCs due to an unstable connection between porous carbon and CC corresponding to FE-SEM images in Figure 2.4. As shown in Figure 2.8b, GCD curves at a current density of 1 A g^{-1} displays a highly linear and symmetrical triangular shapes and the PCC-700 exhibits the longest discharging time compared to that of other samples. Figure 2.8c displays the specific capacitance of PCC-500, PCC-600, PCC-700, and PCC-800 at various current densities from 1 to 30 A g^{-1} implying a strong consensus with the nitrogen adsorption/desorption data as shown in Table 2.1. The PCC-700 exhibited the highest specific capacitance of 379.5 F g^{-1} over PCC-500 (224.4 F g^{-1}), PCC-600 (314.0 F g^{-1}), and PCC-800 (175.3 F g^{-1}) at a low current density of 1 A g^{-1}. For PCC-500, PCC-600, PCC-700, and PCC-800 samples, the 81.9, 89.5, 89.0, and 59.4% of specific capacitances were remained respectively when the current density was increased from 1 to 30 A g^{-1}. Based on the above considerations, it is demonstrated that the PCC-700 possesses optimal electrical and morphological properties for supercapacitor devices. Nyquist plots for the as-prepared PCCs, i.e., PCC-500, PCC-600, PCC-700, and PCC-800, are presented in Figure 2.8d. The values of fitting parameters according to the electrical equivalent circuit are listed in Table 2.3. The quasi-vertical profile of the PCC-20s in low-frequency region indicates that the as-prepared samples have sufficient conductivity. As the carbonization temperature increases, internal and charge transfer resistance (R_{el}, R_s and R_{ct}) are decreased, which means the conductivity and ionic accessibility are improved. The electrochemical characteristics of various previous reported porous carbon materials for supercapacitor application are listed in Table 2.4 for further comparison with this work [18-25].

Table 2.3. Fitting parameters for impedance spectra of PCCs, i.e., PCC-500, PCC-600, PCC-700, and PCC-800, according to the electrical equivalent circuit.

	PCC-500	**PCC-600**	**PCC-700**	**PCC-800**
R_{el} / Ω cm^2	3.12	3.06	3.00	2.28
R_s / Ω cm^2	0.49	0.38	0.27	0.24
C_s / mF cm^2	0.16	0.22	0.32	0.44
C_{dl} / F cm^2	0.48	0.63	0.86	0.89
R_{ct} / Ω cm^2	160.23	113.01	98.02	89.39
W_s / Ω cm^2	1.66×10^{-2}	1.44×10^{-2}	1.39×10^{-2}	1.32×10^{-2}

Table 2.4. Comparison of electrochemical performances with previously reported porous carbon materials in a three-electrode configuration.

Materials	**Specific capacitance / F g^{-1}**	**Rate capability / %**	**Electrolyte**	**Binder**	**Ref.**
PCC-20-700	379 @1 Ag^{-1}	90 (341 F g^{-1}@30 A g^{-1})	6M KOH	none	**This work**
CS-HPGC	332 @0.5 Ag^{-1}	64 (212 F g^{-1}@20 A g^{-1})	6M KOH	PVDF	[18]
NMCNS-1	356 @0.5 Ag^{-1}	67 (239 F g^{-1}@20 A g^{-1})	6M KOH	PTFE	[19]
SPC-5	397 @0.5 Ag^{-1}	70 (278 F g^{-1}@50 A g^{-1})	6M KOH	PTFE	[20]
SC-750	415 @0.5 Ag^{-1}	83 (344 F g^{-1}@10 A g^{-1})	6M KOH	PTFE	[21]
HPNC	312 @1 Ag^{-1}	81 (253 F g^{-1}@10 A g^{-1})	6M KOH	PVDF	[22]
ACA-SCD	261 @1 Ag^{-1}	78 (204 F g^{-1}@20 A g^{-1})	6M KOH	PVDF	[23]
3D C foam	227 @1 Ag^{-1}	50 (114 F g^{-1}@20 A g^{-1})	6M KOH	none	[24]
F-AC-12	272 @1 Ag^{-1}	87 (237 F g^{-1}@20 A g^{-1})	6M KOH	none	[25]

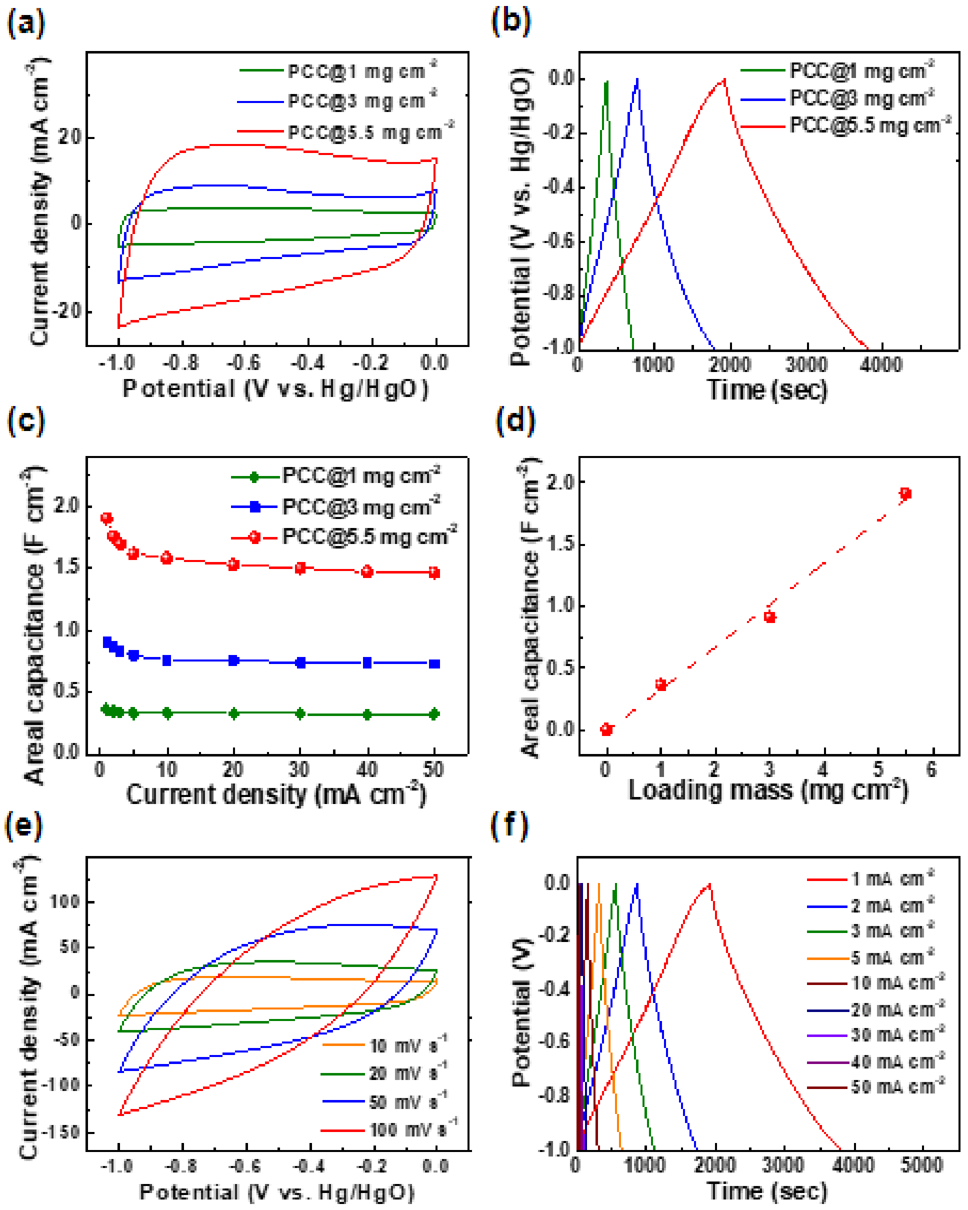

Figure 2.9. Electrochemical performances of PCCs with different loading mass of 1, 3, and 5 mg cm^{-2} in a three-electrode configuration using 6.0 M KOH electrolyte: (a) CV curves at a scan rate of 10 mV s^{-1}; (b) GCD curves at a current density of 1 mA cm^{-2}; (c) areal capacitances at different current densities from 1 to 50 mA cm^{-2}; (d) plots of areal capacitance with different loading mass; (e) CV curves of PCC with loading mass of 5.5 mg cm^{-2} at different scan rates; and (f) GCD curves of PCC with a loading mass of 5.5 mg cm^{-2} at different current densities from 1 to 50 mA cm^{-2}.

To examine the high areal capacity in a high mass loading electrode, the loading mass of PCC-20-700 was increased from 1 to 5.5 mg cm^{-2} (i.e., PCC@1 mg cm^{-2}, PCC@3 mg cm^{-2}, and PCC@5.5 mg cm^{-2}). Figure 2.9a shows CV curves of PCC@1 mg cm^{-2}, PCC@3 mg cm^{-2}, and PCC@5.5 mg cm^{-2} at a fixed scan rate of 10 mV s^{-1}. When the loading mass is increased, the CV curves exhibit larger area. Also, all the CV curves show quasi-rectangular shapes even at high mass loading of 5.5 mg cm^{-2}. The same trend is observed in GCD profiles at current density of 1 mA cm^{-2}, nearly symmetric triangular shapes and small IR drops, suggesting favorable conductivity and high coulombic efficiency (see Figure 2.9b). Figure 2.9c shows the areal capacitance values for different mass loadings at different current densities from 1 to 50 mA cm^{-2}. The areal capacitances of PCCs with a different loading mass measured at a low current density of 1 mA cm^{-2} are 0.36, 0.91, and 1.91 F cm^{-2}, respectively, and the retention ratios of the specific capacitances of each sample at the current density of 50 mA cm^{-2} are evaluated to be 88.8%, 80.7%, and 77.0% for PCC@1 mg cm^{-2}, PCC@3 mg cm^{-2}, and PCC@5.5 mg cm^{-2}, respectively. The PCC@5.5 mg cm^{-2} electrode exhibits the highest areal capacitance value and an excellent rate capability performance with 77% (1.47 F cm^{-2}) of capacitance retention at a current density of 50 mA cm^{-2}, supporting the result that the hierarchically porous carbon structures are beneficial to fast electron transfer even at high mass loaded electrode. When the mass loading is increased from 1.0 to 5.5 mg cm^{-2}, the areal capacitance at a current density of 1 mA cm^{-2} is increased almost linearly as shown in Figure 2.9d. This result reveals that the as-prepared PCCs enable to control a loading mass of porous carbon without losing its capacity performances. Figure 2.9e shows the CV curves of PCC@5.5 mg cm^{-2} corresponding to various scan rates from 10 to 100 mV s^{-1}. A quasi-rectangular CV curve is maintained at a scan rate of 100 mV s^{-1} because optimal structure of sample contributes to a high electrical conductivity and a specific surface area. Moreover, ideal symmetry triangular shapes are maintained in the GCD curves of the sample measured at various current densities ranging from 1 to 50 mA cm^{-2} and a small voltage drop was also remained (see Figure 2.9f). The morphology of PCC@5.5 mg cm^{-2} can be confirmed by FE-SEM images as shown in Figure 2.10 showing a thick porous carbon layer stably covers the CC surface, which is similar to that of PCC@1 mg cm^{-2}.

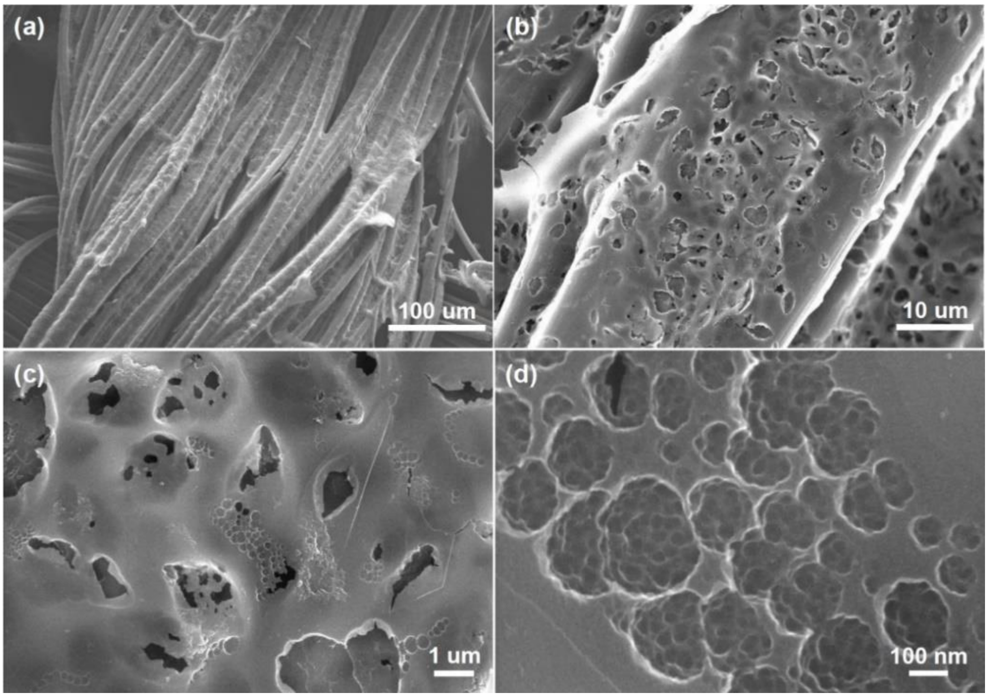

Figure 2.10. (a-d) FE-SEM images of PCC@5.5 mg cm^{-2} with different magnifications.

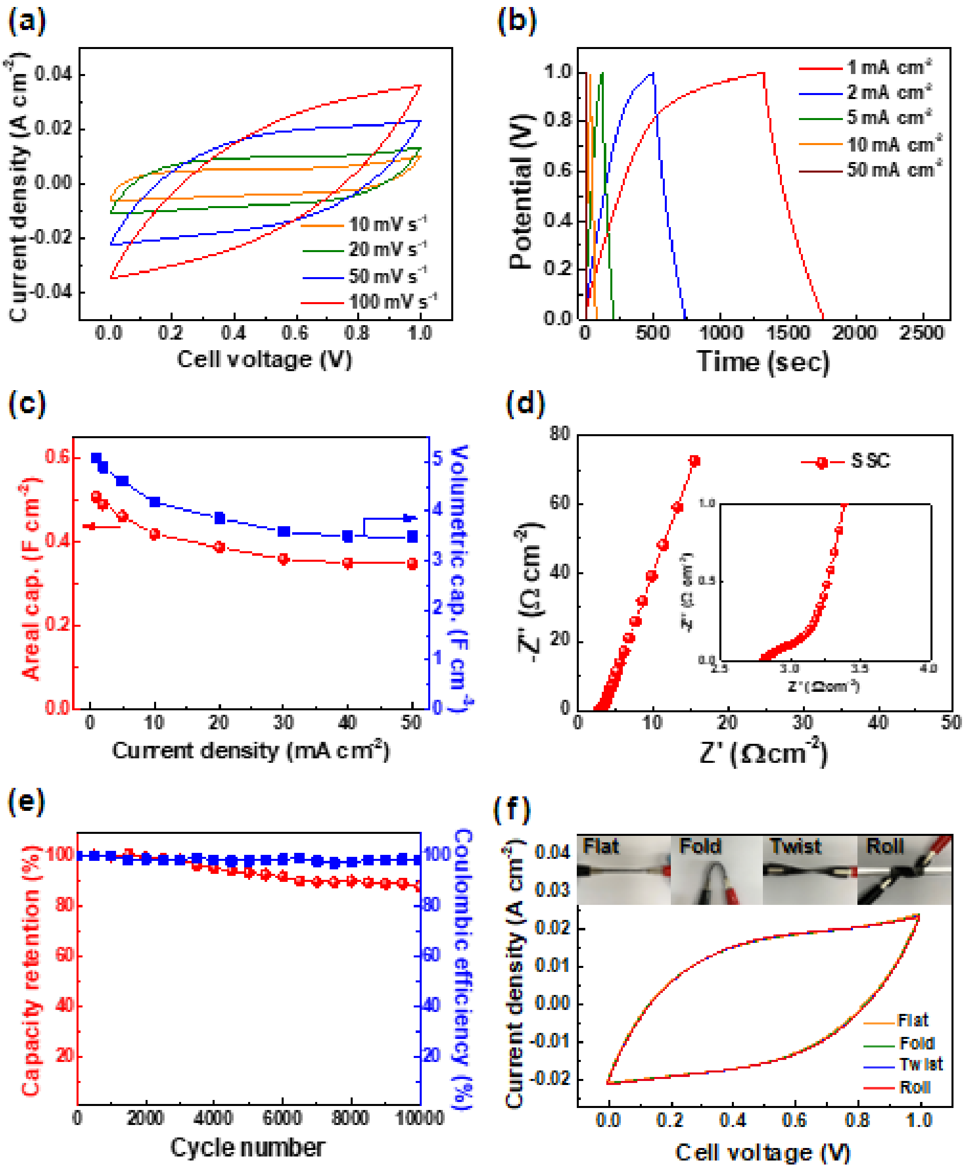

Figure 2.11. Electrochemical performances of symmetrical supercapacitor (SSC) device using the optimized PCCs: (a) CV curves at different scan rates; (b) GCD curves at different current densities; (c) areal and volumetric capacitances at different current densities; (d) Nyquist plots in a frequency range of 100 kHz - 0.01 Hz with the inset showing high-frequency region; (e) capacitance retention and Coulombic efficiency upon 10,000 GCD cycles at a current density of 10 mA cm^{-2}; and (f) CV curves for flexibility test under flat, fold, twist, and roll at a fixed scan rate of 50 mV s^{-1} with the inset showing digital images of each motion.

The electrochemical performance of a symmetrical supercapacitor (SSC) device based on PCC@5.5 mg cm^{-2} with a PVA-KOH electrolyte was summarized in Figure 2.11. The CV curves at various scan rates from 10 to 100 mV s^{-1} display nearly rectangular shapes with a good symmetry and maintain its shapes even at a high scan rate up to 100 mV s^{-1} (see Figure 2.11a). As shown in Figure 2.11b, the GCD curves exhibits quasi-triangular shapes with small IR drops. When increasing the current density from 1 to 50 mA cm^{-2}, 68.6% of its initial capacitance was maintained, indicating a good rate capability of the device. The areal capacitance of the device reached to a value of 507 mF cm^{-2} at a current density of 1 mA cm^{-2}, which are corresponding to a volumetric capacitance (5.07 F cm^{-3}) based on GCD data (see Figure 2.11c). Figure 2.11d shows the Nyquist plot of the SSC device obtained in an open circuit potential in a frequency range from 100 kHz to 0.01 Hz. The values of fitting parameters according to the electrical equivalent circuit are showed in Table 2.5. The quasi-vertical profile of the device in low-frequency region indicates that the device has a nearly ideal supercapacitor behavior. Additionally, the small diameter of the semicircle in high frequency region suggests excellent ionic conductivity between the electrode and electrolyte [14,17]. In contrast, low-frequency Nyquist plot of the device shows a typical Warburg impedance characteristic, where the electrochemical reaction mechanism is dominated by the ion diffusion effects at the electrolyte/electrode interfaces. Moreover, 87.7% of areal capacitance and a 98.0% of coulombic efficiency were maintained upon 10,000 GCD cycles at a current density of 10 mA cm^{-2} implying that the device possesses excellent long-term cycle stability (see Figure 2.11e). As shown in Figure 2.11f, the flexibility test of the all-solid-state SSC device was carried out in a CV measurement at a scan rate of 50 mV s^{-1}. The CV shape of the SSC device at a flat state is well retained even at hard mechanical deformations when the device was folded, twisted, and rolled, indicating favorable electrochemical durability and mechanical integrity.

Table 2.5. Fitting parameters for impedance spectra of SSC device based on PCC@5.5 mg cm^{-2} with a PVA-KOH electrolyte according to the electrical equivalent circuit.

	SSC device
R_{el} / Ω cm^2	3.21
R_s / Ω cm^2	0.81
C_s / mF cm^2	1.45
C_{dl} / F cm^2	1.28
R_{ct} / Ω cm^2	108.23
W_s / Ω cm^2	1.56×10^{-2}

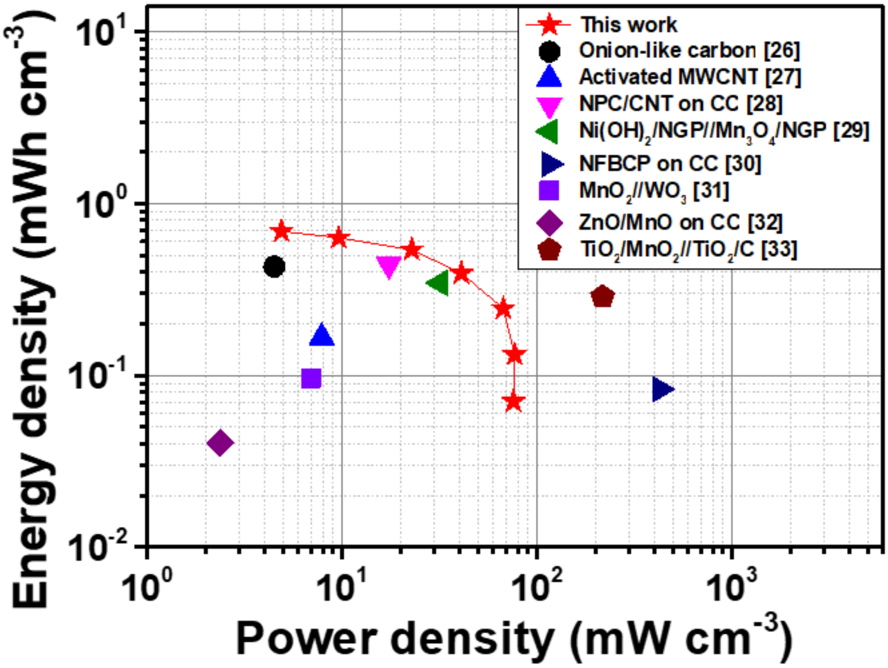

Figure 2.12. Ragone plots of SSC device using PCCs as well as previously referred supercapacitor devices.

Ragone plots of the optimized PCC-based symmetric supercapacitor (SSC) device and previously referred supercapacitor devices using carbon materials are shown in Figure 2.12. The PCC supercapacitor device accomplished a high volumetric energy density of 0.69 mWh cm^{-3} at a power density of 4.91 mW cm^{-3}, and a power density of 77.22 mW cm^{-3} was obtained at an energy density of 0.13 mWh cm^{-3}. These results were comparable to other carbon-based electrodes resulted in previous reports, such as structural carbons [26], activated MWCNTs [27], and doped porous carbons [28-30]. Our results were also higher than those of carbon textile-based symmetric or asymmetric supercapacitor devices composed of composites with metal oxides [31-33].

The PCC electrode had exhibited outstanding electrochemical performances, which evaluated high capacitance and long-cycle stability even with high-rate capability. A preparation of homogeneous CA-KOH gel is very easy and helpful to fabricate the PCC electrode due to its viscosity property with high concentration of carbon source. Moreover, KOH is a good activation agent to modulate the porous carbon structure. These features effectively facilitate a precursor coating on a flexible substrate and a synthesis of hierarchically porous carbon network highly attached on the CC surface, where the coating and modulating effect would be reflected by the electrochemical performance, such as capacitance and rata capability. In order to achieve high rate capability, ion transport should compensate electron transfer in a cell. Therefore, integrating optimal channels for ion diffusion is as essential as the electrical conductivity of the electrode in supercapacitors. For PCC electrodes, carbon cloth with large surface area serves as the flexible substrate offering good conductivity. Controlled KOH activation process is used to generate a high surface area and a good wettability to enhance electrolyte access, which can guarantee a high capacitance and rate capability. The binder-free electrode provides good conductivity even at high current density and maintains ion diffusion channels in the material. As a result, synergistic effects of hierarchically porous carbon networks fabricated by facile and binder-free method contribute to a high electrochemical performance.

2.1.4 Summary

In summary, a low-cost binder-free all-carbon electrode derived from modified potassium citrate was prepared through a simple thermal decomposition and carbonization method. The hierarchically porous carbon structure tuned by KOH and a thermal treatment temperature showed high surface area with unique surface morphology. Furthermore, the free-standing all-carbon electrode exhibited a high specific capacitance with a high-rate capability due to the merits of good electrolyte affinity, improved charge and ion transfer, and appropriate electrical conductivity. Benefiting from its good electrolyte accessibility and fast charge transfer ascribed to its unique multiscale hierarchical pore structure, the resulting PCCs exhibited a high specific capacitance of 379.5 F g^{-1} at a current density of 1 A g^{-1} with high-rate capability and cycle stability in a three-electrode configuration. Furthermore, the SSC device using the optimal PCCs showed a high energy density of 0.69 mWh cm^{-3} with a power density of 4.91 mW cm^{-3}, as well as excellent cycle stability (87.7% retention after 10,000 cycles), and mechanical flexibility. The novel methodology in this study provides valuable candidates in the fabrication of flexible binder-free type porous carbon electrode for a wide range of applications, including high-performance supercapacitors.

2.1.5 References

[1] Y.-J. Gu, W. Wen, J. Wu, Simple air calcination affords commercial carbon cloth with high areal specific capacitance for symmetrical supercapacitors, J. Mater. Chem. A 6 (2018) 21078.

[2] S. Jiang, T. Shi, X. Zhan, H. Long, S. Xi, H. Hu, Z. Tang, High-performance all-solid-state flexible supercapacitors based on two-step activated carbon cloth, J. Power Sources 272 (2014) 16–23.

[3] Z. Dou, Z. Qin, Y. Shen, S. Hu, N. Liu, Y. Zhang, High-performance flexible supercapacitor based on carbon cloth through in-situ electrochemical exfoliation and re-deposition in neutral electrolyte, Carbon 153 (2019) 617–624.

[4] L.-F. Chen, X.-D. Zhang, H.-W. Liang, M. Kong, Q.-F. Guan, P. Chen, Z.-Y. Wu, S.-H. Yu, Synthesis of nitrogen-doped porous carbon nanofibers as an efficient electrode material for supercapacitors, ACS Nano 6 (2012) 7092–7102.

[5] B. Li, F. Dai, Q. Xiao, L. Yang, J. Shen, C. Zhang, M. Cai, Nitrogen-doped activated carbon for a high energy hybrid supercapacitor, Energy Environ. Sci. 9 (2016) 102–106.

[6] M. Sevilla, A.B. Fuertes, Direct synthesis of highly porous interconnected carbon nanosheets and their application as high-performance supercapacitors, ACS Nano 8 (2014) 5069–5078.

[7] Y. Fang, B. Luo, Y. Jia, X. Li, B. Wang, Q. Song, F. Kang, L. Zhi, Renewing functionalized graphene as electrodes for high-performance supercapacitors, Adv. Mater. 24 (2012) 6348–6355.

[8] S. Stankovich, D.A. Dikin, R.D. Piner, K.A. Kohlhaas, A. Kleinhammes, Y. Jia, Y. Wu, S.T. Nguyen, R.S. Ruoff, Synthesis of graphene-based nanosheets via chemical reduction of exfoliated graphite oxide, Carbon 45 (2007) 1558–1565.

[9] A. Sadezky, H. Muckenhuber, H. Grothe, R. Niessner, U. Pöschl, Raman microspectroscopy of soot and related carbonaceous materials: spectral analysis and structural information, Carbon 43 (2005) 1731–1742.

[10] M.M. Lucchese, F. Stavale, E.H.M. Ferreira, C. Vilani, M.V.O. Moutinho, R.B. Capaz, C.A. Achete, A. Jorio, Quantifying ion-induced defects and Raman relaxation length in graphene, Carbon 48 (2010) 1592–1597.

[11] A.C. Ferrari, D.M. Basko, Raman spectroscopy as a versatile tool for studying the properties of graphene, Nat. Nanotechnol. 8 (2013) 235–246.

[12] J. Wang, S. Kaskel, KOH activation of carbon-based materials for energy storage, J. Mater. Chem. 22 (2012) 23710–23725.

[13] Y. Lv, F. Zhang, Y. Dou, Y. Zhai, J. Wang, H. Liu, Y. Xia, B. Tu, D. Zhao, A comprehensive study on KOH activation of ordered mesoporous carbons and their supercapacitor application, J. Mater. Chem. 22 (2012) 93–99.

[14] B.-A. Mei, O. Munteshari, J. Lau, B. Dunn, L. Pilon, Physical interpretations of Nyquist plots for EDLC electrodes and devices, J. Phys. Chem. C 122 (2018) 194–206.

[15] S.P. Lee, G.A.M. Ali, H.H. Hegazy, H.N. Lim, K.F. Chong, Optimizing reduced graphene oxide aerogel for a supercapacitor, Energy Fuels 35 (2021) 4559–4569.

[16] A. Chonat, S. Palatty, Enhanced electrochemical performance of a hybrid supercapacitive material based on ternary doped polyaniline/activated carbon composite, Energy Fuels 34 (2020) 10148–10159.

[17] Y. Liu, Y. Bai, W. Jaegermann, R. Hausbrand, B.-X. Xu, Impedance modeling of solid-state electrolytes: influence of the contacted space charge layer, ACS Appl. Mater. Interfaces 13 (2021) 5895–5906.

[18] Y. Gong, D. Li, Q. Fu, Y. Zhang, C. Pan, Nitrogen self-doped porous carbon for high-performance supercapacitors, ACS Appl. Energy Mater. 3 (2020) 1585–1592.

[19] B. Chang, L. Wang, W. Shi, Y. Chai, S. Zhang, B. Yang, In situ self-activation synthesis of binary-heteroatom co-doped 3D coralline-like microporous carbon nanosheets for high-efficiency energy storage in flexible all-solid-state symmetrical supercapacitors, Sustainable Energy Fuels, 4 (2020) 2527–2540.

[20] Y. Li, S. Liu, Y. Liang, Y. Xiao, H. Dong, M. Zheng, H. Hu, Y. Liu, Bark-based 3D porous carbon nanosheet with ultrahigh surface area for high

performance supercapacitor electrode material, ACS Sustainable Chem. Eng. 7 (2019) 6601–6610.

[21] M. Li, H. Xiao, T. Zhang, Q. Li, Y. Zhao, Activated carbon fiber derived from sisal with large specific surface area for high-performance supercapacitors, ACS Sustainable Chem. Eng. 7 (2019) 4716–4723.

[22] L. Zhang, T. You, T. Zhou, X. Zhou, F. Xu, Interconnected hierarchical porous carbon from lignin-derived byproducts of bioethanol production for ultra-high performance supercapacitors, ACS Appl. Mater. Interfaces. 8 (2016) 13918–13925.

[23] G. Zu, J. Shen, L. Zou, F. Wang, X. Wang, Y. Zhang, X. Yao, Nanocellulose-derived highly porous carbon aerogels for supercapacitors, Carbon. 99 (2016) 203–211.

[24] B. You, J. Jiang, S. Fan, Three-dimensional hierarchically porous all-carbon foams for supercapacitor, ACS Appl. Mater. Interfaces 6 (2014) 15302–15308.

[25] Y. Zhong, T. Shi, Y. Huang, S. Cheng, G. Liao, Z. Tang, One-step synthesis of porous carbon derived from starch for all-carbon binder-free high-rate supercapacitor, Electrochim. Acta. 269 (2018) 676–685.

[26]
D. Pech, M. Brunet, H. Durou, P. Huang, V. Mochalin, Y. Gogotsi, P.-L. Taberna, P. Simon, Ultrahigh-power micrometre-sized supercapacitors based on onion-like carbon, Nat. Nanotechnol. 5 (2010) 651–654.

[27] L. Liu, D. Ye, Y. Yu, L. Liu, Y. Wu, Carbon-based flexible micro-supercapacitor fabrication via mask-free ambient micro-plasma-jet etching, Carbon 111 (2017) 121–127.

[28] D.K. Kim, N.D. Kim, S.-K. Park, K.-D. Seong, M. Hwang, N.-H. You, Y. Piao, Nitrogen doped carbon derived from polyimide/multiwall carbon nanotube composites for high performance flexible all-solid-state supercapacitors, J. Power Sources 380 (2018) 55–63.

[29] Y. Zeng, Y. Han, Y. Zhao, Y. Zeng, M. Yu, Y. Liu, H. Tang, Y. Tong, X. Lu, Advanced Ti-doped Fe_2O_3@PEDOT core/shell anode for high-energy asymmetric supercapacitors, Adv. Energy Mater. 5 (2015) 1402176.

[30] D.K. Kim, S. Bong, X. Jin, K.-D. Seong, M. Hwang, N.D. Kim, N.-H. You, Y. Piao, Facile in situ synthesis of multiple-heteroatom-doped carbons derived from polyimide precursors for flexible all-solid-state supercapacitors, ACS Appl. Mater. Interfaces 11 (2019) 1996–2005.

[31] S.-H. Ji, N.R. Chodankar, W.-S. Jang, D.-H. Kim, High mass loading of h-WO_3 and a-MnO_2 on flexible carbon cloth for high-energy aqueous asymmetric supercapacitor, Electrochim. Acta 299 (2019) 245–252.

[32] P. Yang, X. Xiao, Y. Li, Y. Ding, P. Qiang, X. Tan, W. Mai, Z. Lin, W. Wu, T. Li, H. Jin, P. Liu, J. Zhou, C.P. Wong, Z.L. Wang, Hydrogenated ZnO core−shell nanocables for flexible supercapacitors and self-powered systems, ACS Nano 7 (2013) 2617–2626.

[33] X. Lu, M. Yu, G. Wang, T. Zhai, S. Xie, Y. Ling, Y. Tong, Y. Li, H-TiO_2@MnO_2//H-TiO_2@C core–shell nanowires for high performance and flexible asymmetric supercapacitors, Adv. Mater. 25 (2013) 267–272.

Chapter 2.2 Redox-active conjugated microporous anthraquinonylamine-based polymer network grafted with activated graphene toward high-performance flexible asymmetric supercapacitor electrodes

[Jang et al., Electrochim. Acta 434 (2022) 141315]

2.2.1 Motivation

As mentioned in chapter 1, conjugated microporous polymer networks have attracted tremendous attention as suitable candidates for supercapacitor electrode materials owing to the tunable porosity and molecular structure with a large specific surface area and a redox reactivity, and strong covalent bonding with abundant unsaturated π-bond nature afford a high stability and a charge conductivity [1-4]. Unique porosity and microstructure with a large surface area of CMP-based electrodes endow EDLC contribution with fast scan-rate performance, while the numerous redox-active sites of the CMP backbones consisting of heteroatom functional groups offer outstanding pseudo energy storage performance [5,6]. Despite these advantages, the intrinsically low electronic conductivity of the CMP-based electrodes hampers their wide usage in energy storage because it could limit their capacitive performance and cycling stability [7-10]. Therefore, recent studies have introduced conductive support to the organic molecules to improve electrical conductivity by using carbonaceous materials such as graphene [11-15].

As the conductive support, graphene not only has excellent electrical conductivity, but also has strong durability against mechanical/chemical stress, and provides a stable framework for polymer growth, helping to synthesize a hybrid in which the two materials are uniformly incorporated [16,17]. Also, through the hybrid synthesis of graphene and polymer, it is possible to secure and preserve a substantial surface area for the pseudo-capacitive reaction by preventing re-aggregation of each material [18-20]. In addition, it has been widely accepted that the preparation method of activated graphene, which is in-plane generation of defects in graphene sheets, can not only significantly improves the reactive surface area, but also prevent re-stacking and provide an effective electrolyte path to achieve the enhanced ionic conductivity [21-24]. The introduction of defects in graphene sheets is accompanied by breakage due to the generation and growth of pores, which directly affects the EC performance of the graphene/CMP hybrid electrode [25-28]. Therefore, it is crucial to control the activation conditions of graphene for the development of graphene/CMP hybrids for high-performance supercapacitor electrodes.

Herein, we have synthesized conjugated microporous anthraquinonyl-amine-based polymer network grafted with highly activated graphene (CMAP@AG) via facile one-step BH coupling reaction as active materials for supercapacitor application. The CMAP contains secondary amine bonds between 2,6-diaminoanthraquinone (DAQ) and tris(4-bromophenyl) amine (TA). Compared to using mono-component polymers, the CMAP network takes advantage of 3D macromolecular porous networks with efficient electron and ion transportation. Furthermore, the AG was employed as effective conductive support with in-plane pores. The AGs could enhance the possible specific surface area and mass transfer during EC reactions. In this work, the AG fabrication was controlled by varying acid reflux activation times from 0 to 8 hours. With varied acid treatment times, the resulting AG shows different structural properties regarding porosity, surface area, and flake sizes. In contrast to pristine graphene, these porous AG sheets efficiently intercalated into a CMAP network to build a pillared 3D porous structure. More importantly, their properties also influence the resulting CMAP@AG structure and EC performance owing to the synergistic effect of both AG and CMAP. A series of CMAP@AG hybrid electrodes were prepared and investigated for exceptional enhancement of EC performance such as specific capacitance, long-term cycle stability, and flexibility.

2.2.2 Experiment

2.2.2.1 Materials

Graphite powder (< 20 microns, Sigma-Aldrich), sulfuric acid (H_2SO_4, 97 %, Samchun), potassium persulfate ($K_2S_2O_8$, 98 %, Samchun), phosphorus pentoxide (P_2O_5, 97 %, Sigma-Aldrich), potassium permanganate ($KMnO_4$, > 99 %, Sigma-Aldrich), hydrogen peroxide (H_2O_2, 30.0–35.5 %, Samchun), hydrochloric acid (HCl, 35.0–37.0 %, Samchun), N-methyl-2-pyrrolidone (NMP, > 99.8 %, Samchun), 2,6-diaminoanthraquinone (DAQ, > 99 %, Sigma-Aldrich), tris(4-bromo-phenyl) amine (TA, > 99 %, Alfa Aesar), bis(dibenzylideneacetone) palladium (0) ($Pd(dba)_2$, Alfa Aesar), sodium tert-butoxide (NaOtBu, 98 %, Alfa Aesar), 2-dicyclohexylphosphino-2’,4’,6’-triisopropyl-biphenyl (XPhos, 98 %, Alfa Aesar), anhydrous toluene (99.8 %, Alfa Aesar), N,N-dimethylformamide (DMF, 99.5 %, Samchun), chloroform ($CHCl_3$, 99.5 %, Sigma-Aldrich), and poly(vinyl alcohol) (PVA, Mw. 89k–98k, > 99 % hydrolyzed, Sigma-Aldrich) with A.R. grades were used as received without purification. Deionized (DI) water used in this work was obtained by using a Milli-Q ultrapure water system (Millipore, USA).

2.2.2.2 Preparation of activated graphene (AXGs, X=0, 1, 4, and 8 hours)

Graphene oxide (GO) was synthesized via a modified hummer's method following the previously reported procedures [28]. Briefly, graphite (3.0 g) was firstly added to a mixture of concentrated H_2SO_4 (60 mL, 95 %), $K_2S_2O_8$ (2.5 g), and P_2O_5 (2.5 g) in a 250 mL beaker and then heated for 4 hours with a vigorous stirring. The resultant mixture was cooled to room temperature. Next, DI water (400 mL) was slowly added to the mixture under constant stirring in an ice-water bath to prevent subsequent temperature increases. After the addition of DI water, the mixture was washed with DI water by filtration several times until neutralized. Then, the remaining pre-oxidized graphite was dried thoroughly using a convection oven at a temperature of 60 °C for 10 hours. Concentrated H_2SO_4 (60 mL, 95 %) was added to the dried pre-oxidized graphite and stirred at room temperature. With using the ice-water bath, K_2MnO_4 (15 g) was carefully added to the mixture to keep the reaction temperature below 20 °C. The mixture was cooled to 0 °C using an ice bath with constant stirring. The dark greenish resultant was heated to 80 °C for 4 hours with stirring. Additional water (300 mL) was slowly added to a mixture in the ice bath. After stirring, H_2O_2 (20 mL) was added to terminate further chemical reactions. Finally, the bright yellow mixture was purified following multiple washing steps with DI water via centrifugation until the pH of a supernatant became neutral, and the final product was freeze-dried for 2 days. The activated graphene oxide (AXG, the 'X' denotes acid treatment time) was synthesized via a wet-chemical etching method combined with ultrasonic vibration and mild acid oxidation [28]. The as-prepared graphene oxide powder (0.35 g) was dispersed in 350 mL of 8 M nitric acid (HNO_3) solution via ultra-sonication for 30 minutes. Next, the mixture was poured into 500 mL of a round bottom flask (RBF). Under vigorous stirring, the mixture was heated and refluxed at 100 °C for different times of 0, 1, 4, and 8 hours for AXG samples, which are denoted A0G, A1G, A4G, and A8G, respectively. Note that GO without additional acid treatment (0 hours) was designated A0G. After heating, the reactor was cooled to room temperature and the resultant AXG was washed several times with DI water until it became neutral, and then lyophilized for 2 days. To perform material characterization, AXG samples were thermally reduced and labeled as rAXGs, i.e., rA0G, rA1G, rA4G, and rA8G, respectively. 0.1 g of each AXG sample was transferred to Swagelok in an argon (Ar) atmosphere using a glove box. Then, the AXG sample was thermally treated under Ar atmosphere at 700 °C for 2 hours. At this time, the temperature was raised at a rate of 5 °C min^{-1}, and a purging step was conducted for 1 hour. Finally, the rAXG sample was obtained after cooling the tube furnace to room temperature.

2.2.2.3 Preparation of CMAP and CMAP@AXG Hybrids

CMAP and CMAP@AG hybrids were synthesized using the Buchwald-Hartwig (BH) coupling method [4]. First, DAQ (0.75 mmol), TA (0.5

mmol), Pd(dba)$_2$ (0.03 mmol), XPhos (0.045 mmol), and NaOtBu (2 mmol) were charged in a 100 mL three-necked RBF and degassed for 30 minutes using nitrogen (N_2) gas. Then, 50 mL of anhydrous toluene was added, and the temperature of the reactor was slowly elevated to 110 °C with vigorous stirring under N_2 atmosphere. The reaction proceeded for 24 hours, and the reactor was cooled down to room temperature. The resulting product was purified by centrifugation (8,000 RCF, 30 min) and washed with 200 mL of DMF, hot DI water, and $CHCl_3$ for 3 times, respectively, and dried in a vacuum oven at 80 °C for 72 hours to yield CMAP. For CMAP@AXG hybrids synthesis, 50 mL of AXG dispersion with different concentrations (in anhydrous toluene) was used instead of pure anhydrous toluene, and other synthetic procedures and conditions were the same. To optimize the amount of graphene added in CMAP@AXG hybrid synthesis, CMAP@A0G-conc. was prepared using A0G dispersions with different concentrations of 0.1, 0.2, 0.5, and 1.0 % (w/v), and the samples were named CMAP@A0G-0.1, CMAP@A0G-0.2, CMAP@A0G-0.5, and CMAP@A0G-1.0, respectively. The CMAP@A0G-0.5 condition was adopted for the further synthesis of CMAP@AXG hybrids because of optimized characterization. In addition, to compare the properties of wet-chemically reduced graphene oxide (via BH coupling) and thermally reduced graphene oxide (via heat treatment, T-rGO), the as-prepared A0G (=GO, 100 mg) was reacted in the same condition of BH coupling without polymer precursors (i.e., DAQ and TA), which was named C-rGO.

2.2.2.4 Material characterization

The morphologies of samples were monitored by field-emission scanning electron microscopy (FE-SEM, S-4800, Hitachi) at 15 kV and high-resolution transmission electron microscopy (HR-TEM, JEM-2100F, JEOL) at 200 kV with an energy-dispersive X-ray (EDX) spectrum. N_2 adsorption/desorption test with an increased gas pressure up to 1.0 bar at 77 K was conducted for Brunauer-Emmett-Teller (BET) and Barrett-Joyner-Halenda (BJH) analysis using a BELSORP-mini II analyzer (MicrotracBEL). The size distribution and zeta potential were measured by dynamic light scattering (DLS) via Zetasizer Nano ZS (Malvern instruments). Raman spectra were obtained by DXR2xi Raman Imaging Microscope (Thermo Fisher Scientific) with an excitation wavelength of 532 nm. The content of palladium in the as-prepared sample was analyzed using an Agilent 7900 inductively coupled plasma-mass spectrometer (ICP-MS). Fourier transform infrared (FT-IR) spectra were taken on a Nicolet iS50 (Thermo Fisher Scientific). Solid-state ^{13}C cross-polarization magic angle spinning nuclear magnetic resonance (CP/MAS NMR) spectra were obtained on an ADVANCE 400 spectrometer. Thermogravimetric analysis (TGA) was performed by using a thermogravimeter (TGA/DSC 1, Mettler Toledo) to define reaction behaviors of materials in the temperature range of 25 ~ 900 °C with a heating rate of 5 °C min^{-1}. Surface elemental analysis was conducted by X-ray photoelectron spectroscopy (XPS) using ESCA spectrometer (SIGMA PROBE, Thermo Fisher Scientific) via a monochromatic Al Kα radiation source. X-ray diffraction (XRD) patterns were obtained on a Bruker D8 Advance diffractometer (40 kV, 40 mA) using Cu Kα radiation (2θ = 3 ~ 90°). The sheet resistance of slurry mixture-coated slide glass was measured using a CMT-100s manual contact system with a four-point probe technique with an electrode separation of 1 mm. To prevent the influence of the current collector (graphite foil), slurry mixtures of bare CMAP, CMAP@A0G, CMAP@A1G, CMAP@A4G, and CMAP@A8G were prepared in the same manner as the electrode was applied onto the slide glass.

2.2.2.5 Electrochemical characterization

A slurry was prepared by dispersing a mixture of the synthesized active material, carbon black (Timcal, Super P C60), and polyvinylidene difluoride (PVDF, Solvay, Solef® 6020) in NMP in a mass ratio of 8:1:1, coated on graphite foil (Sigma-Aldrich, 0.1 mm in thickness), and dried at 120 °C overnight in a vacuum oven. The loading mass of the sample was fixed at about 1 mg cm^{-2}, and the as-prepared working electrode exhibited flexibility while the active material film was uniformly coated.

A three-electrode configuration was adopted to measure the electrochemical (EC) performances of individual electrodes in 1.0 M H_2SO_4 aqueous solution, using a sample, a Platinum (Pt) mesh, and an Ag/AgCl electrode as the working electrode (WE), the counter electrode (CE), and the reference electrode (RE), respectively.

The asymmetric and symmetric supercapacitor (ASC and SSC) devices assembled by separating two electrodes with filter paper was tested in a two-electrode system in presence of 1.0 M H_2SO_4/PVA quasi-solid-state electrolyte. For ASC device fabrication, the optimized sample, CMAP@A4G hybrid, was used as the positive electrode and A4G was used as the negative electrode, respectively. The loading mass of the positive electrode was fixed at 1–1.2 mg cm^{-2}, and to balance the charge storage capacity of the positive and negative electrodes, the loading mass of the negative electrode, A4G, was prepared as 1.5–1.8 mg cm^{-2} and used in the ASC device. Meanwhile, the SSC device was assembled using CMAP@A4G hybrid as both negative and positive electrodes. The 1.0 M H_2SO_4/ PVA quasi-solid-state electrolyte was prepared by mixing 3 g of PVA, 30 mL of DI water, and 10 mL of 1.0 M H_2SO_4 aqueous solution at 95 °C for 1 hour with vigorous stirring. Two electrodes and a filter paper (as a separator) were immersed in the electrolyte solution, sandwiched together, and dried in a fume hood at room temperature for 5 hours to evaporate the excess water.

Both cyclic voltammetry (CV) and galvanostatic charge/discharge (GCD) measurements were carried out by using an electrochemical workstation (CHI660E, CH Instruments Inc., USA), and electrical impedance spectroscopy (EIS) was employed to clarify the resistance information by applying an AC voltage with an amplitude of 10 mV and a DC open-circuit voltage (OCV) in the frequency range from 10 mHz to 10 kHz using a ZIVE SP1 (ZIVE Lab.). ZMAN software (ZIVE Lab.) was used to acquire and fit Nyquist plot data. The specific capacitance for each sample was evaluated based on the measured CV curves at various scan rates according to the following equation: (1) $C_s = (\int \cdot I \cdot dV)/(2 \cdot \Delta V \cdot \nu \cdot m)$ where C_s (F g^{-1}), I (A), ΔV (V), ν (V s^{-1}), and m (g) represent the specific capacitance, current, potential window, scan rate, and mass of active material, respectively. The specific capacitance from GCD measurement was calculated through the following equation: (2) $C_s = (I \cdot \Delta t)/(m \cdot \Delta V)$ where C_s (F g^{-1}), I (A), Δt (s), m (g), and ΔV (V) represent the specific capacitance, discharge current, discharge time, the mass of active material in working electrode, and discharging potential range, respectively. To calculate the energy density and power density of a full-cell supercapacitor, the following equations were used: (3) $E = (0.5/3600) \cdot C_s \cdot \Delta V^2$ and (4) $P = 3600 \cdot E \cdot \Delta t^{-1}$, respectively, where E (Wh kg^{-1}), C_s (F g^{-1}), ΔV (V), P (W kg^{-1}), and Δt (s) indicate the energy density, specific capacitance, discharging potential range, power density, and discharging time, respectively. Note that the current collector, i.e., pristine graphite foil without active material, exhibited negligible capacitance (< 20 F g^{-1} at 1 A g^{-1}).

The mass ratio of positive (CMAP@A4G) and negative (A4G) electrode materials in the ASC device were calculated based on the following equation: (5) $M_+/M_- = (C_-\Delta E_-)/(C_+\ \Delta E_+)$ where M_{+-} (g), C_{+-} (F g^{-1}), and ΔE_{+-} (V) represent the mass, specific capacitance, and operation potential window, respectively, tested by the three-electrode configuration. The specific capacitances of whole ASC and SSC devices in a two-electrode configuration were evaluated by the following equation: (6) $C_{asy.\ or\ sy.} = I\cdot\Delta t/(M_T\cdot\Delta V)$ where $C_{asy.\ or\ sy.}$ and M_T are the specific capacitance measured in an asymmetric or symmetric two-electrode configuration and the total mass of active materials in positive and negative electrodes, respectively (i.e., $M_T=M_++M_-$).

The theoretical capacitance value of CMAP (864 F g^{-1}) was determined based on the following calculation when the molecular weight of the repeating unit was substituted with 557 g mol^{-1} and the electron transfer number (n) in the repeating moiety was set to five: (7) Capacitance = $n\cdot F/(Mw\cdot 3.6) = (5\cdot 96485)/(557\cdot 3.6) = 240$ mA h g^{-1}, where n, F (C mol^{-1}), and Mw (g mol^{-1}) indicate the electron transfer number, Faraday constant, and molar weight, respectively. The resulting value was converted to: (240 mA h g^{-1})·(3600s/h)·(A/1000 mA) = 864 A s g^{-1}. Finally, the potential window (1.0 V) was considered as: (864 A s g^{-1})/(1.0 V) = 864 F g^{-1}.

2.2.3 Results and discussion

The synthesis route of conjugated microporous anthraquinonylamine-based polymer network grafted with highly activated porous graphene (CMAP@AXG) and TEM images of CMAP@A4G, the optimized sample, are shown in Figure 2.13. The overall synthesis of CMAP@AXG introduced into (1) preparing activated graphene (AG) oxide through different acid treatment times that can be uniformly dispersed in anhydrous toluene, and (2) conducting BH coupling reaction with polymer precursors. First, graphene oxide (GO) was prepared via a modified hummer's method using concentrated sulfuric acid (H_2SO_4) as an oxidizing medium for chemical exfoliation of graphite as shown in Figure 2.13b. This method is well-known for a large amount of GO production with non-toxic gas compared to using nitric acid (HNO_3). Sequentially, the chemical etching method was adopted for the facile AG synthesis followed by the previously reported procedure [26-28]. This method is a liquid-phase oxidation approach having a lot of advantages, such as cost-effective generation of uniformly distributed in-plane defects (or porosity) on graphene surface and large-scale production of homogeneous AG dispersion. The as-prepared GO was dispersed and refluxed in 8 M HNO_3 solution affording partial detachments of carbon atoms from GO planes by infiltrating HNO_3 molecules through defective edges, i.e., unsaturated carbon atoms. According to this mechanism, nano-sized cavities are created in the GO sheets, which become larger with increasing acid-treatment time, causing the graphene sheets to tear into smaller pieces. Depending on the acid treatment time, i.e., 0, 1, 4, and 8 hours, the as-prepared AGs were named AXGs, i.e., A0G, A1G, A4G, and A8G, respectively, and their structural properties were investigated. Figure 2.14a-d show TEM images of AXG samples indicating that the flake size of graphene sheets clearly decreases with increasing acid treatment time. In detail, there may not be a clear difference between A0G and A1G. This is because nano-sized pores were created on the plane of the A1G. On the other hand, A4G and A8G clearly show broken graphene pieces, and the fragment size becomes smaller as the acid treatment time increases. To investigate the size distribution of AXGs, dynamic light scattering (DLS) measurement was conducted. Figure 2.14e exhibits histograms of hydrodynamic diameter (D_h) distributions with Z-average sizes of A0G, A1G, A4G, and A8G, which are measured as 5083, 5049, 1452, and 585 nm, respectively. This result correlates with the speculation from TEM images that the size of graphene fragments was reduced with the increasing time of acid treatment. To further examine the specific surface area and pore size of AXG samples, nitrogen (N_2) adsorption/desorption isotherm measurement was performed, followed by thermal reduction of AXG samples, denoted rAXGs, i.e., rA0G, rA1G, rA4G, and rA8G, respectively. As shown in Figure 2.14f, Braunauer-Emmette-Teller (BET) surface areas of rA0G, rA1G, rA4G, and rA8G are obtained to be 259, 558, 427, and 563 m^2 g^{-1}, respectively. The acid treatment up to 1 hour could increase specific surface area by generating nano-sized defects on the graphene plane. We consider that prolonged acid treatment time more than 4 hours leads to the enlargement of pores, thus breaking the graphene sheet. The breakage of graphene could result in a surface area decrease. Interestingly, the rA8G sample, however, showed the highest surface area among other samples. After the graphene sheets are torn into pieces, additional nanopore formation and breakage of graphene sheets could occur, resulting in defective edge sites with increased surface area [21-23]. This is explained by the result that the zeta-potential of AXG decreases (becomes negative) with increasing acid treatment time of graphene as shown in Figure 2.14i and Table 2.7. Overall, absolute value trends of zeta potential are in line with the acid treatment time. Comparable zeta potentials between A1G and A4G indicate the existence of a larger number of nanopores on graphene sheets in the A1G sample. A8G shows the smallest negative value of zeta potential, thus proving a larger amount of negatively charged functional groups such as hydroxyl and carboxylic groups on its pore and broken graphene edge sites. As conducting Barrett-Joyner-Halenda (BJH) analysis, pore size distribution was identified from the isotherm curves in Figure 2.14g. Among rAXG samples, the isotherm curve of rA0G is quite different compared to that of rA1G, rA4G, and rA8G. This could be due to the absence of defects on the rA0G surface [24,28]. The pore volume increase in the larger pore size range could be attributed to the internal voids between graphene sheets. On the other hand, the rA1G, rA4G, and rA8G exhibit comparable trends and slightly increased pore volumes in a range of small pores such as micro- and meso-sized ones, indicating the existence of structural defects. The pore size distribution is well-matched with the trend of surface area. Additionally, the BJH pore volume data in Figure 2.14h display that rA1G, rA4G, and rA8G have dominant portions of small-sized micro- and mesopores compared to that of rA0G. With increasing acid treatment time, the rA4G and rA8G exhibit a slightly lower portion of mesopores owing to enlarged pores. BJH pore volume ratio (%) shows a volcano trend with the highest pore volume value achieved for rA1G, which could be due to nanopores on rA1G. Unexpectedly, rA8G shows a lower pore volume ratio than rA1G and rA4G. We anticipate that this might be due to a severe breakage of graphene sheets and its dense re-stacking. Details of the previously mentioned BET surface area and BJH pore volume data are summarized in Table 2.6. At the end of the AXG analysis, Figure 2.14j exhibits Raman spectra of rAXGs with I_D/I_G ratios, respectively. In detail, the intensity ratios at characteristic Raman bands, approximately at 1350 cm^{-1} and 1580 cm^{-1} for the D and G bands, respectively, are evaluated as 1.043, 1.016, 0.985, and 1.094 for rA0G, rA1G, rA4G, and rA8G, respectively. As can be seen, the I_D/I_G ratios are decreased during prolonged acid treatment times up to 4 hours, which is consistent with results obtained in previous research [29]. Compared to the rA0G sample, the decreased I_D/I_G values of rA1G and rA4G imply the removal of quasi-amorphous sp^2-bonded carbon along with acid treatment. However, the I_D/I_G ratio of rA8G is not consistent with these results for rA0G, rA1G, and rA4G. Interestingly, the rA8G shows the highest I_D/I_G ratio among samples, which could be due to an additional introduction of in-plane vacancies after the breakage of graphene sheets.

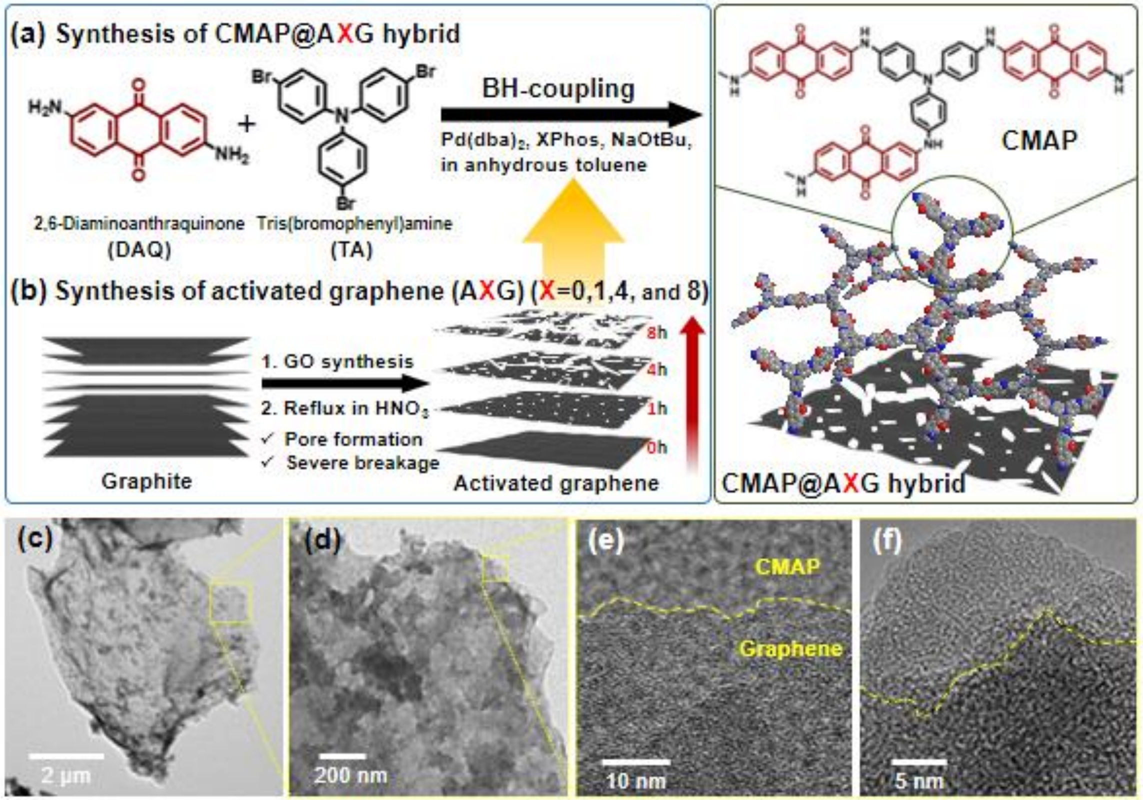

Figure 2.13. Schematic illustration of (a) AXG and (b) CMAP@AXG hybrids synthesis where 'X' stands for acid treatment time, i.e., 0, 1, 4, and 8 h, respectively, and (c-f) TEM images with different magnification of CMAP@A4G hybrid.

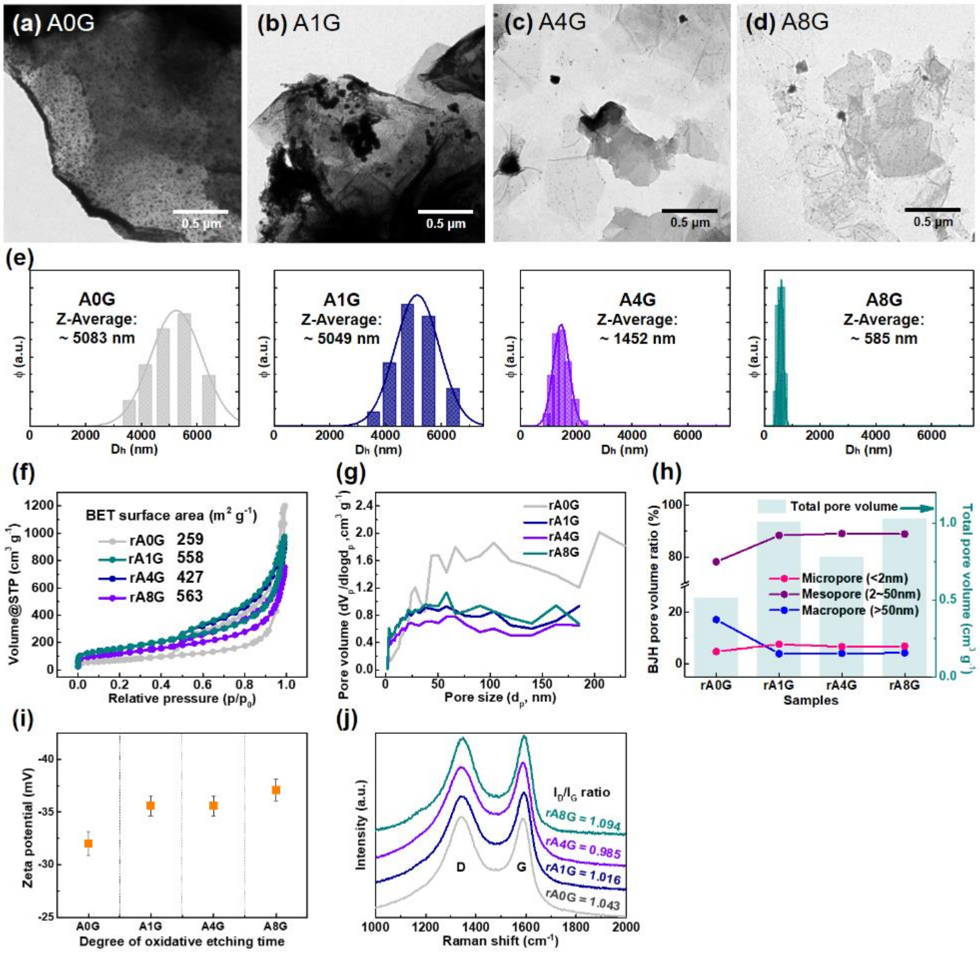

Figure 2.14. (a-d) TEM images and (e) DLS histograms of hydrodynamic diameter (D_h) distributions with Z-average size of AXGs, i.e., A0G, A1G, A4G, and A8G, respectively, (f) N_2 adsorption/desorption isotherms with BET surface areas, (g) pore size distributions, and (h) BJH pore volumes of rAXGs, i.e., rA0G, rA1G, rA4G, and rA8G, respectively, (i) zeta potential of AXGs, and (j) Raman spectra of rAXGs.

Meanwhile, to synthesize CMAP and CMAP@AXG hybrids, the BH coupling method was employed as shown in Figure 2.13a. The BH coupling is an organic synthesis method that induces a polar C–N covalent bond through amination of aryl bromide accompanied by a palladium catalyst [20]. This method expands the scope of aromatic amine synthesis and applications, providing an efficient route to redox-active (i.e., nitrogen-containing) systems that have been found to be exclusively suitable for superior electrochemical energy storage. Through BH coupling of 2, 6-diaminoanthraquinone (DAQ) and tris(bromophenyl) amine (TA), an insoluble dark brown hybrid CMAP network powder was synthesized in high yield (more than 92 wt.%) as shown in Figure 2.15a. The field-emission scanning electron microscopy (FE-SEM) image in Figure 2.15b reveals coral-like CMAP nanoparticles with a size distribution of 50–100 nm, which can contribute outer surface area through external macro- and mesopores. Furthermore, TEM images with the corresponding EDX mapping method in Figure 2.15c show the presence of carbon, nitrogen, and oxygen elements distributed uniformly. Also, Figure 2.15d and e exhibit TEM images at different magnifications showing hierarchical porosity with various diameters, similar to the FE-SEM image. Figure 2.15f displays a high-resolution (HR) TEM image and a selected area electron diffraction (SAED) pattern image indicating the microporous structure and amorphous characteristics of the CMAP network, respectively. Inductively coupled plasma-mass spectroscopy (ICP-MS) confirmed that there was almost no (only 0.01–0.02 mol.%) palladium residue in the final product undergone a harsh refining process. To confirm the D_h distribution, the CMAP was homogeneously dispersed in DI water and then a DLS measurement was conducted. As shown in Figure 2.15g, the as-prepared CMAP exhibits a characteristic small D_h value of around 63 nm which is a Z-averaged Stokes diameter including an electric double-layer thickness. The chemical structure of the CMAP was analyzed by Fourier transform-infrared (FT-IR) and solid-state ^{13}C cross-polarization magic angle spinning nuclear magnetic resonance (CP/MAS NMR). Figure 2.15h shows FT-IR spectra of DAQ, TA, and CMAP. As CMAP was synthesized, peaks by primary amine groups of DAQ, i.e., 3422, 3330 (stretching of $–NH_2$), and 1626 cm^{-1} (deformation of $–NH_2$), and peaks by aryl bromide group of TA, i.e., 1179 and 1005 cm^{-1} (stretching of aryl C–Br) were conspicuously diminished or absent [30]. Also, in the CMAP spectrum, peaks at ≈825 cm^{-1} (for C–H bands) and ≈1300 cm^{-1} (for C–N bands), as well as ≈1498, ≈1585, and ≈1666 cm^{-1} (for C–OH and C=O bands derived from benzenoids and quinoids) became prominent compared to the peaks in the DAQ and TA spectra [31]. Figure 2.15i exhibits a ^{13}C CP/MAS NMR spectrum of CMAP, and there are four main resonance peaks at ≈126, ≈140, ≈157, and ≈185 ppm assigned to C≈C, C≈N, and C=O bonds originating from aryl carbons, amines, and quinones, respectively [32].

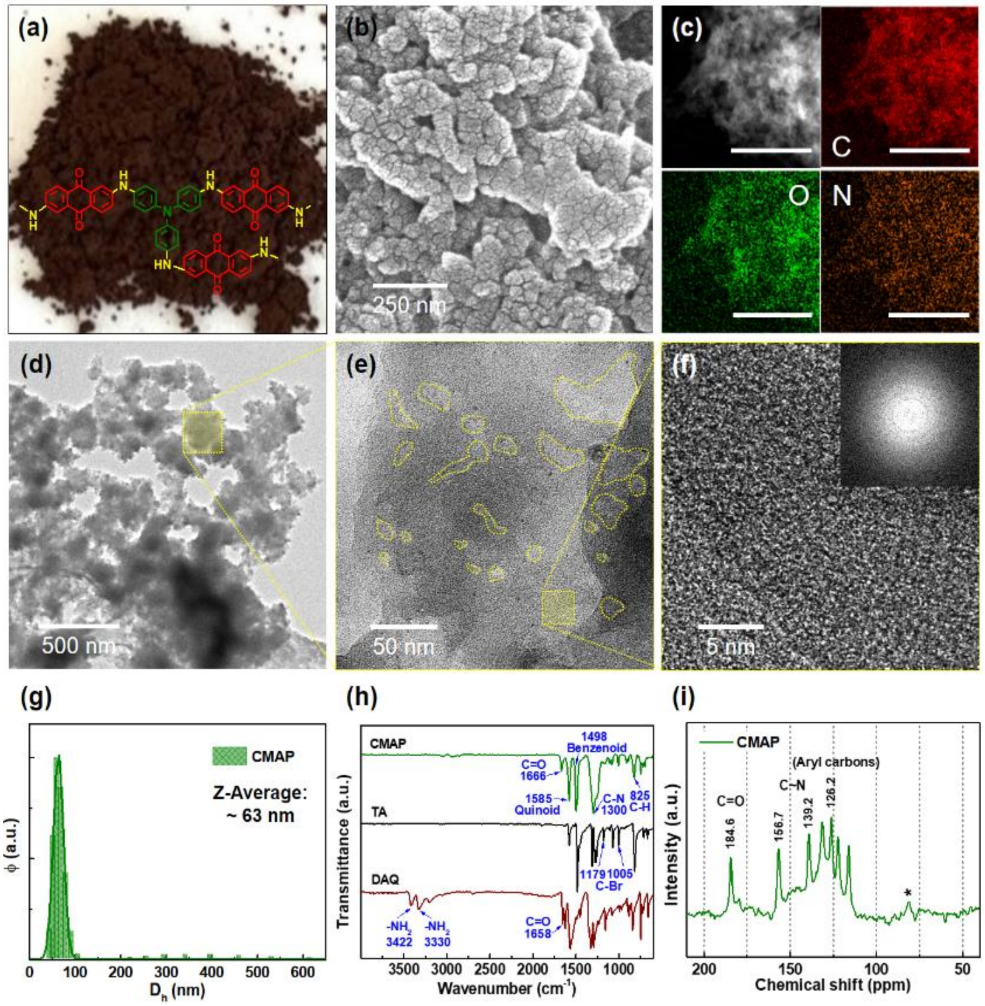

Figure 2.15. (a) Photograph with chemical structure of repeating unit, (b) FE-SEM image, (c) TEM image with the corresponding EDX mapping of carbon, oxygen, and nitrogen elements (scale bar: 500 nm), (d-f) TEM images with different magnification, (g) DLS histogram of hydrodynamic diameter (D_h) distribution with Z-average size of the as-synthesized CMAP; (h) FT-IR spectra of DAQ, TA, and (i) CMAP; and ^{13}C CP/MAS NMR spectrum of the CMAP. The inset in (f) shows the selected area electron diffraction (SAED) pattern indicating amorphous characteristics.

After examining the physical and chemical properties of AXGs and CMAP, respectively, the CMAP@AXG hybrid was synthesized by mixing the as-prepared AXG into BH coupling condition with precursors (DAQ and TA). Prior to the material characterization of the CMAP@AXG hybrids, it was necessary to determine whether GO undergoes wet-chemical reduction under BH coupling conditions. So, chemically reduced GO (C-rGO) was prepared through a BH coupling method without precursors and compared the properties with thermally reduced GO (T-rGO). Figure 2.16d and e exhibit FE-SEM images of the as-prepared T-rGO and C-rGO, respectively. Note that the GO and T-rGO are identical to A0G and rA0G mentioned in AXG characterization (see Figure 2.14), respectively. In Figure 2.16a, the Raman spectra of T-rGO and C-rGO display characteristic peaks at 1350 and 1580 cm^{-1} corresponding to the D (defect) band derived from the breathing mode of the aromatic ring and G (graphitic) band originating from the in-plane stretching vibration mode of the graphitic lattice (sp^2 carbon), respectively [29]. Interestingly, the I_D/I_G ratio of the C-rGO is 0.975, which is comparable to that of T-rGO (=rA0G, 1.043) as well as rA1G (1.016), rA4G (0.985), and rA8G (1.094) (Figure 2.14j). Furthermore, the TGA result in Figure 2.16b exhibits that the isotherm of C-rGO is also comparable to that of T-rGO before 300 °C, which is significantly different from that of pristine GO. The mass loss of C-rGO is relatively larger than that of T-rGO after 300 °C. However, this is due to residual oxygenated functional groups between the graphene layers re-stacked by van der Waals interaction during the wet-chemical reaction, and this can be partially resolved by mixing with polymer precursors with a low concentration of GO [33,34]. Through Raman and TGA analysis, it was confirmed that the wet-chemical reduction of GO under the BH coupling condition is exactly applicable to the next step for hybrid synthesis.

Next, to optimize the amount of graphene addition for CMAP@AXG synthesis, a series of CMAP@A0Gs were prepared using precursors and A0G dispersions (in anhydrous toluene) with different concentrations, i.e., 0.1, 0.2, 0.5, and 1.0 % (w/v) named CMAP@A0G-conc., i.e., CMAP@A0G-0.1, CMAP@A0G-0.2, CMAP@A0G-0.5, and CMAP@A0G-1.0, respectively. Figure 2.16c exhibits the TGA isotherms of pristine CMAP and CMAP@A0G-conc. hybrids obtained under the N_2 atmosphere. As the temperature increased, the mass of CMAP gradually decreased from around 300 °C and maintained a high residual mass of about 70 % or more when reaching 900 °C. This corresponds to the basic properties of a crosslinked CMAP network [4]. For the CMAP@A0G-conc., a characteristic weight loss was found starting at around 441 °C due to oxidation and decomposition of the exposed graphene sheets [34]. In addition, the difference between isotherms of each sample is observed according to the amount of graphene added. At 500 °C, the residual weight ratios of CMAP@A0G-0.1, CMAP@A0G-0.2, CMAP@A0G-0.5, and CMAP@A0G-1.0 are 67, 64, 59, and 53 %, respectively. And this result indicates that the degree of decrease in the weight ratio is proportional to the amount of graphene added. Based on the synthesis, electrode preparation, and EC performance evaluated in advance, the concentration of the AXG dispersion used in the CMAP@AXG hybrid synthesis was fixed as 0.5 % (w/v). Synthesis and characterization of CMAP@AXG hybrids were subsequently carried out using AXGs with different acid treatment times. The CMAP@AXG hybrids were denoted CMAP@A0G, CMAP@A1G, CMAP@A4G, and CMAP@A8G according to the acid treatment time for graphene activation used, i.e., 0, 1, 4, and 8 hours, respectively. Figure 2.16f-i show FE-SEM images to explain the morphology of the as-prepared CMAP@AXG hybrids. The CMAP@AXG hybrids were synthesized in a uniform mixture of CMAP and graphene. The size of the graphene sheet gradually decreased as the acid treatment time of AXG was increased from 0 to 8 hours. Moreover, to investigate the interfacial structure between CMAP and graphene inside the hybrid, the CMAP@A4G hybrid, which is the optimal sample, was observed by TEM at various magnifications as shown in Figure 2.13c-f. The TEM images show that CMAP is evenly distributed on the graphene sheets and connected to the graphene surface.

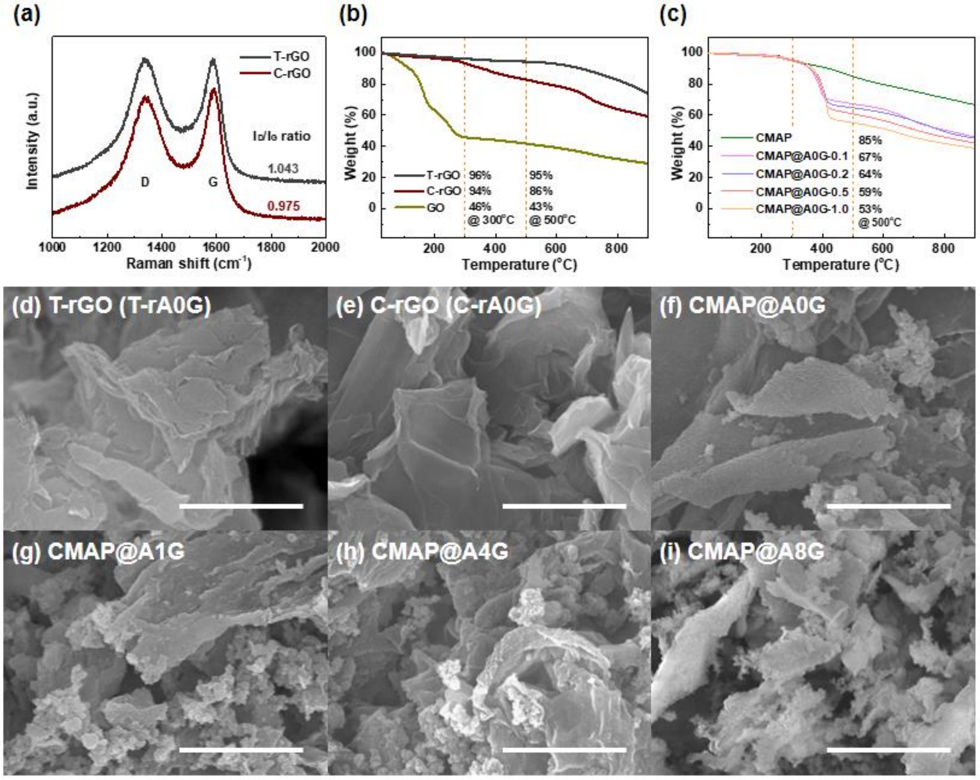

Figure 2.16. (a) Raman spectra of T-rGO and C-rGO; (b) TGA scans of T-rGO, C-rGO, and bare GO; (c) TGA scans of CMAP, CMAP@A0G-0.1, CMAP@A0G-0.2, CMAP@A0G-0.5, and CMAP@A0G-1.0; and FE-SEM images of (d) T-rGO (thermally reduced graphene oxide, T-rA0G), (e) C-rGO (wet-chemically reduced graphene oxide, C-rA0G), (f) CMAP@A0G, (g) CMAP@A1G, (h) CMAP@A4G, and (i) CMAP@A8G, respectively (scale bar: 5 μm).

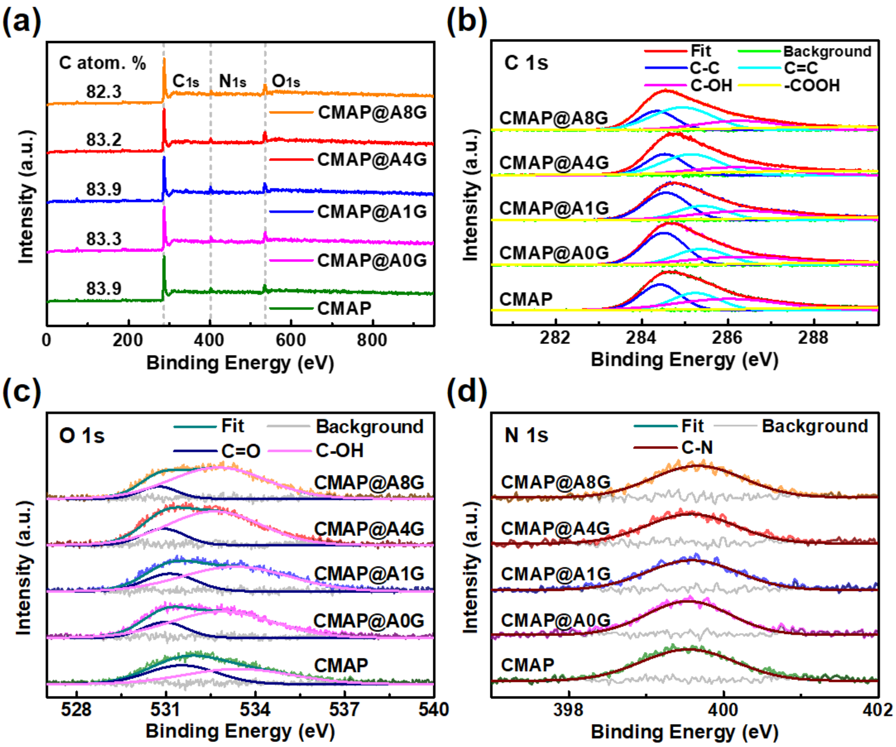

Figure 2.17. (a) XPS survey scanning spectra and core-level high-resolution (b) C 1s, (c) N 1s, and (d) O 1s XPS spectra of CMAP and CMAP@AXGs.

The elemental configuration and structural characteristics of CMAP and CMAP@AXG hybrids were evaluated by X-ray photoelectron spectroscopy (XPS), powder X-ray diffraction (XRD), and N_2 gas adsorption/desorption analysis. As shown in Figure 2.17a, the XPS spectra in the range of 0 to 950 eV show the presence of carbon (C 1s), nitrogen (N 1s), and oxygen (O 1s) atoms without impurities. The atomic and mass ratios of each element were analyzed to compare contents in the as-obtained samples. The carbon contents of CMAP, CMAP@A0G, CMAP@A1G, CMAP@A4G, and CMAP@A8G are measured to be 82.3, 83.2, 83.9, 83.3, and 83.9, respectively. In the experimental section, quantitatively optimized 0.5 % (w/v) graphene dispersion was used to synthesize CMAP@AXG hybrids. As a result, it is confirmed that the carbon contents of CMAP@AXG hybrids were increased by about 1 atomic % (≈1.5 wt.%) from that of CMAP. Furthermore, by adding the AXGs, the N/O ratio (%) of hybrid samples is decreased which implies the AXGs are successfully anchored with CMAP networks, and the surface affinity (wettability) and pseudocapacitive reactivity are enhanced [34]. Details of the as-measured atomic and mass ratio of carbon, nitrogen, and oxygen in each sample are shown in Table 2.8. To compare the detailed binding energy distributions of each sample, high-resolution C 1s, O 1s, and N 1s curves were fitted using a Gaussian function in Figure 2.17b-d. The deconvolution of XPS peaks assigned to C 1s components (see Figure 2.17b) reveals four distinctive peaks at 284.5, 285.2, 286.2, and 289.2 eV, which are consistent with the binding energies of C–C sp^3, C=C sp^2, C–OH, and –COOH carbons, respectively [21,22]. Two binding energy peaks of O 1s at 531.0 and 533.0 eV (see Figure 2.17c) are indicative of each sample corresponding to C=O and C–OH oxygens, respectively [30,35]. Moreover, N 1s peaks of each sample at a binding energy of 399.6 eV (see Figure 2.17d) are attributed to C–N nitrogen [36,37]. According to the peak area, the occupancy of C=C carbon, –COOH carbon, and C–OH oxygen increases as the acid treatment time of AXG incorporated in CMAP network increases. This result implies that the electrical conductivity can be improved by increasing π-π conjugated pairs inside the CMAP@AXG hybrids network. This also suggests that the ionic conductivity can be increased by forming additional defects (ion passage) with the hydrophilic functional groups of AXGs anchored in the hybrid network, which is in accordance with the zeta potential data in Figure 2.14i [18,24]. Consequently, these functional groups can further increase the surface affinity with electrolyte and the pseudocapacitive property via a Faradaic reaction.

The XRD patterns of the CMAP and CMAP@AXG hybrids are shown in Figure 2.18. A broad peak at $2\theta \approx 18°$ of CMAP and CMAP@AXG hybrids indicates that all samples are an amorphous structure. Moreover, the broad peak at $2\theta \approx 18°$ and a small peak at $2\theta \approx 40°$ of each sample originated from a certain amount of π–π stacking of aromatic units in the hybrid network [4,24]. Interestingly, all samples show no obvious carbon-related peak at about $2\theta \approx 26.5°$, and the $2\theta \approx 18°$ peak of CMAP@AXG hybrids is broader than that of CMAP. This indicates that the CMAP@AXG hybrid contains a very small amount of graphene uniformly distributed in the CMAP network, which also increases the amorphous properties of the hybrids.

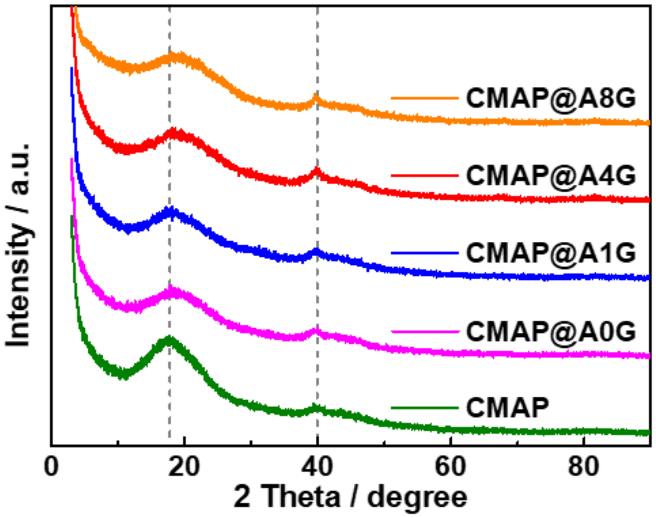

Figure 2.18. XRD patterns of CMAP and CMAP@AXG hybrids.

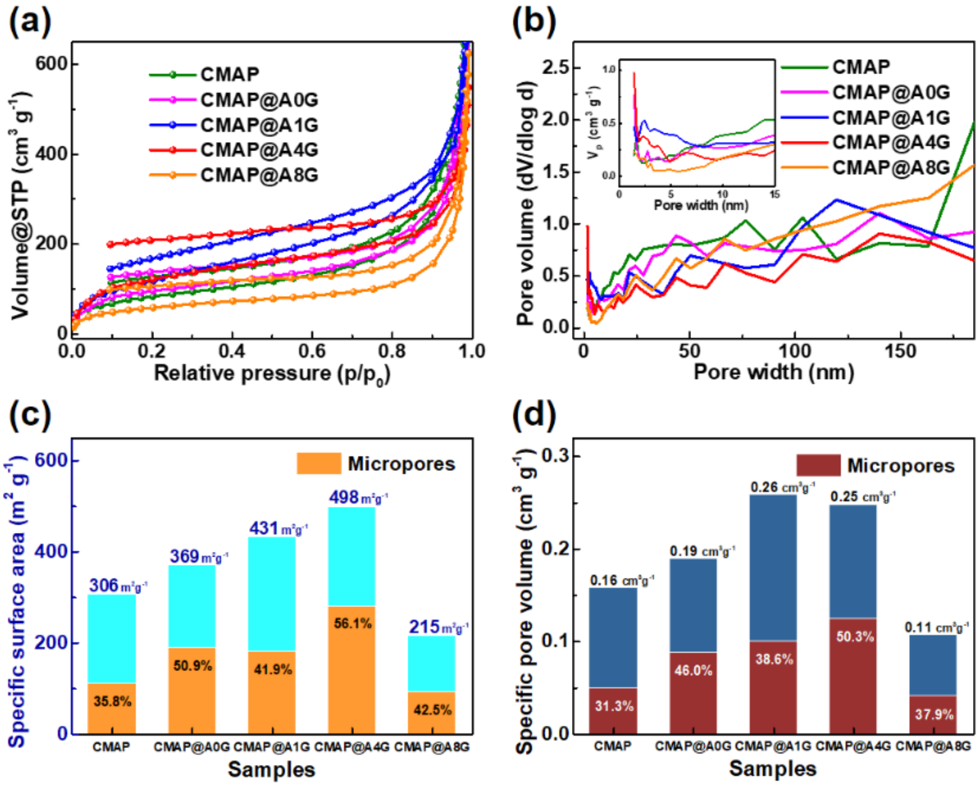

Figure 2.19. (a) N_2 adsorption/desorption isotherms, (b) BJH pore distribution diagrams, (c) BET specific surface area diagrams, and (d) specific pore volume diagrams of CMAP and CMAP@AXG hybrids, i.e., CMAP@A0G, CMAP@A1G, CMAP@A4G, and CMAP@A8G.

The porous characteristics of CMAP and CMAP@AXG hybrids were studied via N_2 adsorption/desorption measurements, and BET/BJH analysis was performed to determine the surface area, porosity, and pore size distribution of each sample as shown in Figure 2.19. The N_2 adsorption/desorption isotherms in Figure 2.19a exhibit a characteristic steep rise in the relative pressure (p/p_0) range above 0.9 suggesting that all samples possess an external surface area owing to inter-particulate pores, i.e., meso- and macropores. The rapid increase of isotherms also appeared in the low-pressure range below 0.02 which is originating from the microporous structure of polymer networks and graphene sheets [4,38]. As shown in Figure 2.19c, CMAP, CMAP@A0G, CMAP@A1G, CMAP@A4G, and CMAP@A8G show the BET specific surface areas of 308, 389, 431, 498, and 215 $m^2\ g^{-1}$, and the percentages of micropores are calculated as 35.8, 50.9, 41.9, 56.1, and 42.5 %, respectively. In the case of CMAP@A4G, which is the optimal condition, 56.1 % of the specific surface area is attributed to microporosity. This result shows that the incorporation of a small amount of AXG into CMAP affects the increase of polymer surface area by preventing re-stacking between themselves, which allows forming a 3D porous network. Figure 2.19b exhibits the pore size distribution of all samples obtained by the BJH method. And using this, the specific pore volume distribution for each sample is shown in Figure 2.19d. The specific pore volume and the percentage of micropores of CMAP, CMAP@A0G, CMAP@A1G, CMAP@A4G, and CMAP@A8G were found to be 0.16, 0.19, 0.26, 0.25, and 0.11 $cm^3\ g^{-1}$, and 31.3, 46.0, 38.6, 50.3, and 37.9 %, respectively. This result indicates that a hierarchically porous structure with a large fraction of micropores was successfully formed. Interestingly, the surface area and the pore volume of CMAP@A8G are drastically decreased compared to that of CMAP@A4G. We speculate that this result is due to the extensive re-stacking between small-sized graphene sheets during wet-chemical reaction because prolonged acid treatment time causes severe breakage of graphene flakes with many polar functional groups at the edges. This result correlates with the results previously mentioned in the AXGs characterization in Figure 2.14. Detailed data of the specific surface area and pore volume distribution of each sample are summarized in Table 2.6.

Table 2.6. BET surface area and BJH pore volume distribution data of rA0G, rA1G, rA4G, rA8G, CMAP@A0G, CMAP@A1G, CMAP@A4G, and CMAP@A8G.

Sample	S_{total}[a] / $m^2\ g^{-1}$	S_{micro}[b] / $m^2\ g^{-1}$	$V_{p,\ total}$[c] / $cm^3\ g^{-1}$	$V_{p,\ micro}$[d] / $cm^3\ g^{-1}$	$V_{p,\ meso}$[d] / $cm^3\ g^{-1}$	$V_{p,\ macro}$[d] / $cm^3\ g^{-1}$
rA0G	259	60.3 (24.9%)	0.51	0.024 (4.75%)	0.40 (78.2%)	0.087 (17.1%)
rA1G	558	180.0 (35.5%)	1.01	0.077 (7.61%)	0.90 (88.4%)	0.040 (3.98%)
rA4G	427	121.2 (31.1%)	0.78	0.052 (6.67%)	0.70 (89.1%)	0.033 (4.12%)
rA8G	563	157.4 (30.7%)	1.03	0.071 (6.89%)	0.92 (88.9%)	0.044 (4.26%)
CMAP	306	109.4 (35.8%)	0.16	0.049 (31.3%)	0.097 (61.7%)	0.011 (7.04%)
CMAP@A0G	369	187.9 (50.9%)	0.19	0.087 (46.0%)	0.092 (48.7%)	0.010 (5.24%)
CMAP@A1G	431	180.8 (41.9%)	0.26	0.100 (38.6%)	0.182 (70.5%)	0.010 (3.72%)
CMAP@A4G	498	279.3 (56.1%)	0.25	0.125 (50.3%)	0.116 (46.9%)	0.007 (2.77%)
CMAP@A8G	215	91.2 (42.5%)	0.11	0.040 (37.9%)	0.056 (52.2%)	0.011 (9.91%)

[a, b] determined by standard BET method; [c, d] determined by BJH method at a pressure of $p/p_0 = 0.99$.

Table 2.7. Parameters of zeta potential plot of AXGs.

Sample	**Average zeta potential / mV**
A0G	-32.02 ± 1.11
A1G	-35.60 ± 0.97
A4G	-35.58 ± 0.94
A8G	-37.08 ± 1.03

Table 2.8. Atomic and mass ratio of CMAP and CMAP@AXG hybrids measured by XPS.

Sample	**Atomic ratio / %**		
	Carbon	**Nitrogen**	**Oxygen**
CMAP	82.3 (±1.3)	5.6 (±0.9)	12.1 (±1.1)
CMAP@A0G	83.2 (±1.3)	5.4 (±0.8)	11.4 (±1.2)
CMAP@A1G	83.9 (±1.1)	4.9 (±0.8)	11.2 (±0.8)
CMAP@A4G	83.3 (±1.0)	5.0 (±0.8)	11.7 (±0.7)
CMAP@A8G	83.9 (±1.1)	4.9 (±0.8)	11.2 (±0.8)

Sample	**Weight ratio / %**		
	Carbon	**Nitrogen**	**Oxygen**
CMAP	78.3 (±1.5)	6.3 (±1.0)	15.4 (±1.3)
CMAP@A0G	79.4 (±1.5)	6.0 (±0.8)	14.6 (±1.4)
CMAP@A1G	80.2 (±1.3)	5.5 (±0.9)	14.3 (±1.0)
CMAP@A4G	79.6 (±1.2)	5.5 (±0.9)	14.9 (±0.9)
CMAP@A8G	80.2 (±1.3)	5.5 (±0.9)	14.3 (±1.0)

To investigate the influence of AXG incorporation on the electrical conductivity of the CMAP network, the sheet resistance of CMAP, CMAP@A0G, CMAP@A1G, CMAP@A4G, and CMAP@A8G electrodes was measured. As shown in Figure 2.20, a slurry mixture and a film of each sample were prepared in the same manner as the electrode for electrochemical measurement, except that the mixture was cast on a slide glass to remove the effect on the conductivity of a graphite foil, which is a current collector. The average sheet resistances of each sample are 689.8 ± 50.1, 418.0 ± 70.8, 390.9 ± 45.9, 303.4 ± 2.2, and 277.9 ± 5.2 Ω sq^{-1}, respectively (see Table 2.9). This result shows that the incorporation of AG with extended acid treatment time into CMAP contributes to the improvement of electrical conductivity leading to a higher charge transfer, which supports that the as-prepared CMAP@AXG hybrids satisfy electrical requirements for supercapacitor application. Specifically, the CMAP is a 3D porous structure composed of conjugated polymer chains. When graphene is added during the BH coupling reaction, the graphene flakes are incorporated into the polymer networks. This not only prevents self-aggregation of CMAP but also supplements electrical conductivity. In addition, as the acid treatment time of AXG is increased, the flake size of porous graphene is reduced and furthermore increases the surface affinity. Therefore, they can be uniformly incorporated into the CMAP network, and as a result, improves the electrical conductivity of the composite film [39].

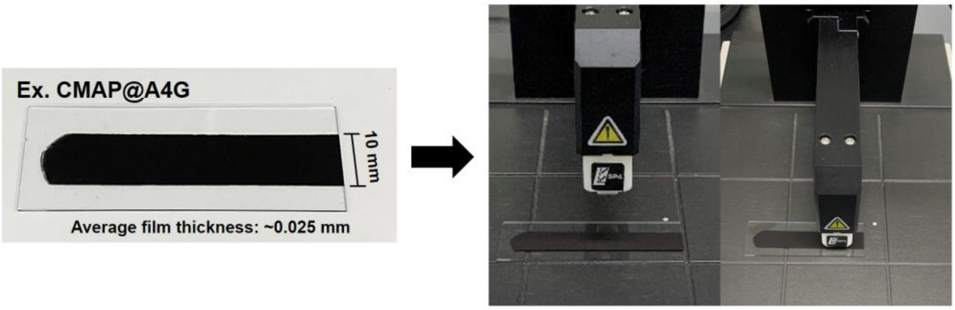

Figure 2.20. Sheet resistance measurement preparation. To eliminate the effect of graphite foil, a slurry mixture in a mass ratio of CMAP@AXGs (or CMAP) (0.1g):SuperP:PVDF binder = 80:10:10 dispersed in NMP was cast on slide glass and dried.

Table 2.9. Sheet resistances of CMAP, CMAP@A0G, CMAP@A1G, CMAP@A4G, and CMAP@A8G.

Sample	**Sheet resistance / Ω square^{-1}**
CMAP	689.8 ± 50.1
CMAP@A0G	418.0 ± 70.8
CMAP@A1G	390.9 ± 45.9
CMAP@A4G	303.4 ± 2.2
CMAP@A8G	277.9 ± 5.2

* Slide glass (1 ± 0.05 mm in thickness): insulator; sample film thickness: 25 ± 1 μm.

The EC performances of CMAP, AXGs, and CMAP@AXG hybrids-coated electrodes were first evaluated in a three-electrode configuration using a 1.0 M H_2SO_4 aqueous electrolyte. Figure 2.21a and b show photographs of a typical flexible CMAP@A4G electrode, which is an optimal sample, and FE-SEM images at different magnifications of the CMAP@A4G electrode surface, respectively. All samples can be readily applied to homogeneous and flexible electrodes owing to their good dispersibility in a polar solvent, i.e., NMP, as shown exemplarily for the CMAP@A4G hybrid. One thing to note in the electrode preparation process is whether an electrode active material film cannot be manufactured using a slurry in which CMAP and AXG are separately mixed without synthesizing CMAP@AXG hybrids. However, even if the two materials mentioned above were sufficiently mixed and introduced into the current collector through the hand mill process, cracks occurred and detached during the annealing process of the active material film due to restacking of graphene and reaggregation between conductive polymer chains. Although this phenomenon can be partially solved by increasing the amount of binder added, it causes problems such as reduced conductivity, porosity, and stability of the film. And this eventually negatively affects the electrochemical performance of the supercapacitor using redox characteristics and a large specific surface area. Therefore, this is the reason why the hybrid synthesis method was used rather than simply mixing the conductive polymer and the active graphene, and a significant electrochemical performance improvement effect was achieved through optimization of the next step.

Figure 2.22 exhibits the EC performances of CMAP, AXGs, and pristine graphite foil (as substrate or current collector). Figure 2.22a-d show CV and GCD curves, specific capacitances at different current densities, and Nyquist plots of CMAP, A0G, A4G, and graphite foil (as a substrate) obtained in a three-electrode configuration using 1.0 M H_2SO_4 electrolyte. Also, the detailed CV and GCD curves of each sample are summarized in Figure 2.22e-j. Figure 2.22a clearly displays the rectangular-shaped CV curve of CMAP with a pair of redox peaks located at about 0.48 and 0.50 V measured at a scan rate of 10 mV s^{-1}. Figure 2.22e shows the cyclic voltammetry (CV) curves of the as-prepared CMAP obtained at various scan rates ranging from 10 to 100 mV s^{-1} exhibiting typical pseudocapacitive characteristics. As the sweep rate increased tenfold from 10 to 100 mV s^{-1}, the positions of the reductive and oxidative peaks shifted from 0.48 to 0.43 V and from 0.5 to 0.55 V, respectively. This indicates the rapid transport of ions and electrons, which means that the CMAP has excellent charge/discharge characteristics and rate capability [15]. Galvanostatic charge/discharge (GCD) measurement was performed to evaluate accurate specific capacitances. Based on the discharge time, the specific capacitance of CMAP was calculated to be 464 F g^{-1} at 1.0 A g^{-1} (see Figure 2.22b). In the case of graphene, CV curves of A0G and A4G show typical quasi-rectangular shapes with a slight distortion due to oxygen atoms in the porous carbon lattice (see Figure 2.22a). As shown in Figure 2.22g and i, the CV curves maintain their shapes even at high scan rates, suggesting an EDLC behavior and a fast ion diffusion. Peaks related to the redox reaction in the middle potential range were not observed, and the CV curve area of A4G was much larger than that of A0G indicating the highly activated porous graphene directly affects the improvement of EC reactivity. Figure 2.22b exhibits GCD curves of A0G and A4G showing highly linear and symmetric triangular shapes, which also implies the typical capacitive behaviors of EDLC. The specific capacitances of A0G and A4G were obtained 282 and 497 F g^{-1} at a current density of 1 A g^{-1}, suggesting the acid treatment of graphene greatly enhances their capacitance [18,19]. In the overall electrochemical test, the graphite foil exhibited featureless performance. According to Figure 2.22a and b, the black curve which corresponds to the graphite foil current collector exhibits negligible capacitance (< 20 F g^{-1} at 1 A g^{-1}). When the current density was increased from 1 to 50 A g^{-1}, the specific capacitances of A0G and A4G were maintained at about 83~84 % of their initial capacitance, whereas that of CMAP was retained at about 57 % (263 F g^{-1} at 50 A g^{-1}, see Figure 2.22c). This is attributed to the better electrical conductivity of graphene, which can be explained by the faster rising of Nyquist plots in the middle frequency region implying lower surface and internal resistance as shown in Figure 2.22d [34]. The detailed specific capacitance based on Galvanostatic discharge time of the A0G, A4G, and CMAP are summarized in Table 2.10, respectively.

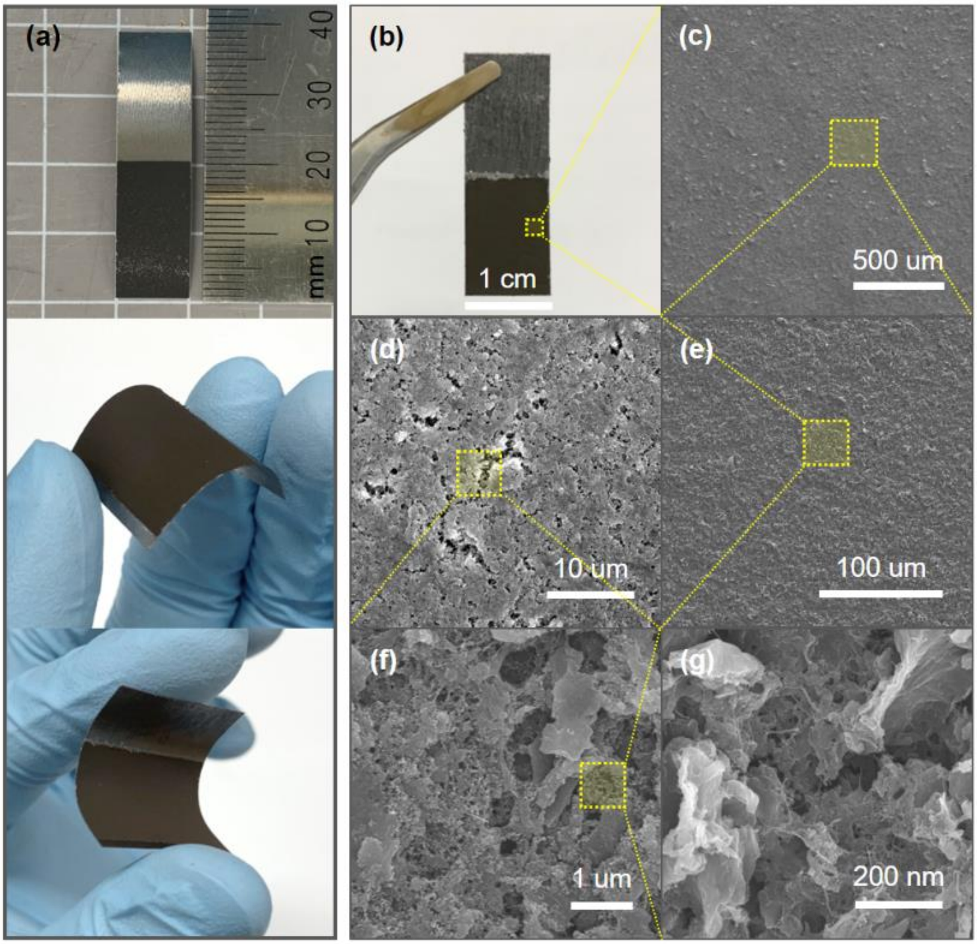

Figure 2.21. (a, b) Photographs and (c-g) FE-SEM images at different magnification of flexible CMAP@A4G electrode.

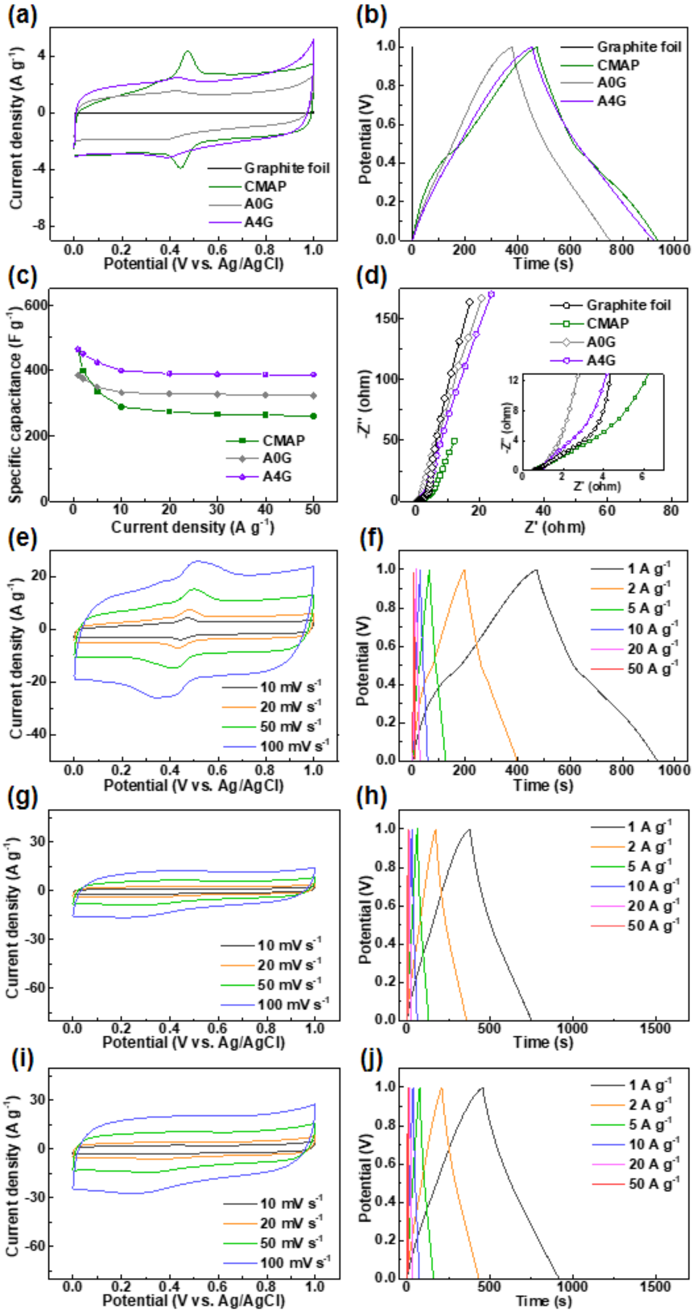

Figure 2.22. Electrochemical performance of CMAP, A0G, A4G, and graphite foil in a three-electrode system using 1.0 M H_2SO_4 electrolyte: (a) CV curves at a scan rate of 10 mV s^{-1}, (b) GCD curves at a current density of 1 A g^{-1}, (c) specific capacitances ranging from 1 to 50 A g^{-1}, (d) Nyquist plots in frequency range of 100 kHz – 10 mHz (inset: enlargement of the high-frequency region); CV and GCD curves of (e, f) CMAP, (g, h) A0G, and (i, j) A4G, respectively, in the positive potential range of 0–1.0 V.

Back to CMAP@AXG hybrids, to optimize the amount of graphene added into the CMAP network, CMAP@A0G-conc., i.e., CMAP@A0G-0.1, CMAP@A0G-0.2, CMAP@A0G-0.5, and CMAP@A0G-1.0 hybrid electrodes were prepared according to the concentration of A0G dispersion we used, i.e., 0.1, 0.2, 0.5, and 1.0 % (w/v), respectively. Then, their EC performance was measured and compared with the data from CMAP as shown in Figure 2.23. Figure 2.23a exhibits CV curves of CMAP and CMAP@A0G-conc. hybrids obtained at a scan rate of 10 mV s^{-1}. Interestingly, the redox peaks around 0.48 and 0.5 V broadened, and their intensity also increased, and additional peaks were observed at 0.14 and 0.18 V in CMAP@A0G-conc. hybrids. This is because the incorporation of graphene sheets into the CMAP network formed a 3D porous composite with a larger surface area exposing functional groups, and as a result, the charge/ion mobility and redox reactivity can be improved [15-17]. Figure 2.23b and c show GCD curves and rate capability data of CMAP and CMAP@A0G-conc. hybrids, respectively. The specific capacitances of CMAP, CMAP@A0G-0.1, CMAP@A0G-0.2, CMAP@A0G-0.5, and CMAP@A0G-1.0 are 464, 501, 538, 665, and 650 F g^{-1} at 1.0 A g^{-1} as well as 263, 291, 322, 436, and 401 F g^{-1} at 50 A g^{-1}, respectively. Accordingly, when the scan rate was increased from 1 to 50 A g^{-1}, the specific capacitance retention values were calculated to be 56.7, 58.1, 59.9, 65.6, and 61.7 %, respectively. The detailed CV and GCD curves, and specific capacitances at different current densities of CMAP@A0G-conc. hybrids are shown in Figure 2.24 and Table 2.10, respectively. As the amount of graphene added increased, the charge/ion conductivity and surface area were improved, so that the specific capacitance was enhanced from 464 F g^{-1} (CMAP) to 665 F g^{-1} (CMAP@A0G-0.5), and the specific capacitance retention value also increased from 56.7 (CMAP) to 65.6 % (CMAP@A0G-0.5), respectively. The CMAP@A0G-1.0, however, showed relatively low EC performance compared to that of CMAP@A0G-0.5. The reason seems to be that the surface area and conductivity were low due to the re-stacking of graphene sheets and the agglomeration of CMAP itself by using an excessive amount of graphene sheets in the synthesis procedure. Figure 2.23d shows the Nyquist plots of each sample. As described above, the charge/ion conductivity was improved through the A0G incorporation, but the difference in EIS data according to the amount of A0G added was insignificant. As a result, the concentration of AXG dispersion was fixed at 0.5 % (w/v), and CMAP@AXG hybrids were prepared by using AXGs with different acid-treatment times, i.e., 0, 1, 4, and 8 hours.

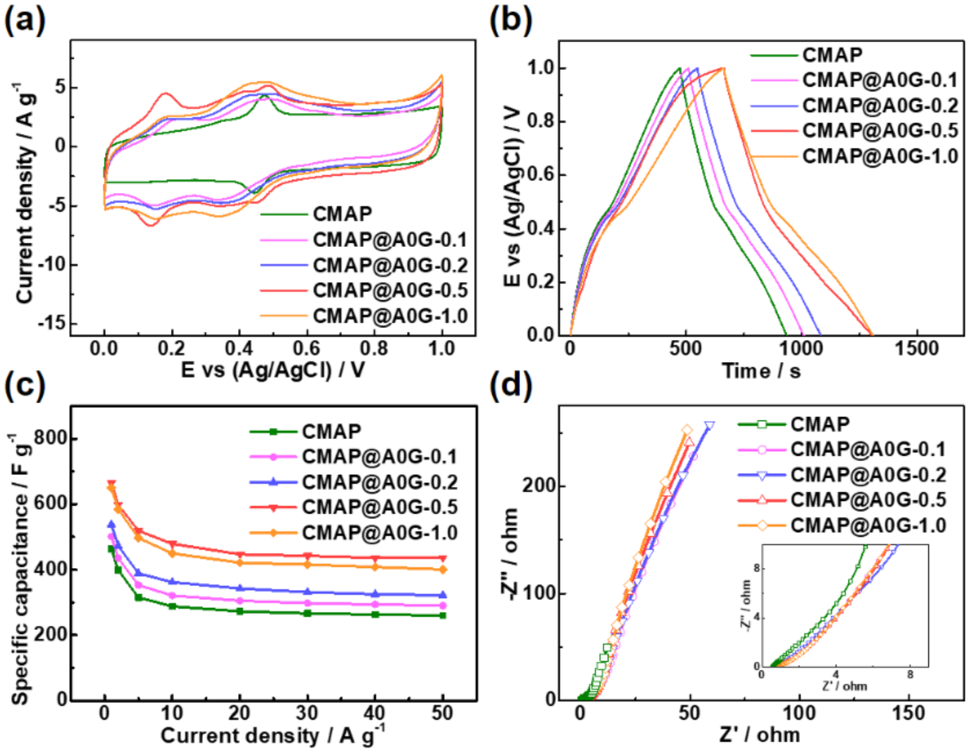

Figure 2.23. Electrochemical performance of CMAP, CMAP@A0G-0.1, CMAP@A0G-0.2, CMAP@A0G-0.5, and CMAP@A0G-1.0 in a three-electrode system using 1.0 M H_2SO_4 electrolyte: (a) CV curves at a scan rate of 10 mV s^{-1}, (b) GCD curves at a current density of 1 A g^{-1}, (c) specific capacitance obtained at different scan rates from 1 to 50 A g^{-1}, and (d) Nyquist plots in a frequency range of 100 kHz – 10 mHz (inset: enlargement of the high-frequency region).

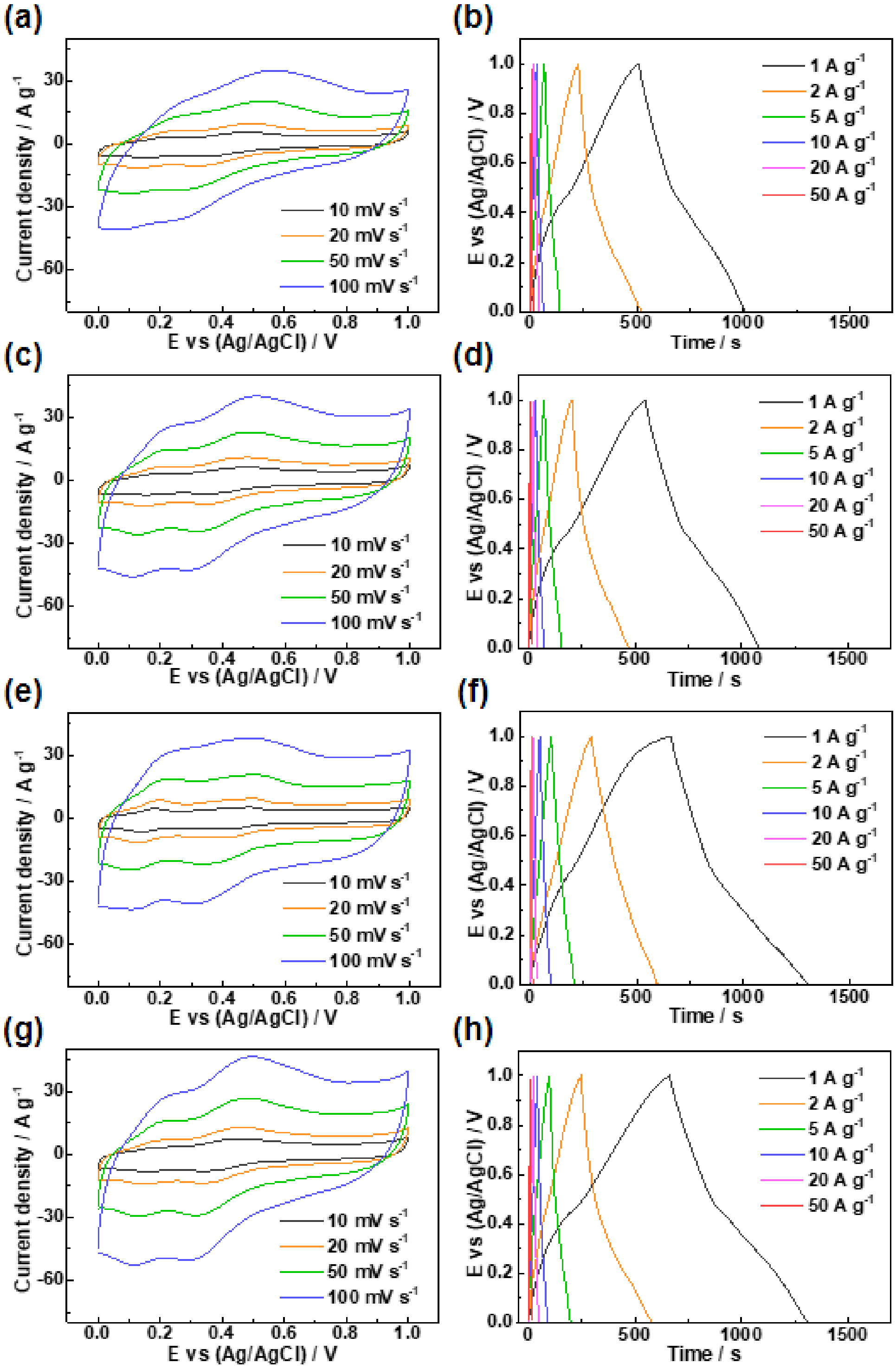

Figure 2.24. CV and GCD curves of (a, b) CMAP@A0G-0.1, (c, d) CMAP@A0G-0.2, (e, f) CMAP@A0G-0.5, and (g, h) CMAP@A0G-1.0 in a three-electrode system using 1.0 M H_2SO_4 electrolyte.

Afterward, EC performance measurements of the as-prepared electrodes coated with CMAP@AXGs, i.e., CMAP@A0G, CMAP@A1G, CMAP@A4G, and CMAP@A8G, were measured. Figure 2.25a shows CV curves of CMAP and CMAP@AXG hybrids at a scan rate of 10 mV s^{-1}, and the corresponding capacitances at different scan rates were calculated based on the integration of the CV curves. As shown in Table 2.11, the specific capacitance of CMAP is ≈461 F g^{-1} at a scan rate of 10 mV s^{-1}, and the value increases up to ≈950 F g^{-1} (for CMAP@A4G) as the addition of activated graphene. This is the result of amplification of the redox activity of coupled electroactive moieties due to the homogeneous incorporation of graphene with a large surface area and conductivity [4,40]. GCD measurements of CMAP@AXG hybrids were conducted to evaluate more accurate specific capacitances. Figure 2.25b displays GCD curves of CMAP, CMAP@A0G, CMAP@A1G, CMAP@A4G, and CMAP@A8G at a current density of 1 A g^{-1}. Moreover, the specific capacitances calculated based on Galvanostatic discharge time at different current densities are exhibited in Figure 2.25c and Table 2.10. Detailed CV and GCD curves of CMAP@AXG hybrids are shown in Figure 2.26. The specific capacitances of CMAP, CMAP@A0G, CMAP@A1G, CMAP@A4G, and CMAP@A8G are 464, 665, 686, 751, and 513 F g^{-1} at 1.0 A g^{-1} as well as 263, 436, 460, 533, and 337 F g^{-1} at 50 A g^{-1}, respectively. Accordingly, when the scan rate was increased from 1 to 50 A g^{-1}, the specific capacitance retention values were calculated to be 56.7, 65.6, 67.1, 71.0, and 65.7 %, respectively. Obviously, CMAP@A4G displays the best EC energy storage ability exhibiting a specific capacitance of 751 F g^{-1} at 1.0 A g^{-1} and 513 F g^{-1} at 50 A g^{-1} (68.3 % of specific capacitance retention). In the case of CMAP@A8G, the EC performance is relatively very low. Since the graphene fragments were severely broken by excessive acid treatment, a stable porous structure could not be maintained. Therefore, the charge/ion conductivity also could not be improved even when a composite was formed with a CMAP network. This is consistent with the results of N_2 adsorption/desorption and sheet resistance measurements as dealt with Figure 2.19 and Table 2.9. Figure 2.25d shows the Coulombic efficiencies of CMAP and CMAP@AXGs calculated by GCD data at different current densities from 1 to 50 A g^{-1}. CMAP exhibits the Coulombic efficiencies of 91.6−98.7 %. However, the values of CMAP@AXG hybrids are significantly enhanced to 96.9−99.6 %. This is because better charge/ion conductivity was achieved by incorporating activated graphene into the CMAP network providing a passage of an appropriate size for facile movement of charge and ions during reaction [15]. Electrochemical impedance spectroscopy (EIS) analysis was performed to predict the electrochemical kinetics, internal and charge transfer resistances of CMAP and CMAP@AXG hybrids. The EIS behaviors of all samples were measured in the frequency range of 100 kHz – 10 mHz in 1.0 M H_2SO_4 electrolyte and the resultant Nyquist plots are presented in Figure 2.25e. The diffusion layer resistance of each sample in the high-frequency region behaves like a pure resistor typically found for non-metallic materials. The plots of middle-range frequencies imply small deviations indicative of low conductivity due to hierarchical porosity and pseudocapacitance. Moreover, the quasi-vertical profile at low frequencies indicates a nearly ideal capacitive behavior, which means efficient diffusion of the electrolyte to the active material surface [41]. The EIS results are further demonstrated by fitting parameters according to the electrical equivalent circuit as shown in Figure 2.26f. The R_{el}, R_s, and R_{ct} represent the electrolyte-electrode resistance, surface resistance, and internal charge transfer resistance, respectively. Also, the C_s, C_{dl}, and W_s indicate the surface layer geometrical capacitance, electric-double-layer capacitance, and surface layer diffusion impedance, respectively [42,43]. As the acid treatment time of AXG increases, the values of the internal and charge transfer resistances (R_{el}, R_s, and R_{ct}) decrease and the values of capacitances (C_s and C_{dl}) increase. These results represent that the accessibility of charge and ion is improved by the formation of hierarchically porous conductive networks and the exposure of redox-active functional groups. Note that CMAP@A4G shows the lowest impedance, i.e., reaction resistance, and the highest capacitance values due to the rapid charge and ion transfer resulting from the stable 3D hybrid structure, suitable conductivity, and reactivity. Detailed values of the fitting parameters for each sample are summarized in Table 2.12. Based on the specific capacitance attained by the optimal CMAP@A4G electrode (533–751 F g^{-1}), the values are exceptional to other comparable materials, i.e., conducting polymers or CMPs (335–576 F g^{-1}) [3,4,44,45], MOFs (3 mF cm^{-2} or 416 F g^{-1}) [46,47], metal/polymer/carbon composites (385–759 F g^{-1}) [15,48,49], and CMP or MOF-derived N/O-doped porous carbons [50,51]. Some composite electrode materials have reported higher capacity values, i.e., polyaniline/mesoporous carbon composites (PANI/MPC, 900 F g^{-1}) [52], graphene/CNT hydrogel with nickel-cobalt hydroxide composites (GCH-NC, 759 F g^{-1}) [20], and graphene/polyaniline nanowires on nitrogen-doped carbon fabrics (RGO/PANI/eCFC, 1145 F g^{-1}) [53], but require energy-intensive multistep procedures, i.e., pyrolysis, solvothermal, or purification steps. Therefore, to the best of our knowledge, the accomplishment of the CMAP@A4G hybrid is competitive with those of recently reported organic-based composites for supercapacitor electrodes. Detailed information on the above-mentioned active materials is summarized in Table 2.13.

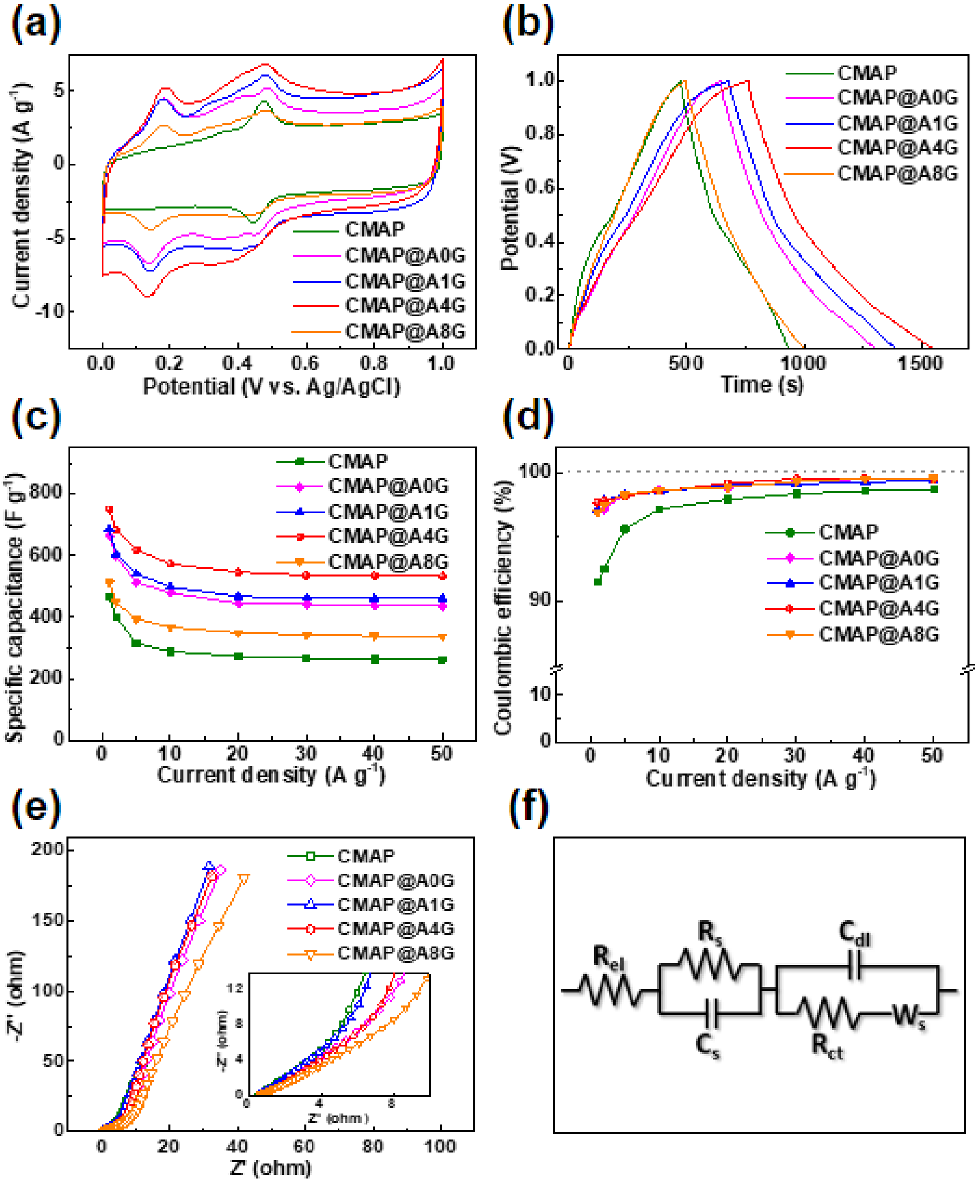

Figure 2.25. Electrochemical performance of CMAP, CMAP@A0G, CMAP@A1G, CMAP@A4G, and CMAP@A8G in a three-electrode system using 1.0 M H_2SO_4 electrolyte: (a) CV curves at a scan rate of 10 mV s^{-1}, (b) GCD curves at a current density of 1 A g^{-1}, (c) specific capacitance and (d) Coulombic efficiency obtained at different scan rates from 1 to 50 A g^{-1}, (e) Nyquist plots in a frequency range of 100 kHz – 10 mHz (inset: enlargement of the high-frequency region), and (f) electrical equivalent circuit used for fitting impedance spectra.

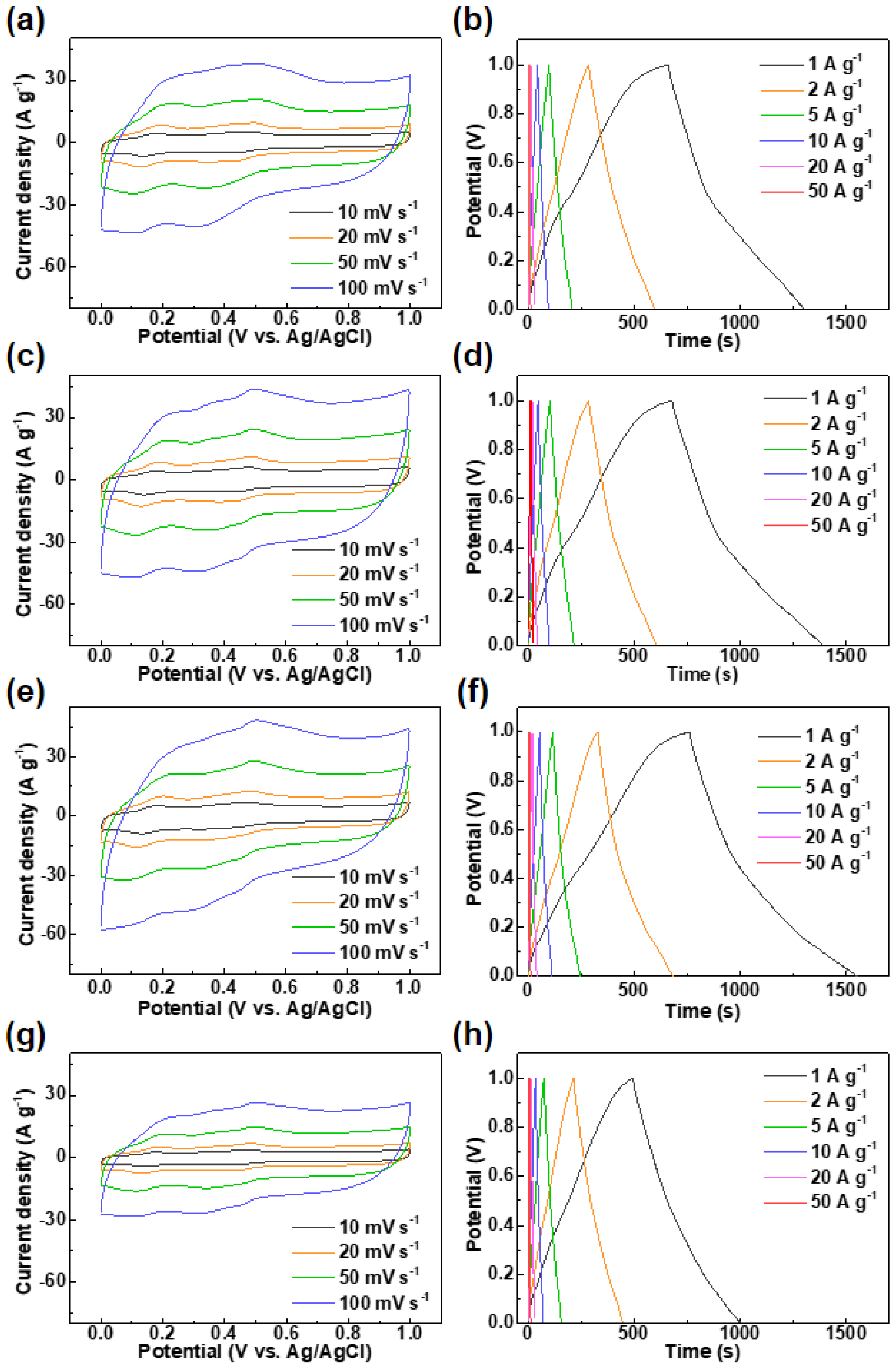

Figure 2.26. CV and GCD curves of (a, b) CMAP@A0G, (c, d) CMAP@A1G, (e, f) CMAP@A4G, and (g, h) CMAP@A8G in a three-electrode system using 1.0 M H_2SO_4 electrolyte.

Table 2.10. The capacitance calculated based on Galvanostatic discharge time.

Sample	**C_T / F g^{-1}**							
	1 A g^{-1}	**2 A g^{-1}**	**5 A g^{-1}**	**10 A g^{-1}**	**20 A g^{-1}**	**30 A g^{-1}**	**40 A g^{-1}**	**50 A g^{-1}**
A0G	282	261	230	210	197	194	192	192
A4G	497	455	419	394	373	370	368	368
CMAP	464	399	315	288	273	267	263	263
CMAP@A0G-0.1	501	435	353	321	305	298	294	291
CMAP@A0G-0.2	538	473	389	362	343	331	325	322
CMAP@A0G-1.0	650	585	497	450	422	416	408	401
CMAP@A0G-(0.5)	665	598	513	479	444	442	436	436
CMAP@A1G	686	606	542	498	467	462	461	460
CMAP@A4G	751	683	618	573	547	536	535	533
CMAP@A8G	513	448	393	367	349	343	339	337

Table 2.11. The capacitance calculated based on CV scans.

Sample	**C_T / F g^{-1}**			
	10 mV s^{-1}	**20 mV s^{-1}**	**50 mV s^{-1}**	**100 mV s^{-1}**
CMAP	461	422	385	356
CMAP@A0G	723	676	614	554
CMAP@A1G	864	803	719	640
CMAP@A4G	950	875	766	707
CMAP@A8G	524	487	436	388

To demonstrate the cycle stability of the CMAP@A4G electrode, GCD measurement at a current density of 10 A g^{-1} for 20,000 times was conducted. As can be seen in Figure 2.27a, approximately 95 % of the initial capacitance value and Coulombic efficiencies (96–98 %) were maintained during the entire cycling test, indicating excellent electrochemical stability and reversibility of the pseudocapacitive reaction. Furthermore, the ex-situ characterization of CMAP@A4G was performed to confirm the chemical and morphological changes before and after charge/discharge cycles. Figure 2.27b shows the FT-IR spectra before and after the cycle of the CMAP@A4G used as the electrode active materials. The aryl C–H peak at 825 cm^{-1}, which is not affected by charge/discharge, was used for calibration. After 20,000 charge/discharge cycles, all peaks of C–N, benzenoid, quinoid, and C=O bonds at 1300, 1498, 1585, and 1666, respectively, involved in the pseudocapacitive reaction were preserved in the same position as the spectra of the sample before cycle test, and there was only a very slight decrease in intensity. Also, the FE-SEM images in Figure 2.27c and d exhibit that the sample maintains the morphologies. This indicates that the electrochemical durability and reversibility are significantly improved compared to conventional conductive polymers by uniformly and stably forming a porous hybrid network between polymer and graphene. As a result, the CMAP@A4G achieved excellent cycle stability with good capacitance and Coulombic efficiency maintenance.

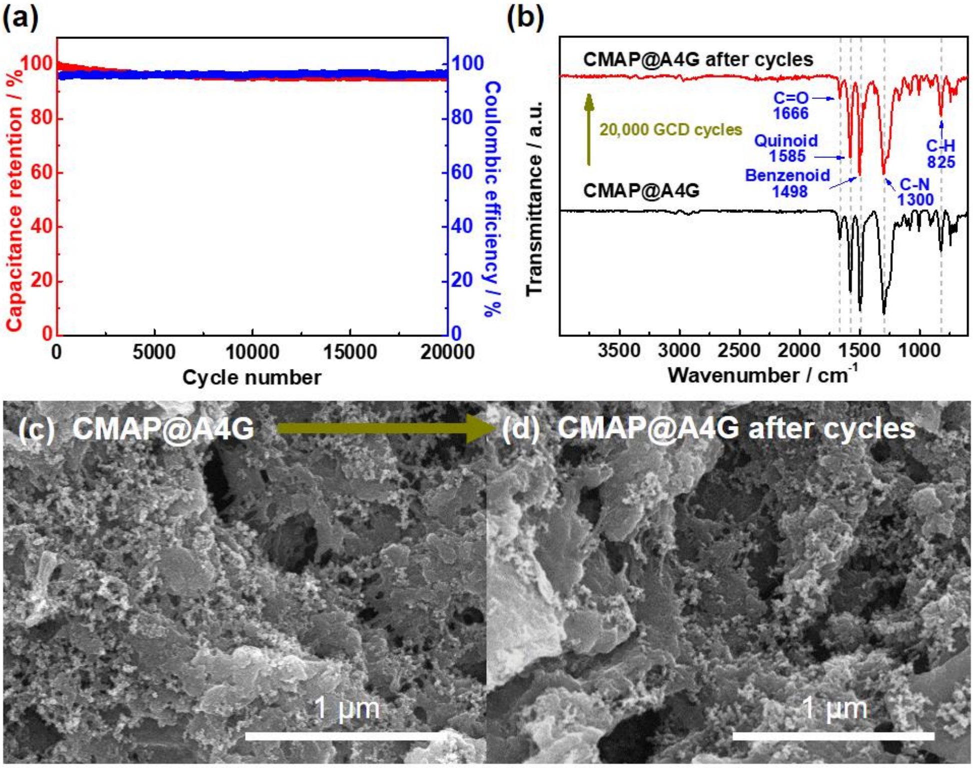

Figure 2.27. (a) Capacitance retention and Coulombic efficiency of CMAP@A4G electrode in a three-electrode system upon 20,000 GCD cycles at a current density of 10 A g^{-1}; (b) FT-IR spectra and (c, d) FE-SEM images of CMAP@A4G used as an electrode before and after 20,000 GCD cycles.

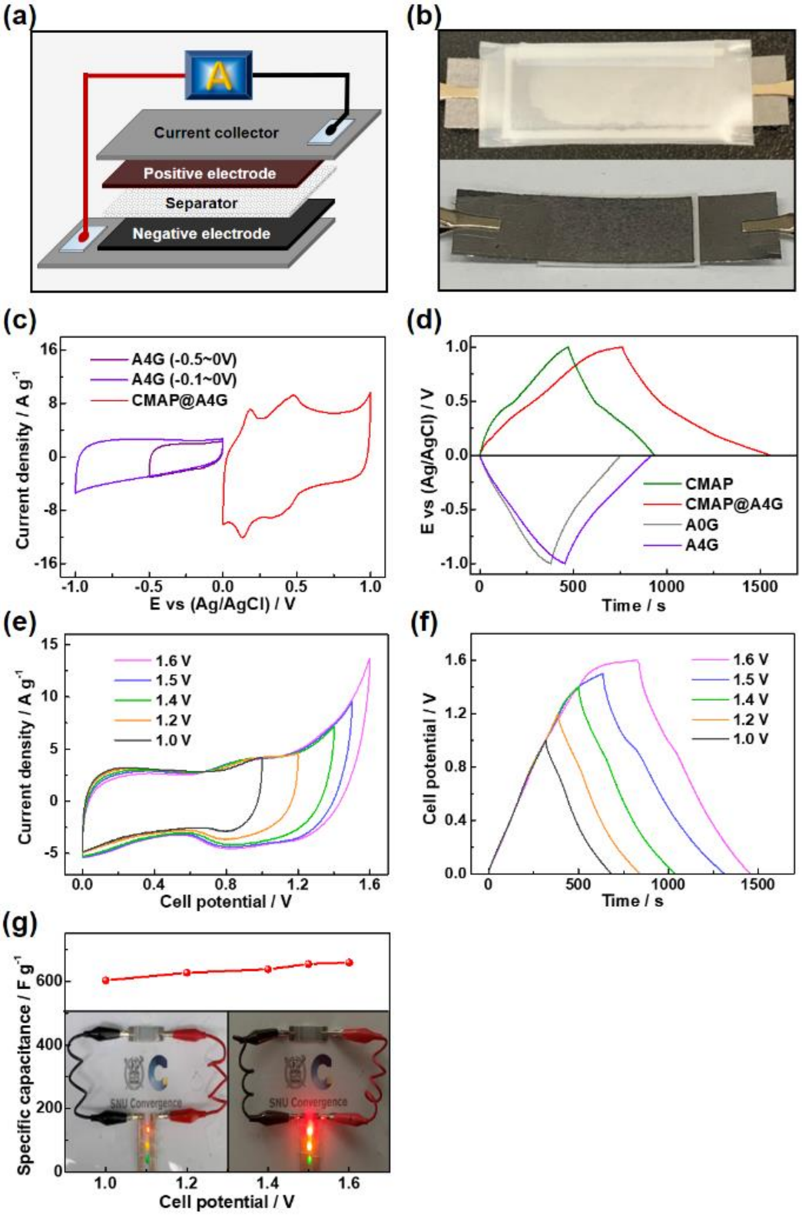

Figure 2.28. (a) Schematic illustration and (b) picture of CMAP@A4G//A4G ASC device composed of CMAP@A4G cathode, A4G anode, filter paper (separator), and graphite foil (current collector); (c) CV curves of A4G and CMAP@A4G electrodes at a scan rate of 10 mV s^{-1} and (d) potential-time curves of CMAP, CMAP@A4G, A0G, and A4G vs. Ag/AgCl reference electrode at a current density of 1 A g^{-1} in a three-electrode configuration using 1.0 M H_2SO_4 electrolyte; (e) CV curves of the ASC device collected at different voltage ranges at a scan rate of 10 mV s^{-1}; (f) GCD curves of the ASC device measured at different voltage ranges at a current density of 1 A g^{-1}; and (g) specific capacitance of the ASC device obtained at different voltage ranges with inset showing light up three LEDs (red, yellow, and green colors; bright (left) and dark (right) space, respectively).

Based on the three-electrode configuration evaluation, it was confirmed that the optimized CMAP@A4G hybrid is very suitable for the electrochemical energy storage device. Next, as shown in Figure 2.28a and b, an asymmetric supercapacitor (ASC) device was prepared for full-cell application using the CMAP@A4G as the positive electrode and the as-prepared A4G as the negative electrode. The EC performances, i.e., CV, GCD, EIS, cycle, and flexibility tests, of the CMAP@A4G//A4G ASC device were evaluated in a two-electrode system in 1.0 M H_2SO_4/PVA quasi-solid-state electrolyte. Before measuring the full-cell device, it was confirmed that charge can be stored in a voltage range from -1.0 to +1.0 vs. Ag/AgCl by conducting CV measurement of A4G and CMAP@A4G in a three-electrode system as shown in Figure 2.28c. Also, the specific capacitance of each electrode was calculated to be 497 and 751 F g^{-1}, respectively, based on GCD measurement collected at a current density of 1 A g^{-1} (see Figure 2.28d). The detailed result of EC measurements of the A4G electrode collected in the negative voltage range (-1.0–0 V and -0.5–0 V) are displayed in Figure 2.29. The charge storage capacity of both electrodes in a device should be balanced to attain maximum performance [37]. Because the specific capacitance values of the A4G and CMAP@A4G electrodes obtained in a three-electrode configuration are different in the same loading mass and voltage range, adjusting loading mass is an effective way to balance their charge storage capacities. The CMAP@A4G electrode exhibited about 1.5 times the charge storage capacity of the A4G electrode under the same loading mass condition. Therefore, the loading mass densities of A4G and CMAP@A4G electrodes were adjusted to 1.5–1.8 and 1.0–1.2 mg cm^{-2}, respectively, for ASC device fabrication. The detailed calculation procedure is given in the experimental section. Figure 2.28e shows the CV curves of the CMAP@A4G//A4G ASC device at different voltage ranges collected at a scan rate of 10 mV s^{-1}. Also, Figure 2.28f and g exhibit GCD curves and corresponding specific capacitances obtained at different voltage range at a current density of 1.0 A g^{-1}, respectively. The specific capacitance increases from 603 to 659 F g^{-1} as the voltage window increases from 0–1.0 to 0–1.6 V. However, in the case of the GCD curve measured in the 0–1.6 V window, a very asymmetrical charge/discharge curve was shown due to the charge delay and rapid potential drop in a range of 1.5–1.6 V. This is because an irreversible side reaction related to oxidation occurred inside the full-cell and the current response decreased, which is also confirmed by the CV curve rising at 1.5–1.6 V. In the 0–1.5 V range, the ASC device operates stably without side reactions and exhibit high capacity. Therefore, the 0–1.5 V range was adopted for further measurement of the ASC device. Additionally, the inset in Figure 2.41g represents the as-prepared ASC device lighting up three light-emitting diodes (LEDs; red, yellow, and green colors; bright (left) and dark (right) space, respectively), suggesting that the device is practical enough as a charge storage system.

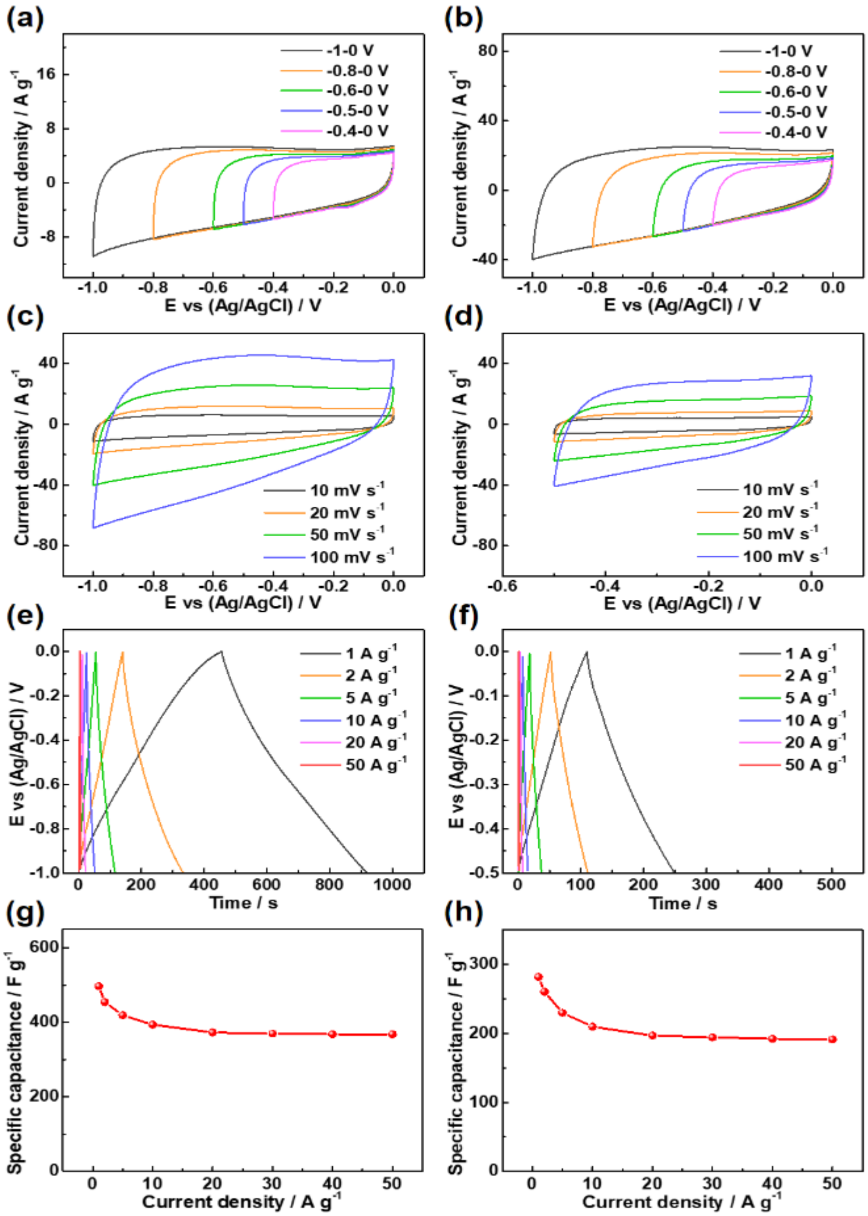

Figure 2.29. Electrochemical performance of A4G obtained in the negative potential window in a three-electrode system using 1.0 M H_2SO_4 electrolyte: CV curves at different potential ranges and different scan rates, i.e., (a) 10 mV s^{-1} and (b) 50 mV s^{-1}, respectively; (c, d) CV curves at different scan rates and different potential windows, (e-h) GCD curves and corresponding specific capacitances at various current densities ranging from 1 to 50 A g^{-1}, respectively. Note that the (c, e, g) and (d, f, h) data were obtained at different potential ranges, i.e., -1.0–0 V and -0.5–0 V, respectively.

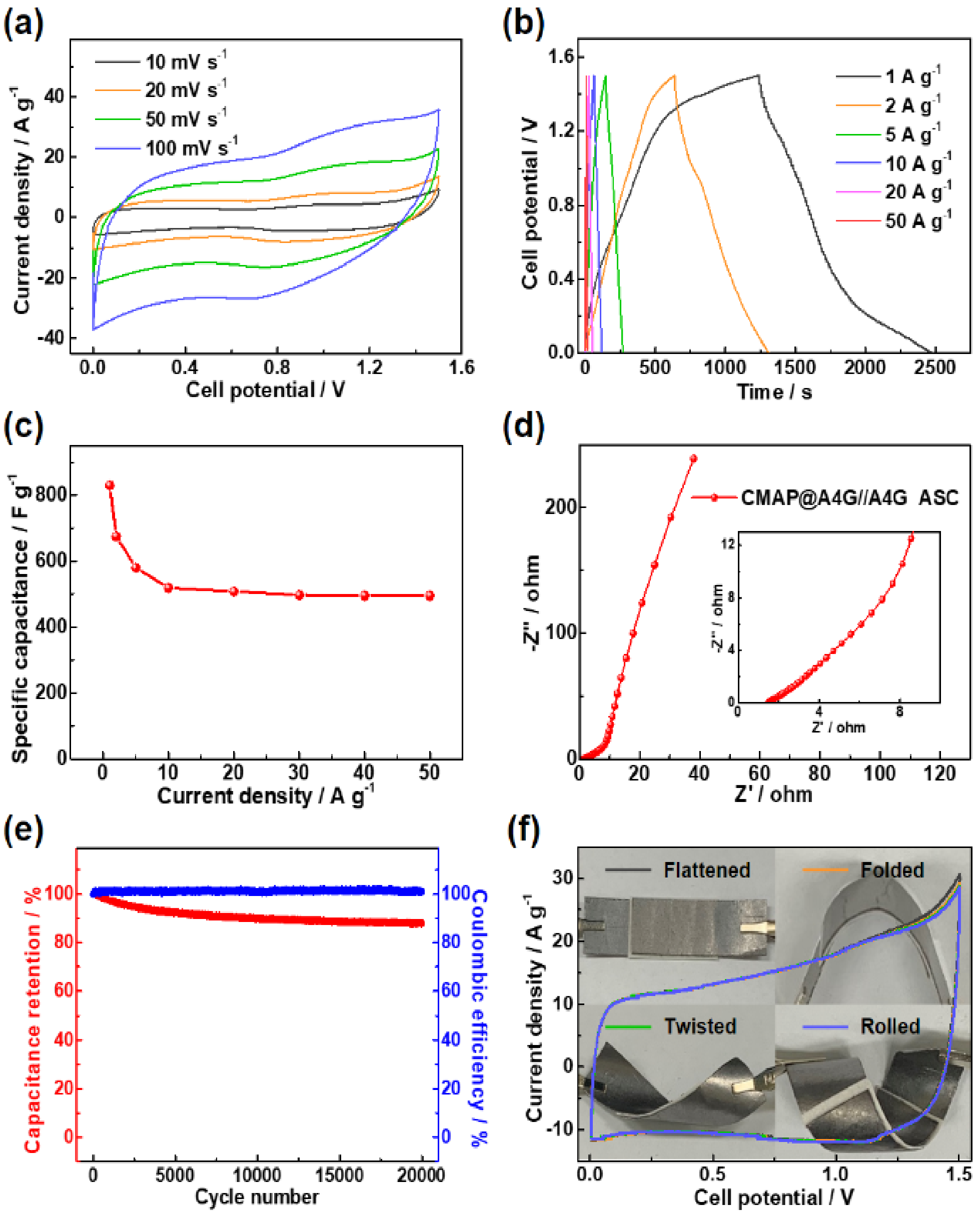

Figure 2.30. EC performance of the CMAP@A4G//A4G ASC device: (a) CV curves at different scan rates; (b) GCD curves at various current densities; (c) specific capacitance obtained at different scan rates from 1 to 50 A g^{-1}; (d) Nyquist plot of the ASC device with the inset showing high-frequency region; (e) capacitance retention and Coulombic efficiency based on the total mass of the two electrodes upon 20,000 GCD cycles at a current density of 10 A g^{-1}; and (f) CV curves for flexibility test when flattened, folded, twisted, and rolled at a fixed scan rate of 50 mV s^{-1} with the inset showing pictures of each motion.

As shown in Figure 2.30a, CV curves of the as-prepared CMAP@A4G//A4G ASC device were studied at different scan rates ranging from 10 to 100 mV s^{-1} at a fixed voltage range at 0–1.6 V. As expected, the ASC device exhibited combined contribution of both non-faradaic and faradaic reactions due to the double-layer capacitive and pseudocapacitive behaviors of each electrode. When the scan rate is increased from 10 to 50 mV s^{-1}, the generated current density increases while still maintaining the initial shape of the CV curve. Figure 2.30b and c show the GCD curves of the ASC device measured at different current densities from 1 to 50 A g^{-1} and the corresponding specific capacitances calculated from these GCD data, respectively. The ASC device represents a maximum specific capacitance of 830 F g^{-1} at a current density of 1.0 A g^{-1}, and 495 F g^{-1} even at a higher current density of 50 A g^{-1}, which are calculated by the total mass of both electrodes. Figure 2.30d displays the Nyquist plot of the CMAP@A4G//A4G ASC device showing a typical aspect with negligible internal and charge transfer resistance. As shown in Figure 2.30f, the flexibility test of the quasi-solid-state ASC device was performed through CV measurements at a scan rate of 50 mV s^{-1}. Even if the ASC device was subjected to deformation such as folding, twisting, and rolling, the CV curve of the flat state is well maintained, which demonstrates the excellent mechanical durability and electrochemical integrity of the ASC device. By fitting energy and power densities, the CMAP@A4G//A4G ASC device delivers maximum energy and power densities of 76.6 Wh kg^{-1} and 27,634 W kg^{-1} and a minimum of 48.9 Wh kg^{-1}

and 495 W kg^{-1}, respectively. Figure 2.32 shows the Ragone plot of the CMAP@A4G//A4G ASC device, and other reported ASC devices are also inserted for comparison. Interestingly, the values of energy and power densities of the ASC device in this work are superb to those of other previously reported ASC devices such as polyaminoanthraquinone-triphenylamine (PAQTA)//activated carbon (AC) (60 Wh kg^{-1}, 1.3 kW kg^{-1}) [4], CoSe-graphene (G) composite//AC (45.5 Wh kg^{-1}, 1.1 kW kg^{-1}) [54], Co_3O_4/carbon cloth (CC)//MnO/CC (59.6 Wh kg^{-1}, 1.5 kW kg^{-1}) [55], MnO_2/PANI@cellulose//rGO@cellulose (41.5 Wh kg^{-1}, 5.2 kW kg^{-1}) [56], $CoWO_4$/Co_3O_4//AC (57.8 Wh kg^{-1}, 6 kW kg^{-1}) [57], $FeCo_2O_4$@polypyrrole (PPy)//AC (68.8 Wh kg^{-1}, 15.5 kW kg^{-1}) [58], and NiSe-G composite//AC (50.1 Wh kg^{-1}, 8.0 kW kg^{-1}) [59]. Furthermore, the cycling stability test of the CMAP@A4G//A4G ASC device was conducted through GCD measurement at a current density of 10 A g^{-1} for 20,000 cycles as shown in Figure 2.30e. After 20,000 cycles, only about 12 % of the initial specific capacitance decreased (maintaining ≈88 %), and almost 100 % of the Coulombic efficiency (98.9–99.7 %) remained. Additionally, a symmetric supercapacitor (SSC) device was assembled using CMAP@A4G hybrids as both positive and negative electrodes to compare the EC performances of the ASC device as shown in Figure 2.31a and b. Also, the EC performances of the SSC device were evaluated in the same way as the ASC device. In the case of CV curves in Figure 2.31c and d, the SSC device shows a nearly rectangular CV shape with a small area compared to that of the ASC device. Also, a large side reaction is observed from the 1.5 V range. Overall, the specific capacitance and Coulombic efficiency are decreased due to the insignificant Faradaic reactions and the excessive side reactions, which can be confirmed through the GCD results in Figure 2.31e and f. The results of the EIS analysis and cycle test are displayed in Figure 2.31g, h, and Table 2.12. The SSC device remains at 82 % of its initial capacitance and shows nearly 100 % Coulombic efficiency upon 20,000 GCD cycles collected at a current density of 10 A g^{-1}. As a result, the maximum capacitance, energy density, and power density of the SSC device were calculated to be 541 F g^{-1} (at 1.0 A g^{-1}), 50.6 Wh kg^{-1}, and 495 W kg^{-1}, respectively. The detailed data (Ragone plot) are also shown in Figure 2.32.

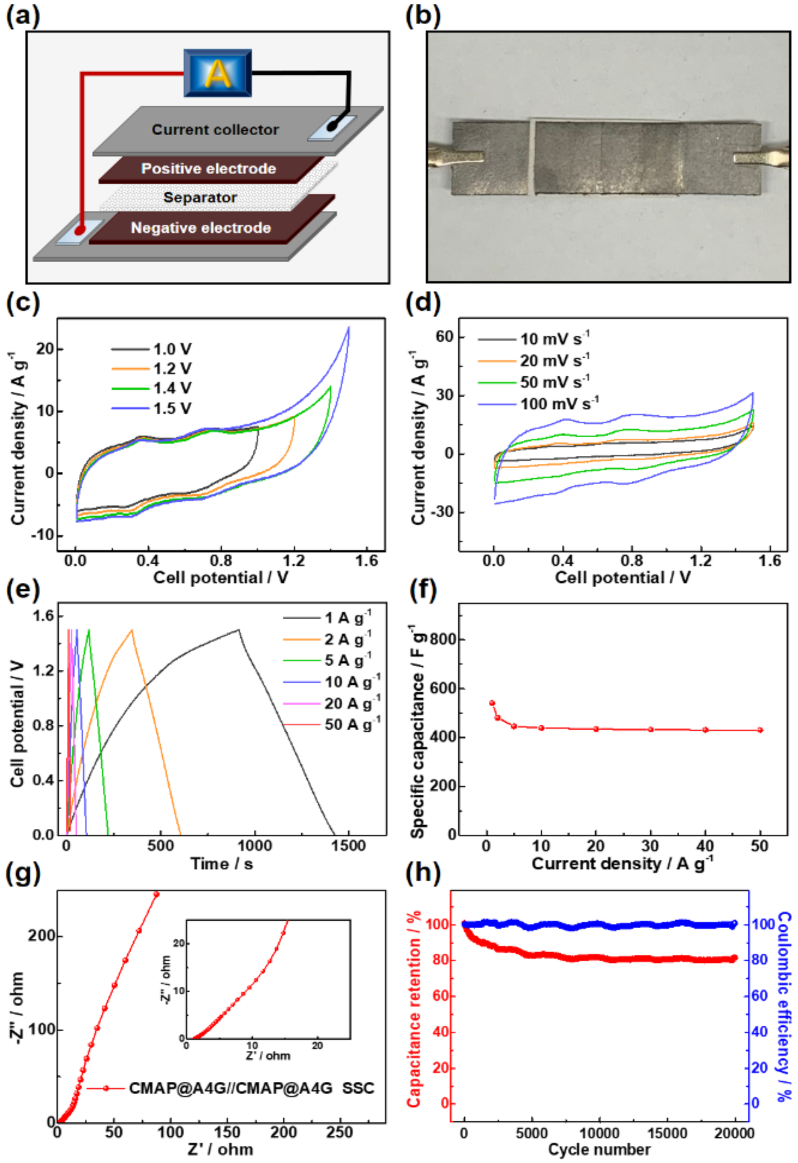

Figure 2.31. (a) Schematic illustration and (b) picture of CMAP@A4G//CMAP@A4G SSC device composed of CMAP@A4G cathode, CMAP@A4G anode, filter paper (separator), and graphite foil (current collector); (c) CV curves of the SSC device collected at different voltage ranges at a scan rate of 10 mV s^{-1}; (d) CV curves of the SSC device at different scan rates; (e) GCD curves of the SSC device at various current densities; (f) specific capacitance measured at different scan rates from 1 to 50 A g^{-1}; (g) Nyquist plot of the SSC device with inset showing high-frequency region; and (h) capacitance retention and Coulombic efficiency based on the total mass of the two electrodes upon 20,000 GCD cycles at a current density of 10 A g^{-1}.

Table 2.12. Fitting parameters for impedance spectra of CMAP, CMAP@A0G, CMAP@A1G, CMAP@A4G, CMAP@A8G, CMAP@A4G//A4G ASC device, and CMAP@A4G//CMAP@A4G SSC device according to the electrical equivalent circuit.

Sample	CMAP	CMAP@A0G	CMAP@A1G	CMAP@A4G	CMAP@A8G
R_{el} / Ω cm^2	0.58	0.61	0.57	0.51	0.55
R_s / Ω cm^2	0.72	0.62	0.43	0.40	0.46
C_s / mF cm^2	0.39	0.36	0.88	1.28	0.66
C_{dl} / F cm^2	0.29	0.53	0.91	1.11	0.79
R_{ct} / Ω cm^2	132.2	111.7	89.4	87.1	106.8
W_s / Ω cm^2	2.21×10^{-2}	1.76×10^{-2}	1.54×10^{-2}	1.49×10^{-2}	1.61×10^{-2}

Device	CMAP@A4G//A4G ASC	CMAP@A4G//CMAP@A4G SSC
R_{el} / Ω cm^2	1.45	1.08
R_s / Ω cm^2	1.21	1.31
C_s / mF cm^2	2.46	1.49
C_{dl} / F cm^2	1.27	1.13
R_{ct} / Ω cm^2	118.39	146.51
W_s / Ω cm^2	1.71×10^{-2}	1.83×10^{-2}

Table 2.13. Comparison of capacitance of previously reported active materials for supercapacitors.

Materials	Maximal C_s / F g^{-1}	Electrolyte	Potential range / V	Current density / A g^{-1}	Mass loading / mg cm^{-2}	Ref.
CMAP@A4G	**751**	**1.0 M H_2SO_4**	**0-1**	**1**	**1**	**This work**
PTPA-25	335	1.0 M H_2SO_4	0.1-0.9	0.5	1	**[3]**
PAQTA	576	0.5 M H_2SO_4	0.2-0.8	1	1	**[4]**
Fc-CMPs/rGO	470	1.0 M H_2SO_4	0-0.8	0.5	0.85	**[14]**
GCH-NC	759	6 M KOH	0-0.4	1	12	**[20]**
PTCT-C	558	6 M KOH	-1-0	1	NA	**[44]**
PPy hydrogel	400	1.0 M H_2SO_4	0-0.8	1	1.8	**[45]**
TpPa-(OH)$_2$	416	1.0 M buffer (P)	-0.2-0.5	0.5	0.2	**[47]**
CNF@PTPA	0.7 F cm^{-2}	0.5 M H_2SO_4	0-0.8	0.01 A cm^{-2}	0.4 μg cm^{-1}	**[48]**
3D RGO/PANI	385	1.0 M H_2SO_4	0-1	0.5	NA	**[49]**
MOF-74-GNRod	198	1.0 M H_2SO_4	0-1	0.5	2	**[50]**
HPC-1.5	283	6 M KOH	-1-0.3	1	NA	**[51]**
PANI/MPC	900	1.0 M H_2SO_4	-0.2-0.7	0.5	5	**[52]**
RGO/PANI/eCFC	1145	1.0 M H_2SO_4	0-0.8	1	0.5	**[53]**
DAAQ-TFP COF	0.003 F cm^{-2}	0.1 M TBAPF$_6$	-2-0	0.1 μA cm^{-2}	NA	**[56]**

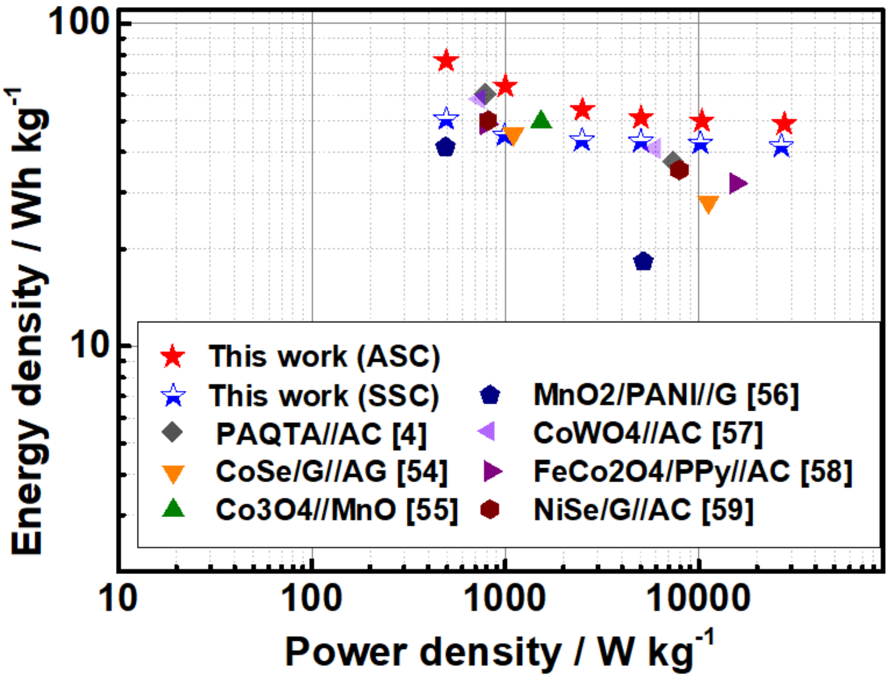

Figure 2.32. Ragone plots of CMAP@A4G//A4G ASC and CMAP@A4G//CMAP@A4G SSC devices as well as previously referred ASC devices: [4] PAQTA//AC; [54] CoSe-G composite//AC; [55] Co_3O_4/CC//MnO/CC; [56] MnO_2/PANI@cellulose//rGO@cellulose; [57] $CoWO_4$/Co_3O_4//AC; [58] $FeCo_2O_4$@PPy//AC; and [59] NiSe-G composite//AC.

2.2.4 Summary

In summary, conjugated microporous anthraquinonylamine-based polymer network grafted with activated graphene (CMAP@AG) hybrids were synthesized via a facile one-step BH coupling. The electrical conductivity of the polymer network was improved by the incorporation of the activated graphene. Also, the porosity and ion conductivity of the hybrid network can be efficiently optimized by the incorporated activated graphene because the flake size and porosity of the activated graphene nanosheets are easily tuned by chemical etching method. By controlling the acid-treatment time for graphene activation, the optimized CMAP@A4G composed of anthraquinonylamine, triphenylamine, and porous graphene showed high redox activity, electrical conductivity, and physicochemical durability with a large surface area up to 498 m^2 g^{-1}. The CMAP@A4G hybrid electrode exhibited a remarkable specific capacitance of 751 F g^{-1} at a current density of 1.0 A g^{-1} and could maintain 97 % of initial capacitance even after 20,000 cycles at a current density of 10 A g^{-1}. Furthermore, asymmetric supercapacitors assembled from the as-prepared CMAP@A4G, A4G, and 1.0 M H_2SO_4/PVA quasi-solid-state electrolyte exhibit a high energy density of 76.6 Wh kg^{-1} and power density of 27,634 W kg^{-1}, as well as long-term cycle stability (i.e., capacitance retention of 88 % after 20,000 cycles at 10 A g^{-1}) within the voltage range of 0–1.5 V. These investigations suggest that the CMAP@A4G hybrid is a promising candidate for achieving high-performance supercapacitors and provide insights for further development of electrode materials toward efficient electrochemical energy storage in the future.

2.2.5 References

[1] F. Vilela, K. Zhang, M. Antonietti, Conjugated porous polymers for energy applications, Energy Environ. Sci. 5 (2012) 7819–7832.

[2] K. Amin, N. Ashraf, L. Mao, C.F.J. Faul, Z. Wei, Conjugated microporous polymers for energy storage: recent progress and challenges, Nano energy. 85 (2021) 105958.

[3] H. Li, W. Lyu, Y. Liao, Engineering redox activity in conjugated microporous polytriphenylamine networks using pyridyl building blocks toward efficient supercapacitors, Macromol. Rapid Commun. 40 (2019) 1900455.

[4] Y. Liao, H. Wang, M. Zhu, A. Thomas, Efficient supercapacitor energy storage using conjugated microporous polymer networks synthesized from Buchwald-Hartwig coupling, Adv. Mater. 30 (2018) 1705710.

[5] M.E. Roberts, D.R. Wheeler, B.B. McKenzie, B.C. Bunker, High specific capacitance conducting polymer supercapacitor electrodes based on poly(tris(thiophenylphenyl)amine), J. Mater. Chem. 19 (2009) 6977–6979.

[6] R. Holze, Composites and copolymers containing redox-active molecules and intrinsically conducting polymers as active masses for supercapacitor electrodes–an introduction, Polymers 12 (2020) 1835.

[7] I. Shown, A. Ganguly, L.-C. Chen, K.-H. Chen, Conducting polymer-based flexible supercapacitor, Energy Sci. Eng. 3 (2015) 2–26.

[8] M.E. Abdelhamid, A.P. O'Mullane, G.A. Snook, Storing energy in plastics: a review on conducting polymers & their role in electrochemical energy storage, RSC Adv. 5 (2015) 11611–11626.

[9] J. Kim, J.H. Kim, K. Ariga, Redox-active polymers for energy storage nanoarchitectonics, Joule 1 (2017) 739–768.

[10] X. Liu, C.-F. Liu, S. Xu, T. Cheng, S. Wang, W.-Y. Lai, W. Huang, Porous organic polymers for high-performance supercapacitors, Chem. Soc. Rev. 51 (2022) 3181–3225.

[11] R. Shi, C. Han, H. Duan, L. Xu, D. Zhou, H. Li, J. Li, F. Kang, B. Li, G. Wang, Redox-active organic sodium anthraquinone-2-sulfonate (AQS) anchored on reduced graphene oxide for high-performance supercapacitors, Adv. Energy Mater. 8 (2018) 1802088.

[12] X. Chen, H. Wang, H. Yi, X. Wang, X. Yan, Z. Guo, Anthraquinone on porous carbon nanotubes with improved supercapacitor performance, J. Phys. Chem. C 118 (2014) 8262–8270.

[13] L. Gao, S. Gan, H. Li, D. Han, F. Li, Y. Bao, L. Niu, Self-assembling graphene-anthraquinone-2-sulphonate supramolecular nanostructures with enhanced energy density for supercapacitors, Nanotechnology 28 (2017) 275602.

[14] L. Zhang, D. Han, Y. Tao, C. Cui, Y. Deng, X. Dong, W. Lv, Z. Lin, S. Wu, Z. Weng, Q.-H. Yang, Dense organic molecules/graphene network anodes with superior volumetric and areal performance for asymmetric supercapacitors, J. Mater. Chem. A 8 (2020) 461–469.

[15] A.M. Khattak, H. Sin, Z.A. Ghazi, X. He, B. Liang, N.A. Khan, H.R. Alanagh, A. Iqbal, L. Li, Z. Tang, Controllable fabrication of redox-active conjugated microporous polymers on reduced graphene oxide for high performance faradaic energy storage, J. Mater. Chem. A 6 (2018) 18827–18832.

[16] R. Raccichini, A. Varzi, S. Passerini, B. Scrosati, The role of graphene for electrochemical energy storage, Nat. Mater. 14 (2015) 271–279.

[17] X. Li, L. Zhi, Graphene hybridization for energy storage applications, Chem. Soc. Rev. 47 (2018) 3189–3216.

[18] J.H. Lee, N. Park, B.G. Kim, D.S. Jung, K. Im, J. Hur, J.W. Choi, Restacking-inhibited 3D reduced graphene oxide for high performance supercapacitor electrodes, ACS Nano 7 (2013) 9366–9374.

[19] W.H. Antink, Y. Choi, K.-D. Seong, J.M. Kim, Y. Piao, Recent progress in porous graphene and reduced graphene oxide-based nanomaterials for electrochemical energy storage devices, Adv. Mater. Interfaces 5 (2018) 1701212.

[20] J. Kang, M. Hwang, K.-D. Seong, L. Lyu, D. Ko, Y. Piao, Three-dimensional nanocomposite of graphene/MWCNT hydrogel grafted with Ni–Co hydroxide nanorods as high-performance electrode for asymmetric supercapacitor, Electrochim. Acta 346 (2020) 136258.

[21] B. Konkena, S. Vasudevan, Understanding aqueous dispersibility of graphene oxide and reduced graphene oxide through pK(a) measurements, J. Phys. Chem. Lett. 3 (2012) 867–872.

[22] X. Wang, L. Jiao, K. Sheng, C. Li, L. Dai, G. Shi, Solution-processable graphene nanomeshes with controlled pore structures, Sci. Rep. 3 (2013) 1996.

[23] K. Krishnamoorthy, M. Veerapandian, K. Yun, S.-J. Kim, The chemical and structural analysis of graphene oxide with different degrees of oxidation, Carbon 53 (2013) 38–49.

[24] L. Peng, Z. Fang, Y. Zhu, C. Yan, G. Yu, Holey 2D nanomaterials for electrochemical energy storage, Adv. Energy Mater. 8 (2018) 1702179.

[25] D. Pan, S. Wang, B. Zhao, M. Wu, H. Zhang, Y. Wang, Z. Jiao, Li storage properties of disordered graphene nanosheets, Chem. Mater. 21 (2009) 3136–3142.

[26] X. Zhao, C.M. Hayner, M.C. Kung, H.H. Kung, Flexible holey graphene paper electrodes with enhanced rate capability for energy storage applications, ACS Nano 5 (2011) 8739–8749.

[27] X. Zhao, C.M. Hayner, M.C. Kung, H.H. Kung, In-plane vacancy-enabled high-power Si/graphene composite electrode for lithium-ion batteries, Adv. Energy Mater. 1 (2011) 1079–1084.

[28] Y. Cho, J.M. Kim, B. Yan, H. Hong, Y. Piao, Influence of flake size and porosity of activated graphene on the performance of silicon/activated graphene composites as lithium-ion battery anodes, J. Electroanal. Chem. 876 (2020) 114475.

[29] J.-B. Wu, M.-L. Lin, X. Cong, H.-N. Liu, P.-H. Tan, Raman spectroscopy of graphene-based materials and its applications in related devices, Chem. Soc. Rev. 47 (2018) 1822–1873.

[30] L.-Q. Mai, A. Minhas-Khan, X. Tian, K.M. Hercule, Y.-L. Zhao, X. Lin, X. Xu, Synergistic interaction between redox-active electrolyte and binder-free functionalized carbon for ultrahigh supercapacitor performance, Nat. Commun. 4 (2013) 2923.

[31] Y. Liao, C. Zhang, Y. Zhang, V. Strong, J. Tang, X.-G. Li, K. Kalantar-zadeh, E.M.V. Hoek, K.L. Wang, R.B. Kaner, Carbon nanotube/polyaniline composite nanofibers: facile synthesis and chemosensors, Nano Lett. 11 (2011) 954–959.

[32] Y. Liao, J. Weber, B.M. Mills, Z. Ren, C.F.J. Faul, Highly efficient and reversible iodine capture in hexaphenylbenzene-based conjugated microporous polymers, Macromolecules 49 (2016) 6322–6333.

[33] Y.L. Zhong, Z. Tian, G.P. Simon, D. Li, Scalable production of graphene via wet chemistry: progress and challenges, Mater. Today 18 (2015) 73–78.

[34] D.-J. Chen, Q.-L. Zhang, J.-X. Feng, K.-J. Ju, A.-J. Wang, J. Wei, J.-J. Feng, One-pot wet-chemical co-reduction synthesis of bimetallic gold-platinum nanochains supported on reduced graphene oxide with enhanced electrocatalytic activity, J. Power Sources 287 (2015) 363–369.

[34] Y. Fang, B. Luo, Y. Jia, X. Li, B. Wang, Q. Song, F. Kang, L. Zhi, Renewing functionalized graphene as electrodes for high-performance supercapacitors, Adv. Mater. 24 (2012) 6348–6355.

[35] H. Kim, M.E. Fortunato, H. Xu, J.H. Bang, K.S. Suslick, Carbon microspheres as supercapacitors, J. Phys. Chem. C 115 (2011) 20481–20486.

[36] L. Ma, H.L. Zhuang, S. Wei, K.E. Hendrickson, M.S. Kim, G. Cohn, R.G. Hennig, L.A. Archer, Enhanced Li–S batteries using amine-functionalized carbon nanotubes in the cathode, ACS Nano 10 (2016) 1050–1059.

[37] X.-C. Li, Y. Zhang, C.-Y. Wang, Y. Wan, W.-Y. Lai, H. Pang, W. Huang, Redox-active triazatruxene-based conjugated microporous polymers for high-performance supercapacitors, Chem. Sci. 8 (2017) 2959–2965.

[38] M. Salanne, B. Rotenberg, K. Naoi, K. Kaneko, P.-L. Taberna, C.P. Grey, B. Dunn, P. Simon, Efficient storage mechanisms for building better supercapacitors, Nat. Energy 1 (2016) 16070.

[39] T. Liu, S. Sun, Z. Zang, X. Li, X. Sun, F. Cao, J. Wu, Effects of graphene with different sizes as conductive additives on the electrochemical performance of a $LiFePO_4$ cathode, RSC Adv. 7 (2017) 20882–20887.

[40] S. Admassie, A. Elfwing, O. Inganäs, Electrochemical synthesis and characterization of interpenetrating networks of conducting polymers for enhanced charge storage, Adv. Mater. Interfaces 3 (2016) 1500533.

[41] B.-A. Mei, O. Munteshari, J. Lau, B. Dunn, L. Pilon, Physical interpretations of Nyquist plots for EDLC electrodes and devices, J. Phys. Chem. C 122 (2018) 194–206.

[42] A. Chonat, S. Palatty, Enhanced electrochemical performance of a hybrid supercapacitive material based on ternary doped polyaniline/activated carbon composite, Energy Fuels 34 (2020) 10148–10159.

[43] Y. Liu, Y. Bai, W. Jaegermann, R. Hausbrand, B.-X. Xu, Impedance modeling of solid-state electrolytes: influence of the contacted space charge layer, ACS Appl. Mater. Interfaces 13 (2021) 5895–5906.

[44] H.G. Wang, Z.H. Cheng, Y.Z. Liao, J.H. Li, J. Weber, A. Thomas, C.F.J. Faul, Conjugated microporous polycarbazole networks as precursors for nitrogen-enriched microporous carbons for CO_2 storage and electrochemical capacitors, Chem. Mater. 29 (2017) 4885–4893.

[45] Y. Shi, L. Pan, B. Liu, Y. Wang, Y. Cui, Z. Bao, G. Yu, Nanostructured conductive polypyrrole hydrogels as high-performance, flexible supercapacitor electrodes, J. Mater. Chem. A 2 (2014) 6086–6091.

[46] C.R. DeBlase, K. Hernández-Burgos, K.E. Silberstein, G.G. Rodríguez-Calero, R.P. Bisbey, H.D. Abruna, W.R. Dichtel, Rapid and efficient redox processes within 2D covalent organic framework thin films, ACS Nano 9 (2015) 3178–3183.

[47] S. Chandra, D.R. Chowdhury, M. Addicoat, T. Heine, A. Paul, R. Banerjee, Molecular level control of the capacitance of two-dimensional covalent organic frameworks: role of hydrogen bonding in energy storage materials, Chem. Mater. 29 (2017) 2074–2080.

[48] W. Lyu, W. Zhang, H. Liu, Y. Liu, H. Zuo, C. Yan, C.F.J. Faul, A. Thomas, M. Zhu, Y. Liao, Conjugated microporous polymer network grafted carbon nanotube fibers with tunable redox activity for efficient flexible wearable energy storage, Chem. Mater. 32 (2020) 8276–8285.

[49] Y. Meng, K. Wang, Y. Zhang, Z. Wei, Hierarchical porous graphene/polyaniline composite film with superior rate performance for flexible supercapacitors, Adv. Mater. 25 (2013) 6985–6990.

[50] P. Pachfule, D. Shinde, M. Majumder, Q. Xu, Fabrication of carbon nanorods and graphene nanoribbons from a metal–organic framework, Nat. Chem. 8 (2016) 718–724.

[51] D. Zhu, Y. Wang, L.W. Lu, H. Zhang, Z. Song, D. Luo, L. Gan, M. Liu, D. Sun, A novel synthesis of hierarchical porous carbons from interpenetrating polymer networks for high performance supercapacitor electrodes, Carbon 111 (2017) 667–674.

[52] Y.-G. Wang, H.-Q. Li, Y.-Y. Xia, Ordered whisker-like polyaniline grown on the surface of mesoporous carbon and its electrochemical capacitance performance, Adv. Mater. 18 (2006) 2619–2623.

[53] P. Yu, Y. Li, X. Zhao, L. Wu, Q. Zhang, Graphene-wrapped polyaniline nanowire arrays on nitrogen-doped carbon fabric as novel flexible hybrid electrode materials for high-performance supercapacitor, Langmuir 30 (2014) 5306–5313.

[54] B. Kirubasankar, V. Murugadoss, S. Angaiah, Hydrothermal assisted in situ growth of CoSe onto graphene nanosheets as a nanohybrid positive electrode for asymmetric supercapacitors, RSC Adv. 7 (2017) 5853–5862.

[55] N. Yu, K. Guo, W. Zhang, X. Wang, M.-Q. Zhu, Flexible high-energy asymmetric supercapacitors based on MnO@C composite nanosheet electrodes, J. Mater. Chem. A 5 (2017) 804–813.

[56] F. Hekmat, S. Shahrokhian, N. Taghavinia, Ultralight flexible asymmetric supercapacitors based on manganese dioxide–polyaniline nanocomposite and reduced graphene oxide electrodes directly deposited on foldable cellulose papers, J. Phys. Chem. C 122 (2018) 27156–27168.

[57] M. Zhang, H. Fan, N. Zhao, H. Peng, X. Ren, W. Wang, H. Li, G. Chen, Y. Zhu, X. Jiang, P. Wu, 3D hierarchical $CoWO_4/Co_3O_4$ nanowire arrays for asymmetric supercapacitors with high energy density, Chem. Eng. J. 347 (2018) 291–300.

[58] X. He, Y. Zhao, R. Chen, H. Zhang, H. Liu, Q. Liu, D. Song, R. Li, J. Wang, Hierarchical $FeCo_2O_4$@polypyrrole core/shell nanowires on carbon cloth for high-performance flexible all-solid-state asymmetric supercapacitors, ACS Sustainable Chem. Eng. 6 (2018) 14945–14954.

[59] B. Kirubasankar, V. Murugadoss, J. Lin, T. Ding, M. Dong, H. Liu, J. Zhang, T. Li, N. Wang, Z. Guo, S. Angaiah, In situ grown nickel selenide on graphene nanohybrid electrodes for high energy density asymmetric supercapacitors, Nanoscale 10 (2018) 20414–20425.

Chapter 3. Conclusion

Research on improving the energy density of supercapacitors is one of the most important issues in the development of eco-frendly and renewable energy storage devices, and the capacitance (C) and voltage range (V) determine the electrochemical performance of the device. For this, it is necessary to develop conductive structural active materials which are stable with a large specific surface area, and the properties such as high charge/ion conductivity, affinity with an electrolyte, and additional redox reactivity must be required. Furthermore, the electrode active materials and the energy storage device should be fabricated by using eco-friendly and safe (harmless to the human body) raw materials and through cost-effective production methods. Therefore, this thesis aims to develop a high-performance supercapacitor device with improved energy density and praticality, i.e., cycle stability and flexibility, by synthesizing a hierarchically porous carbon/polymer composite with a stable and large specific surface area via an facile method and utilizing it as the electrode materials.

First, a fabric-type active electrode made of carbon fibers, in which a hierarchically porous carbon structure with a large specific surface area was stably formed, was prepared through a heat treatment method of a mixture consisting of citric acid and potassium hydroxide (KOH) which can be easily obtained from nature. Since the conventional porous carbon manufacturing methods are mainly obtained as powder-type product, no matter how large a specific surface area and high reactivity it may have, the amount of activated carbon production yield is too small, so industrialization is greatly limited. Also, there are disadvantages in that the electrochemical performance of the active material is significantly lowered by the electrode manufacturing process involving slurry preparation, coating, and anealing. A gel-type mixture with high viscosity and high carbon content was prepared by controlling the content of KOH, which act as a thermal activation catalyst, and the temperature and time of the pre-heat treatment, and the mixture was applied to the carbon fabric. Thereafter, a fabric-type active electrode in which a hierarchically porous carbon was evenly coated on the surface of carbon fibers was obtained through a heat treatment process. The as-prepared active fabric exhibited a large specific surface area while maintaining flexibility. In addition, it was confirmed that the ion conductivity and redox reactivity were excellent due to its porosity and oxygen groups on its surface, so that the electrochemical reaction between the electrolyte and electrode surface can be facilitated. It was also confirmed that the prepared porous carbon fabric can be directly used as an electrode and exhibits superior performance than the conventionally used carbon-based flexible free-standing electrode. Finally, despite the porous carbon structure, it was possible to apply a high-loading mass active material on the carbon fiber, and when an all-solid-state symmetrical supercapacitor device was manufactured using this, high energy density with a good cycle stability and a flexibility could be achieved.

Second, a high-performance flexible supercapacitor with greatly improved energy density was developed by synthesizing a conjugated microporous anthrquinonylamine-based polymer grafted with activated graphene (CMAP@AG) hybrid network with excellent pseudocapacitive reaction through a facile Buchwald-Hartwig (BH) coupling reaction and using it as an electrode active material. The CMAP, composed of 2, 6-diaminoanthraquinone and triphenyl amine covalently bonded to each other, is a multi-demensional conductive porous polymer network with excellent thermal/chamical durability and a large specific surface area, and shows good pseudocapacitive capacitance by the redox-active functional groups involving oxygen and nitrogen. By uniformly incorporating activated graphene into this CMAP network, the insufficient electrical conductivity can be improved, thereby broadening the usable voltage range of the active material and enhancing the rate performance and cycle stability. The activated graphene used was perpared by forming in-plane defects on the conventional graphene oxide sheets via acid treatment, and it was possible to sufficiently secure the passage of electrolyte ions with a very large specific surface area. The prepared activated graphene oxide was reduced under BH coupling conditions (wet-chemical reduction), confirming that this is comparable to thermal reduction methods for rGO. Therefore, the optimized CMAP@AG with superior stability and charge/ion conductivity exhibited greatly improved energy density and power density as well as cycle stability and flexibility with the advantages of the pseudocapacitive reactivity and the wide voltage range.

In summary, this study is meaningful in that it developed a high-performance flexible supercapacitor electrode through eco-friendly materials and cost-effective preparation methods, and this provides valuable candidates and insights for further development of electrode materials toward efficient electrochemical energy storage in the future.

국문초록

슈퍼커패시터는 전기화학적 에너지 저장 장치의 한 종류로 저장 용량이 매우 큰 커패시터를 의미한다. 1980 년대부터 상용화되어 상대적으로 짧은 역사를 갖는 슈퍼커패시터는 활성탄소뿐만 아니라 금속산화물 및 전도성 고분자 등 새로운 전극 소재의 등장과 하이브리드 소재 기술의 발전으로 지속적으로 성능이 향상되어왔다. 슈퍼커패시터는 빠른 충·방전 속도와 높은 전력 밀도 및 사이클 안정성으로, 안정하고 고품질의 전기에너지를 제공하여 그 중요성이 더욱 높아지고 있다. 그러나 지속적으로 높아지는 시장 수요를 충족시키기 위해서는 향상된 에너지 밀도를 갖는 유연한 에너지 저장 장치 개발이 필요하고, 이를 위한 연구들이 활발히 진행중이다. 슈퍼커패시터의 에너지 밀도는 장치의 용량값 (capacitance, C)과 작동 전압 범위 (voltage range, V)가 결정한다. 따라서, 본 논문에서는 고성능 유연성 슈퍼커패시터를 제작하기 위해 안정한 계층적 다공성 구조를 갖는 탄소/고분자 복합체 물질을 합성하고, 이를 통해 에너지 저장 용량값과 작동 전압 범위를 향상시키는 방법에 대해 논의하였다.

먼저, 계층적 다공성 탄소 구조가 고르게 코팅된 탄소섬유로 이루어진 직물형 프리스탠딩 (free-standing) 전극을 제조하여 슈퍼커패시터에 활용하였다. 3 차원 다공성 구조로 서로 연결된 활성탄소 전극은 macro- (>50 nm), meso- (2~50 nm), micro- (<2 nm) 크기의 기공 구조가 안정하게 형성되어, 우수한 전하 전도성과 유연성을 나타낼 뿐만 아니라, 이온 확산을 수월하게 하여 뛰어난 에너지 저장 용량값을 갖는다. 또한, 프리스탠딩 전극의 제조법은 바인더 혼합이 필요한 추가적인 전극 제조 공정이 필요하지 않기 때문에 에너지 저장 장치용 전극의 대면적 및 대량생산이 용이하다. 본 활성탄소 전극은 매우 안정한 계층적 다공성 구조를 갖는데, 이는 탄소구조체 원료인 시트르산과 활성화제인 포타슘 이온으로 구성된 유-무기 혼합물의 혼합비와 열처리 온도를 조절함으로써 탄소 수득율을 향상시켰기 때문이다. 또한, 포타슘 이온은 열처리 과정 중에 자가 템플릿 (self-template) 반응과 촉매 반응이

동시에 이루어지도록 하여 약 700℃의 비교적 낮은 열처리 온도에서도 넓은 비표면적을 갖는 안정한 다공성 탄소 구조체가 형성될 수 있었다. 나아가, 열분해 (pyrolysis) 및 염 주형 제거과정으로 형성된 다공성 탄소 구조체는 표면에 잔존하는 산소 관련 작용기로 인해 전해질과의 친화도와 도핑 효과로 보다 향상된 용량값을 얻을 수 있었다. 그 결과, 자가 형성된 계층적 다공성 활성 탄소 전극은 높은 전도성과 다공성 및 산소 관련 작용기의 시너지 효과를 통해 우수한 에너지 저장 용량을 나타냈다. 실질적인 구현성을 확인하고자, 제조된 활성전극을 사용하여 전고체형 대칭성 슈퍼커패시터를 제조하였으며, 전기화학적 평가를 통해 0.69 mWh cm^{-3}의 에너지 밀도와 4.91 mW cm^{-3}의 전력 밀도로 우수한 성능을 나타내는 것을 확인하였다. 또한, 이 장치는 10,000 번의 충·방전 후에도 약 88%의 초기 용량을 유지하는 뛰어난 사이클 안정성과 우수한 유연성을 나타냈다.

두 번째 장에서는, 산화·환원 반응 활성을 띠는 전도성 고분자를 활성화된 그래핀에 접목하여 유사용량 (pseudocapacitive) 반응을 더욱 강화시킴으로써 우수한 에너지 저장 성능을 갖는 슈퍼커패시터를 제조하고자 하였다. 먼저, 화학적 에칭법을 통해 산화그래핀 시트 평면상에 공극 및 찢어짐 등의 결함 형성을 유도하였고, 이렇게 제조된 활성 산화그래핀과 고분자 전구체간 부흐발트-하트윅 커플링 (Buchwald-Hartwig coupling) 반응을 통해, 안트라퀴노닐 아민 기반의 공액 미세다공성 고분자 (conjugated microporous polymer, CMP) 네트워크에 활성화된 그래핀이 고르게 통합된 형태의 복합체를 합성하였다. 여기서 활성그래핀은 매우 견고한 전도성 매트릭스를 제공하여 고분자의 재응집을 막고, 전극 내부로의 이온 확산을 용이하게 한다. 이와 더불어, 안트라퀴노닐 아민과 트리스페닐 아민이 가교결합되어 전도성과 기계적·화학적·열적 안정성을 나타내는 CMP 네트워크는 그래핀의 퇴적 (re-stacking)을 방지하여 복합체 내부의 계층적 다공성을 유지함으로써 우수한 이온 전달과 함께 풍부한 산화·환원 반응 활성 사이트를 제공하고, 전기화학적 전하 저장 용량을 한층 더

향상시킨다. 그래핀의 첨가량과 활성화 정도를 조절하여 고분자/활성그래핀 복합체의 특성을 최적화하였고, 결과적으로 높은 용량, 빠른 충·방전 속도, 사이클 안정성, 및 유연성을 갖는 전극을 제조할 수 있었다. 나아가, 합성한 고분자/활성그래핀 복합체를 양극으로, 활성-그래핀을 음극으로 사용하여 준고체형 비대칭성 슈퍼커패시터를 제조함으로써 작동 전압 범위를 향상시킬 수 있었고, 76.6 Wh kg^{-1} 의 에너지 밀도와 27,634 W kg^{-1} 의 전력 밀도를 달성하였다. 또한, 제조된 장치는 유연성과 함께 20,000 번의 충·방전 사이클 후에도 88%의 초기 용량을 유지하는 뛰어난 사이클 안정성을 나타내었다.

본 논문에서는 높은 용량값을 갖는 3 차원 전극물질을 합성하고, 이를 이용하여 뛰어난 성능을 갖는 유연성 슈퍼커패시터를 제작하였다. 첫 번째 연구에서는 전극 물질의 내부 구조 및 표면기의 최적화를 통해 안정한 다공성 탄소가 형성된 직물형 프리스탠딩 활성 전극을 제조하여 에너지 저장 용량이 향상된 슈퍼커패시터를 제작하였다. 두 번째 연구에서는 산화·환원반응 활성을 띠는 고분자/활성그래핀 복합체를 합성하여 에너지 저장 용량을 극대화하였으며, 넓은 작동 전압 범위를 갖는 비대칭성 슈퍼커패시터를 제작하여 한층 더 향상된 성능을 나타내는 유연성 에너지 저장 장치를 개발하였다. 따라서, 본 연구는 친환경적인 재료와 가격경쟁력 있는 제조법으로 고성능 유연성 에너지 저장 장치 개발 분야에 적용하여 그 성능을 향상시킬 수 있을 것이라 기대한다.

주 요 어 : 슈퍼커패시터, 계층적 다공성 탄소, 활성 그래핀, 공액 미세다공성 고분자 네트워크, 고분자/탄소 복합체

학 번 : 2018-36419